Analysis and correction of geometric distortion in knee-MRI images for computer assisted planning of total knee replacement

Master of Science Thesis

NOOR MUSA

Department of Signals and Systems
Division of Biomedical Engineering
CHALMERS UNIVERSITY OF TECHNOLOGY
Göteborg, Sweden, 2011
Report No. EX057/2011

CHAIR OF MEDICAL ENGINEERING
FACULTY OF MECHANICAL ENGINEERING, RWTH AACHEN

Univ.-Prof. Dr.-Ing. K. Radermacher

Master Thesis

Analysis and Correction of Geometric Distortion in Knee-MRI images for Computer Assisted Planning of Total Knee Replacement

cand.-ing. Noor Musa

Matr.-Nr.: 291419

For the degree of Master of Science in Biomedical Engineering

Examinator: Univ.-Prof. Dr.-Ing. K. Radermacher

Supervisor: Dipl.-Ing. Ghaith Al.Hares

Aachen, 07. 06. 2010

Declaration

I hereby declare that this thesis has been written by myself under the supervision of the Chair of Medical engineering, RWTH Aachen University, without any external unauthorised help. It has been neither presented to any institution for evaluation nor previously published in its entirety or in parts. Any parts, words or ideas of the thesis, how ever limited, and included tables, graphs, maps etc. which are quoted from or based on other sources, have been acknowledged as such without exception.
I'm aware of the fact that any infringement of this declaration and willful deceit will lead to a grading of the thesis with grade 5.0 (Fail).

Aachen, 02. 06. 2010

Signature

Acknowledgment

With this acknowledgement, i would like to express my deep gratitude to all people that contributed time and effort in supporting me when working on and writing this thesis. Without these people this thesis would not have achieved the end.

I am grateful to professor Radermacher for allowing me to join the Meditec team, for his kindness and expertise ideas through the start presentation. Furthermore thanks to my supervisor Ghaith for his guidance, supervision, support throughout the entire research and especially with image processing. Furthermore, Special thanks to Hans, Sabine and Martin for their assistance with CAD-drawings, and to the staff at our workshop for the construction of the phantom. Also, thanks to Dr. Donker at the clinic of diagnostic and interventional radiology for his support with the MRI-scanning.

Finally, I would like to thank my family and friends for their encouragement, as well as their patience and great support.

Aachen, Germany

Summer 2010

Problem statement

The accurate planning of osteotomies and placement of implant components is crucial for the success of the total knee replacement. Among different computer assisted planning approaches the patient-specific templating technique has shown high potential in achieving precise bone resections along with accurate alignment and positioning of the prosthesis components and a reduced intervention time. Today's computer assisted approaches for the planning and customization of templates use CT-based 3D reconstructions of the patient's bony structures and rapid prototyping and therefore provide accurate preoperative planning and intra-operative realization. However, the exposure to ionizing radiations remains a disadvantage of CT-based approaches and it would be desirable to establish the surgical planning using an alternative non-ionizing imaging technique. Furthermore, the actual planning approaches completely rely on the geometry of only bony structures due to the poor quality of soft tissues in CT images. Therefore, the intra-operative realization normally requires an additional preparation work and operation time to remove attached soft tissues like femoral and tibial cartilages before positioning of the individual templates. Latest improvements of the non-invasive magnetic resonance imaging (MRI) concerning the 3D visualization of bone and knee articular cartilage offer advantages for surgical planning and customization of individual templates over CT-based approaches. However, as the quality of the planning is directly affected by the geometric accuracy of the 3D models it is mandatory as the first step to analyze and compensate geometric distortions associated with MR images. This master work will focus on compensating geometrical distortions in knee-MRI images. In the framework of this work a literature research on MRI-related geometric distortions and the state-of-the art on correction methods will be performed at the first step, based on which a concept for the evaluation and compensation of the distortion in knee MR-images will be developed in the next step. The construction of a dedicated calibration phantom which allows the measurement of the distortion as well as the development of a correction method will be main aspects of this work. The concept will be realized by the application of the correction method on test scans taken from reference bodies with known geometries. Finally, a comprehensive evaluation of the method accuracy will be performed.

Summary

Today the patient specific template (PST) has proven high accuracy in osteotomies during total knee replacement surgery (TKR). The 3D reconstruction data which are used to plan the virtual PST are based only on the bony structures and does not account for the volume of femoral and tibial cartilages. Normally muscles, ligaments and cartilage are best seen on MRI images, which offers advantages for surgical planning and customization of individual templates over CT-based approaches. The long term goal is to use the MRI modality instead of the CT for the pre-operative planning since it provides excellent visualization of the knee cartilages and avoid the radiation risks of the the CT-imaging. However, as the quality of the planning is directly affected by the geometric accuracy of the 3D models it is mandatory as the first step to analyze and, if necessary, compensate the geometric distortions associated with MR images. The main focus of this work was on the development and evaluation of a method for the quantification of geometric distortion in MR-images. A dedicated MRI-compatible phantom with reference geometry has been developed and manufactured for this purpose. This phantom provides two grids with densed distributed markers and was constructed to fit inside a knee coil of a MRI scanner. For the purpose of distortion evaluation, the developed phantom was scanned in CT and MRI. A method was developed to extract the centers of a set of phantom markers from the corresponding CT and MRI images based on specific subtraction technique and cylinder fitting algorithm. A set of total 33 markers extracted from the outer grid was used as a reference rigid body for comparison between the CT- and MRI-derived bone models. The comparison of the CT-extracted markers to their reference locations from the phantom geometry has shown a maximal deviation of 0.61 mm, (mean: 0.26 mm, std: 0.16 mm, RMS: 0.31 mm) while the maximal deviation for the MRI-extracted markers compared to the reference geometry was 0.95 mm, (mean: 0.32 mm, std: 0.20 mm, RMS: 0.38 mm). In the comparison between CT-extracted and MRI-extracted markers, where CT was considered as the ground truth, the maximal deviation found was 0.97 mm, (mean: 0.42 mm, std: 0.18 mm, RMS: 0.45 mm). The 3D surface comparison between the MRI- and the CT-derived models using the larger markers set has shown at small regions a deviation up to 4.71 mm, (mean: 1.13 mm, std: 0.56 mm, RMS: 1.26 mm). A correction method based on thin plate splines was also proposed. First investigations using synthetic distortion shapes in computer simulation have shown promising results and potential of the method for the compensation of geometric distortion.

Contents

List of Figures

List of Tables

1 Introduction

MRI is considered today as a valuable tool for soft tissue visualization; it has shown high potentials for the 3D visualization of bone and soft tissues. Geometric distortion has long been regarded as a poor feature of magnetic resonance imaging modality (MRI), an imaging modality that has revolutionized medical imaging in the past two decades. Current generation of MRI scanners has been designed with short gradient rise times, and such restrictions have led to an increase in the gradient field nonlinearity which results in image distortions [Wang et al., 2004a]. Furthermore, Heiland, Hornak, Michiels et al. and Wang et al. have reported the main sources of spatial distortions are the inhomogeneity in the main magnetic field, nonlinearity of the gradient fields and the eddy currents due to the switching of the gradients. These distortion sources are categorized as machine dependent. Patient or object dependent sources such as magnetic susceptibility, chemical shift and flow artifacts are other causes for magnetic field deviations which must be taken into account. [Michiels et al., 1994]. Young et al. made investigation of magnetic susceptibility effects in patients in a series of articles and reported the susceptibility effect induces magnetic field deviations [Young et al., 1987]. Furthermore, Sumanaweera et al. presented an analysis of air-tissue and bone-tissue susceptibility effects [Sumanaweera et al., 1994a].

When using MRI for orthopaedic surgical planning purposes which involve the resection and modification of some anatomical areas, the geometric distortion should first be taken into consideration. The built-in distortion correction systems which exist today in MR scanners are able to correct the distortions due to gradients and magnetic fields. Furthermore, these systems are not able to correct specific distortions caused by either a patient or an object. To achieve specific estimation of the distortion's amount and later on correction of the deformations; a special designed tool with known dimensions has to be scanned with the patient/object, and this tool is considered as a reference body. The correction can be achieved according to the pre-known geometries of the reference body, which allows the individual correction of the geometrical distortions.

An accurate preoperative planning of bone osteotomies and prosthesis components replacement with accurate alignment are the essential keys for the success of total knee replacement surgery (TKR). Today the patient specific template (PST) has proven high accuracy in osteotomies of both femoral and tibial bones [Radermacher et al., 1998].

This computer assisted planning approach is based on computer tomography (CT) modality. It provides accurate preoperative planning and intra-operative realization. Furthermore, the only disadvantage of this approach is that it is based on CT. As known, CT accounts for most diagnostic radiation exposure to patients. The risk of radiation exposure vs. the high localization accuracy (geometric accuracy) and excellent contrast for bony structures of the CT must always be considered. In addition, with CT-based planning there is a lack of femoral and tibial cartilage visualization. The 3D reconstruction data which are used to plan the virtual PST are based only on the bony structures. Therefore, this procedure sets an extra operation time for the surgeon to prepare the bone surface area for fitting exactly with the cutting block [Hafez et al., 2006]. Normally muscles, ligaments and cartilage are often best seen with an MRI, which offers advantages for surgical planning and customization of individual templates over CT-based approaches.

To implement MRI-based planning on PST, patient specific geometrical distortion needs first to be quantified. The short term goal and focus in this work is to quantify the amout of distortion and investigate the effectiveness for a non-rigid registration method (based on the thin plate spline) to calculate the corrective transformation which aims to compensate the distortion. This can be done by using a phantom with known dimensions. The quantification of object-specific distortion and it's evaluation will be performed by several comparisons; CT and phantom geometry, MR and phantom geometry, CT and MR, surface comparison of MR-derived and CT-derived bone model. Further evaluation of the correction method affectivity will be performed by Matlab simulations.

For first investigation of this topic, a MRI compatible phantom is designed, together with a knee model fits inside a lower extremity knee coil, used to both quantify and correct object-specific distortions. This master thesis pursues the following sequence as illustrated below, see figure 1.1. The initial starting point of this thesis is chapter one. Firstly, the thesis provides the reader a general overview of this topic. Secondly, provide a short overview on the applied method. This is followed by the problem limitations and expected method contributions. Next coming chapter i.e. chapter 2 gives a brief overview over the medical and anatomical background as well as the technical background of computer assisted planning approach; PST-technique.

Geometric Distortion chapter, i.e. chapter 3 deals with the main source of the thesis problem and in detail analyze each sub-source of the distortion. Chapter 4 discusses different relevant correction methods which have been proposed; how these are formulated to answer the strategic problem of MRI distortion correction. This chapter is the building stone for this thesis. Chapter 5 represents the methodology chapter containing the approach that has been applied during this study. Strategies of the thesis,simulations, materials, methods and applied construction design are presented. The next last chapter, chapter 6 provides the reader the reached results and evaluations. The final chapter discusses the proposed method as well as the expected results versus gained results. In addition, this chapter includes the conclusions as contribution to science. Future work and recommendations for the next study case with suggestions for further research work are presented here too.

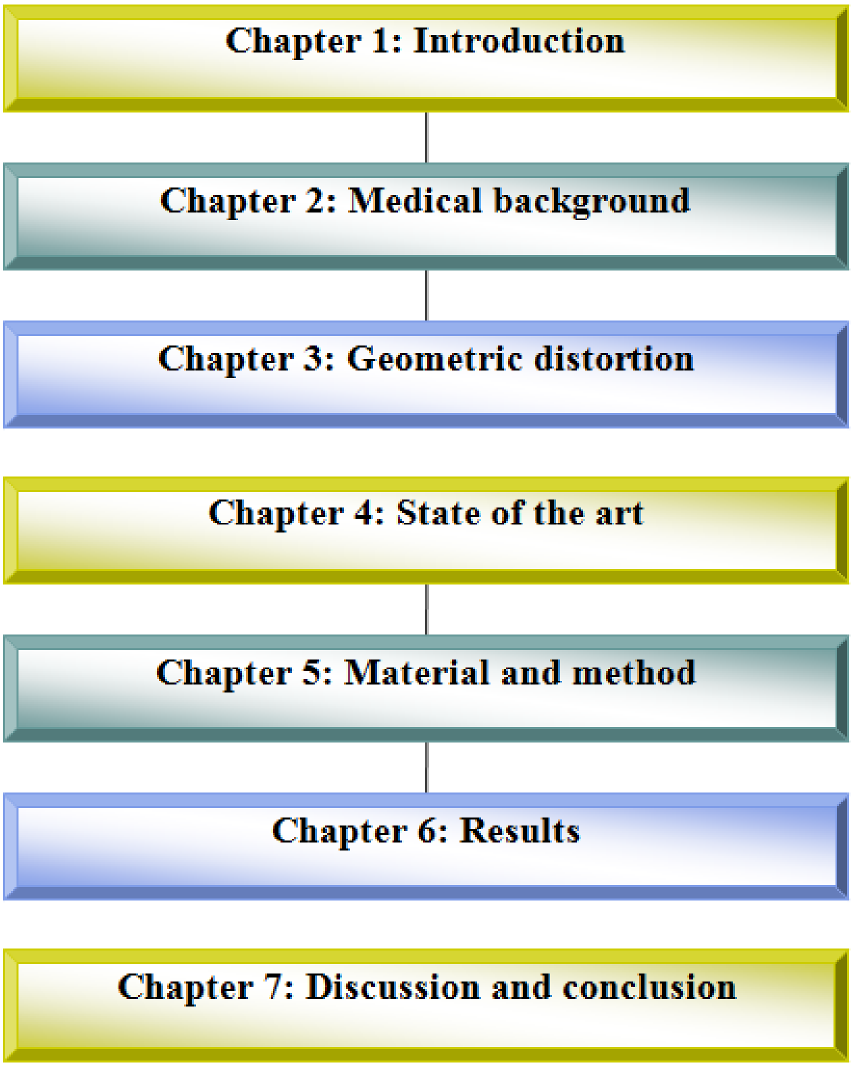

Figure 1.1: Master thesis outline

2 Medical Background

2.1 Basic knee anatomy and function

Knee joint is the largest and most complex joint in the body. It consists of four bones, and are connected by muscles, tendons and ligaments.

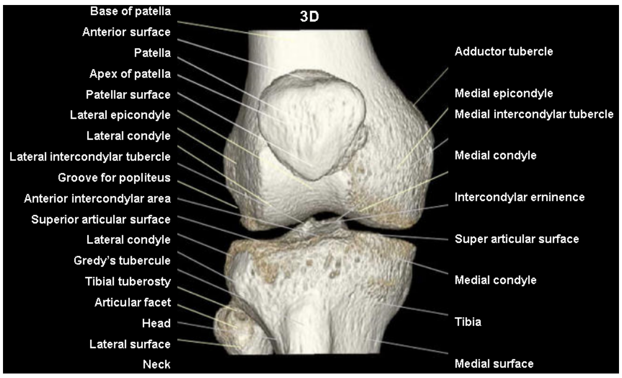

Figure 2.1: 3D view of the knee joint - MRI [www.imaios.com, 2010.03.29]-modified

Figure 2.1 illustrate the anatomy of the knee joint. The femur, which is the large bone in the thigh, is attached by ligaments and a capsule to the tibia. Tibia is the large shin bone. Below and next to the tibia is the fibula, which runs parallel to the tibia. The fibula is the smaller shin bone which slides up and down as the knee bends and straightens. The patella, or the knee cap, rides on the knee joint as the knee bends [Sportmedicine, 2010.03.29].

The bones of the knee joint are connected by the like strong ropes i.e. ligaments, they provide stability to the joints. There are four main ligaments in the knee. In the inner (medial) aspect is the medial collateral ligament (MCL) and lateral collateral ligament (LCL) is on the outer (lateral) part, and in the center of the knee there are the two other main ligaments which are called the anterior cruciate ligament (ACL) and the posterior cruciate ligament (PCL). The smaller ligaments holds the patella in the center of the femoral groove [www.kneepaininfo.com, 2010.03.29]. Figure 2.2 and 2.3 illustrate a sagittal and axial view of the knee, where the ligaments are shown.

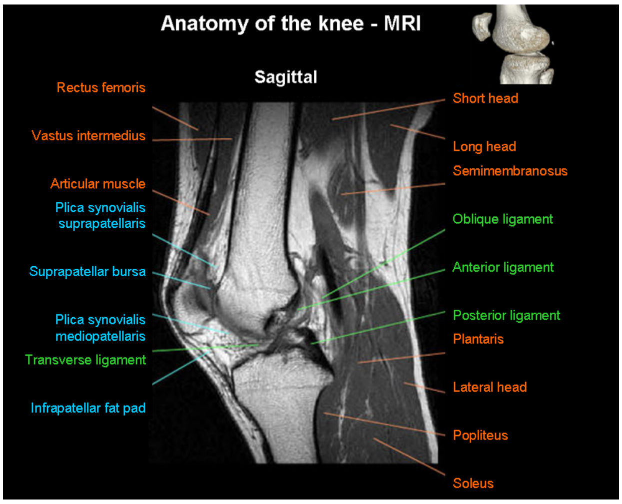

Figure 2.2: Sagittal view MRI [www.imaios.com, 2010.03.29]-modified

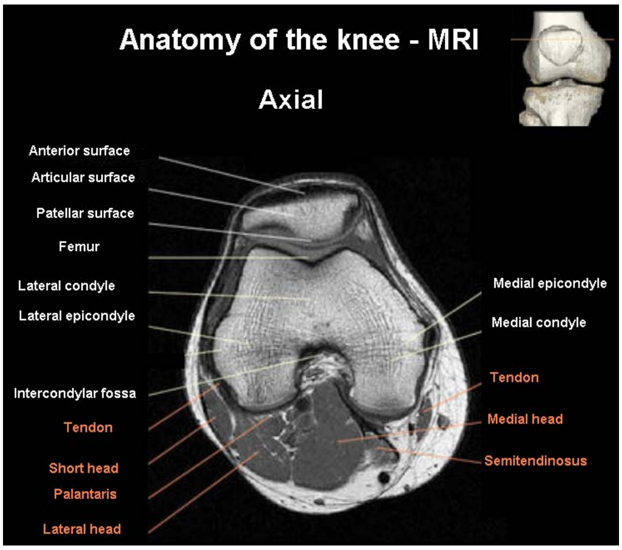

Figure 2.3: Axial view MRI [www.imaios.com, 2010.03.29]-modified

MRI is often used to help investigate the foundation of many potential knee problems. Most common forms of knee problems which are behind the knee damage are rheumatoid arthritis, osteoarthritis and traumatic arthritis. See figure 2.4. Rheumatoid arthritis is a chronic disease causes the synovial membrane to be inflamed and producing too much of synovial fluid that overfills the joint space. It causes damages of the cartilage and eventually cartilage loss, pain and stiffness. Osteoarthritis disease is more often occurred in people of 50 years or older. In this chronic disease the cartilage which cushions the bones of the knee softens and wears away, in turn the bones of the knee joint rub against one another, causing pain and stiffness. Traumatic arthritis can be caused by a trauma that penetrates the joint capsule, introducing infectious agents and resulting in an infectious arthritis or injury the articular cartilage over time, causing knee pain and limiting knee function [www.orthoinfo.aaos.org, 2010.03.15].

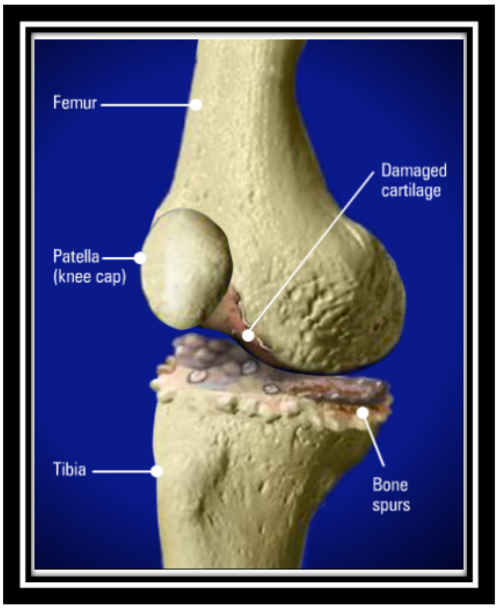

Figure 2.4: Damaged knee joint, [www.wmt.com, 2010.03.15].

When medications, changing activity level, and using walking supports are no longer successful and helpful, then Total Knee Replacement (TKR) surgery is considered. To help resume normal activities again, resurfacing the damaged and worn surfaces of the knee can relieve pain and correct leg deformities, due to arthritis or trauma. TKR was first performed in 1968, and was one of the most outstanding orthopaedic surgical advances of the twentieth centry. Improvements in surgical materials and techniques since then have greatly increased its effectiveness.

2.2 Total Knee Replacement

Total knee replacement (TKR) is a surgical procedure which includes removing the damaged joint lining and replacing the damaged and worn joint surfaces with a metal and plastic implant. That is to relief the pain, correct leg deformities and disability of osteoarthritis and to help resume the normal activities back. It depends on the seriousness level of the arthritis, TKR may not be needed. Alternatively is partial or so called unicompartmental knee replacement, which is performed when only one compartment of the knee is affected by arthritis. During TKR, both damaged bone surface and cartilage of the femur is removed away by cutting, and the surface of the femur is reshaped to allow the artificial femoral component to fit in place, see figure 2.5 a). The artificial femoral component is attached to the surface of femur.

Afterwards, tibial damaged bone surface and cartilage is cut away and reshaped to receive the metal tibial component, 2.5 b). The metal tibial component is attached to the cut surface of the tibia, and then polyethylene insert is attached to the metal tibial component to replace the lost knee cartilage. The insert supports body weight and allows the femur to move on the tibia. The final knee prothesis is shown in figure 2.5 c). The tibia with its new polyethylene surface, and the metal femur surface are put together to form a new artificial knee joint [www.kneepaininfo.com, 2010.03.29; www.wmt.com, 2010.03.15].

2.3 Patient Specific template

Conventional instrument systems are normally based on average data from bone geometry, which may differ widely between patients. Some authors reported several anatomical variations in patients with knee osteoarthritis (OA), in addition other authors reported that significant malalignment errors (>3°) resulted from using extra-medullary and intra-medullary rods. Accuracy of these instrumentations is also questionable [Goble und Justin, 2004]. Usually, such instrumentation systems are relatively complex tools with numerous jigs and fixtures. Their assembly is also time consuming and may lead to additional errors. In addition, their repeated use carries a theoretical risk of contamination [Hafez et al., 2006].

Another technology which have been introduced into clinical practice, are proved to be more accurate than conventional instrumentation systems is navigation and robotic techniques [Brown et al., 2003; Haaker et al., 2005]. Navigation and robotic technique allows elimination of alignment guides. However, this technology is expensive, requires the use of conventional instruments for various bone cuts, also requires additional instruments and technical steps such as registration and tracking. Such procedures lead to prolonged operative time, is concidered as a complex, takes senior surgeons away from their comfort zone and interrupt their learning curve.

A new concept was introduced by Radermacher [Radermacher et al., 1998], Patient-Specific Template (PST), can completely replace conventional instruments, also navigation and robotics. Unlike navigation and robotics, with PST neither computer equipments in the operating room nor registration processes are needed. Furthermore, PST needs no tracking, pin insertions. The

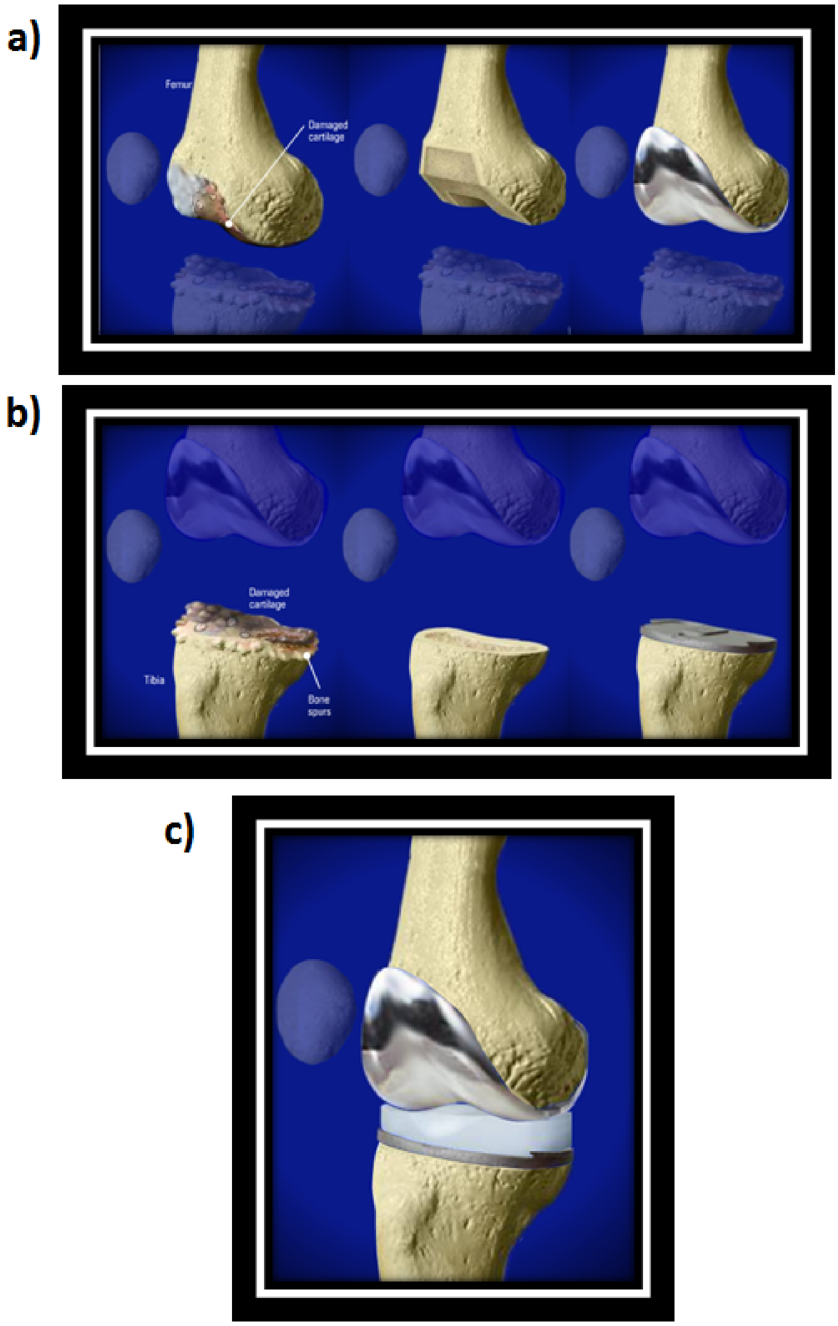

Figure 2.5: Steps of TKR: a)Replacing damaged femur bone. b)Replacing damaged tibia bone. b)Final knee prosthesis. [www.wmt.com, 2010.03.15]

main advantages of PST are the ease of use, reduction of bone cutting time, safe and fast implementation of planned surgery, less expensive, and prevents overloaded surgery with complicated, expensive equipments and time consuming procedures. Technical steps of generation of PST are shown in figure 2.6 and 2.7. Positioning of implant components with high accuracy in TKR with respect to the individual mechanical axis of the leg is necessary. It has a significant affect in both, short and long term outcomes. PST technique is a promising solution for the translation of the high accuracy of the preoperative imaging and planning into precise intraoperative surgery. The

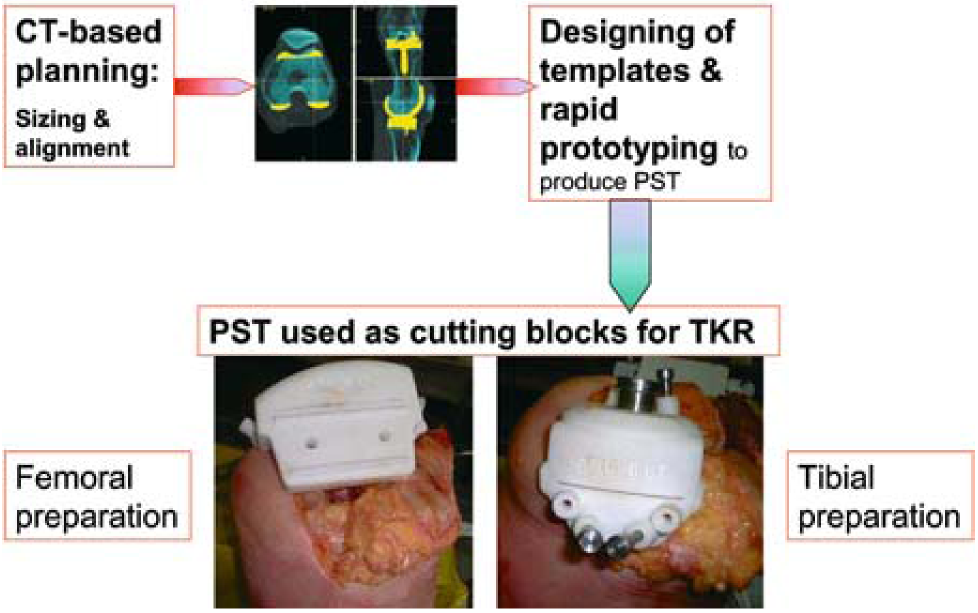

Figure 2.6: Technical steps of PST technology [Hafez et al., 2006]

pre-operative planning starts with 3D reconstruction of a CT scan data, later on sizing and alignment of the prosthetic components, surgical simulations, then template designing and production [Hafez et al., 2006]. For pre-operative production, either a low cost desktop milling machine is used as a 3D printer to mill the individual bone shape into the template, or a rapid prototyping technology.

One main limitation of this approach is that it depends on preoperative CT imaging which also involves the exposure to ionizing radiations. It does not show cartilage very well on CT scans. In turn, that might lead to difficulties in positioning the templates which were based only on bony structures. Consequentely, the surgeon has to lay additional time and work to remove all the cartilage and soft tissues, then positioning the template. All that might lead to errors and inaccuracies of the osteotomies and positioning of the implant components [Hafez et al., 2006]. Another drawback of PST; preoperative planning could not be modified intraoperatively. The 3D reconstruction data which are used to plan the virtual PST are based only on the bony

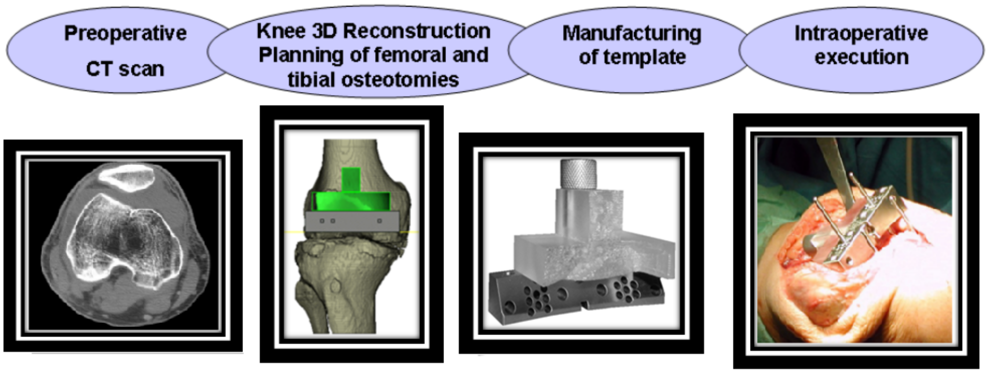

Figure 2.7: Patient specific template [Portheine et al., 2004]

structures. Therefore, this procedure sets an extra operation time for the surgeon to prepare the bone surface area for fitting exactly with the cutting block [Hafez et al., 2006]. Normally muscles, ligaments and cartilage are often best seen with an MRI, which offers advantages for surgical planning and customization of individual templates over CT-based approaches. Currently, the usage of MRI is limited for orthopaedic modelling purposes and mainly involved in diagnostic procedures.[Tomczak et al., 1997]. These applications are normally based on axial MRI images at the centre of the magnetic field with the assumption that spatial distortions at the borders of the field of View (FoV) have minor or no impact on diagnosis results. Geometric quality of MRI-based 3D anatomical models has been investigated in previous studies. White et al. performed specific dimensional measurements on ten ovines legs and found differences up to 10.9 mm between real bones and MRI-derived bone models manufactured using rapid prototyping. Furthermore, they found that the mean of all measurements taken from MRI was 3.5 percent smaller than the corresponding mean from the real bones [White et al., 2008]. Lee et al. evaluated the accuracy of combined CT-MRI models of six porcine femora using rigid body registration. Their evaluation in the joint region showed a matching deviation of (1.1 ± 0.3) mm in the global 3D contour-based measurements and (3.0 ± 1.8) mm in the local 2D contour-based measurement [Lee et al., 2008]. Moro-Oka et al. investigated the fidelity of MRI-derived bone models of the knee for motion measurement in three healthy subjects. Their results of comparing CT and MRI models of femur and tibia showed regions where the surfaces differed by several millimetres along with significant differences in the measurement of knee's kinematic parameters [Moro-oka et al., 2007]. Hinterwimmer et al. performed a comparison between MRI and long radiographs-based measurements using optimized MRI technique and found significant underestimation for leg length (2.5 ± 0.5) cm and for HKA-angle in valgus knees $(3.6 \pm 2.8°)$ [Hinterwimmer et al., 2008].

Among previous mentioned argumentations of phantom designs, see figure 4.1, a calibration body which are subjected for simultaneous scan with the patient's knee was not found. In the coming chapter, several ideas for such calibration body design was proposed. It presents the optimal phantom design which allows calibration of object specific distortion. To implement MRI-based planning on PST, patient specific geometrical distortion needs first to be quantified and corrected. The first investigation will be performed on a phantom model, and the figure 2.8 illustrates the concept of Master thesis in case of phantom study. The next coming chapter, i.e. chapter 3 deals with the major drawback of MRI, the geometrical distortion and in detail analyzes each sub-source.

In general medical diagnosis, surgery and treatment planning, Computer Tomography (CT) and Magnetic Resonance Imaging (MR) are widely used tools. For planning of osteotomies and placement of implant components, which is related to this thesis aim, accuracy is an extremely important issue to consider for the success of Total Knee Replacement (TKR) surgery. Particularly the geometry (location, shape and size) of anatomical structures that can be detected in the images has to be in agreement with the reference geometry of these structures in the patient.

It is essential in TKR-surgery the accurate representation of knee joint anatomical structures, which can be achieved today with CT-modality, but the lack of soft tissue information during planning can be achieved by MR-modality. Planning a TKR-surgery with help of individual template, relies on the basis of pre-operatively scanned MR images conveys geometric distortions. The spatial geometric distortions which present in MR images may seriously decrease the accuracy of the surgery, such as scaling and shearing distortions. Inhomogeneity of the static magnetic field and the imperfectness and non-linearity of the gradients, are the main reasons of why correction of the geometrical distortions [Breeuwer et al.].

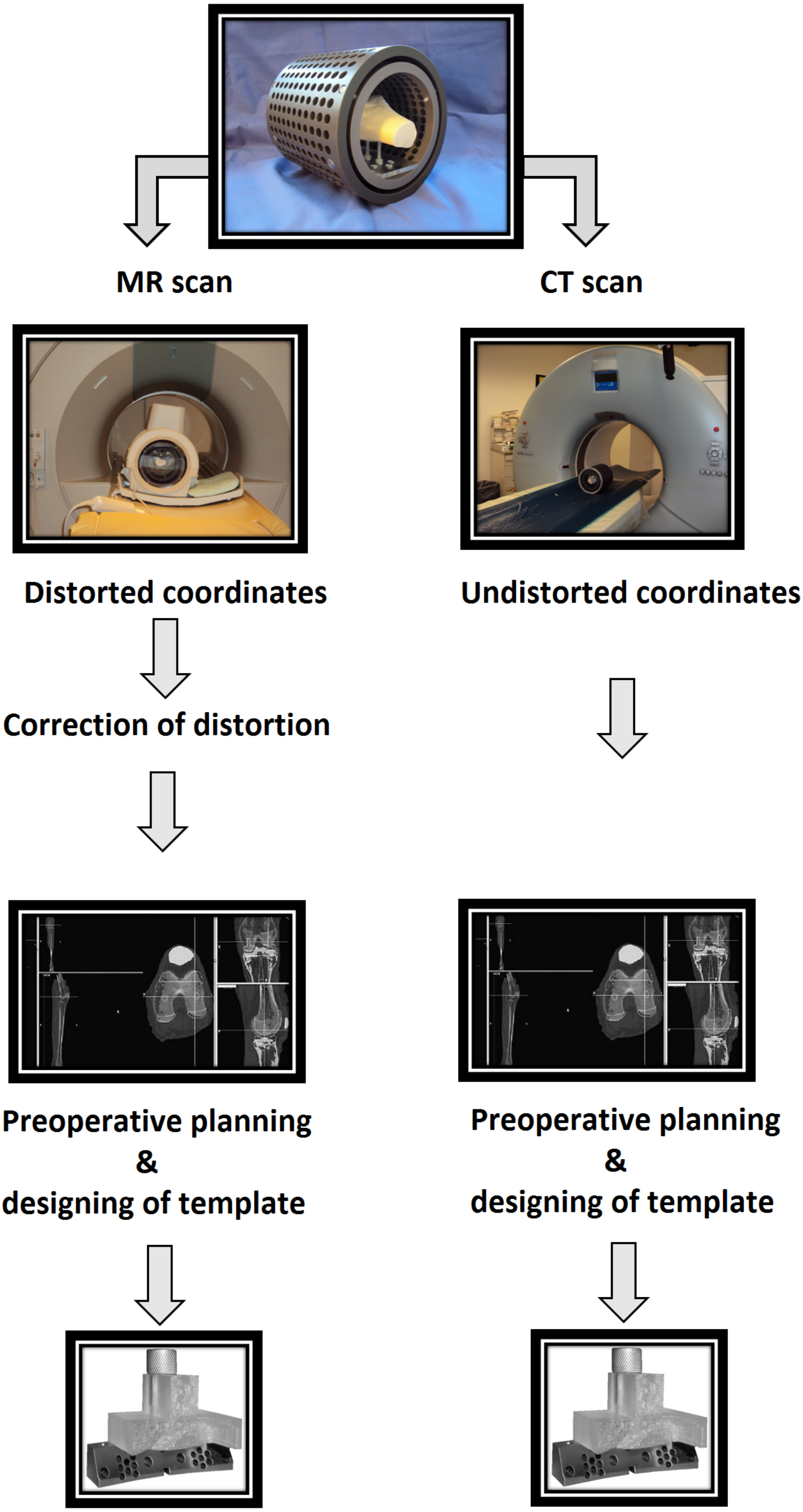

Figure 2.8: Concept of Master Thesis

3 Geometric Distortion

Nuclear Magnetic Resonance (NMR) modality just like other modalities does have some limitations: the limitations are related to the homogeneity of the field generating devices used to form the image. In other words, geometric distortion can arise from magnetic field inhomogeneity and the non-linearity of the gradient field. It can be a serious problem in some MRI applications where high geometric accuracy is required. In some cases, non-uniformity of the magnetic field can be large enough, for example in the presence of metal objects, to cause significant degradation of the image. Magnetic field inhomogeneities mean here the cause of dephasing of nuclear spins during data acquisition, which in turn leads to a loss of NMR signal. The final resulting effect is a noticeable reduction in image intensity. The distortion caused by gradient field non-linearity is very small near to the magnet centre or iso-centre, but increases when going away from the centre. It is strongest at the field of view boundary. There are built-in distortion correction systems which can correct the distortion caused by the gradient non-linearities. These systems do not correct distortions caused by magnet inhomogeneity, eddy currents or tissue susceptibility. Geometric distortion is in general the result of incorrect frequency-encoding. [Menuel et al., 2005; Vadim, 2000] Current generation of MRI scanners has been designed with short gradient rise times of less than 200 ms, that is in order to achieve shorter rise times and that affected the length of the gradient coils. The gradient design is restricted to be shorter and with fewer turns. Such restrictions have led to an increase in the gradient field nonlinearity which results in image distortions. The effects of the gradient field nonlinearity which is a consequence of imperfections and limitation of the gradient coil design, it depends on the geometry of the gradient coils and its effects are constant in time and independent of the imaging sequence which is used. Typical effect appears in the 2D image is called potato chip effect. Sumanaweera explained the effects of the gradient field nonlinearity with 2D MR scans that it clearly appear in three ways: First the barrel aberration which its size is around 4 mm within $(200 \times 200)mm^2$ field of view at the center of the gradients isocenter. Second the potato chip effect which is also around 4 mm for slices around 100 mm away from isocenter of the gradient coils, and finally the bow tie effect [Wang et al., 2004a; Sumanaweera et al., 1994b]. The most complex form of geometric distortion wit MR scanning is object-specific. This distortion is especially complex, because it depends on both the present material and the shape of the structure being imaged. The phantom-based quantifications are very useful to assess the general scan quality but they can not take into account the object dependent parameters, such as magnetic susceptibility differences, chemical shift and flow. Sumanaweera present a study of air-tissue and bone-tissue susceptibility effects. In this study, they conclude that the distortion at bone-tissue interfaces is negligible compared to the typical 1 mm MR image resolution, but the distortion at air-tissue interfaces has the size up to 2 mm. To correct those spatial mis-registrations due to susceptibility differences and chemical shift is possible by manipulation of the parameter settings of the used sequence during acquisition, but nevertheless one must still be careful because the air-tissue effect can be significant. Lüdeke have shown the local field deviation can be up to 10 ppm [Michiels et al., 1994; Ludeke et al., 1985; Sumanaweera et al., 1994b]. Furthermore, the geometric distortions can differ depending on the sequence. For example, geometric distortions due to the inhomogeneity in the main magnetic field and the susceptibility difference are less in spin echo sequences than gradient echo sequences. Therefore, the selections of sequence parameters along with optimized scanner calibration are therefore important optimization aspects.

3.1 What is geometric distortion

Geometric distortion means the spatial relationships between pixels in the image is not equal or equivalent to the spatial relationship between corresponding points in the scene. This distortion is described generally in more mathematical forms. The geometrical distortion is characterized by the spatial deviations or geometric errors [Wang et al., 2004a]:

$$dx(x,y,z) = x'(x,y,z) - x$$

$$dy(x,y,z) = y'(x,y,z) - x$$

$$dz(x,y,z) = z'(x,y,z) - x$$

$$dr(x,y,z) = \sqrt{dx^2 + dy^2 + dz^2} \tag{3.1}$$

Where $x'(x,y,z), y'(x,y,z)$ and $z'(x,y,z)$ are the coordinates in the space of the distorted image, and x, y, and z are the corresponding coordinates in the undistorted space. The positions of the phantom geometry are well defined, thus the geometric distortion can easily be mapped through the association between the pre-defined control points and the distorted image control points. The proportionateness can be described as follows:

$$dx_{ijk} = x'_{ijk} - x_{ijk}$$

$$dy_{ijk} = y'_{ijk} - y_{ijk}$$

$$dz_{ijk} = z'_{ijk} - z_{ijk}$$

$$dr_{ijk} = \sqrt{(dx_{ijk})^2 + (dy_{ijk})^2 + (dz_{ijk})^2} \tag{3.2}$$

Where x_{ijk} , y_{ijk} and z_{ijk} are the pre-defined coordinates by control points of phantom geometry and x'_{ijk} , y'_{ijk} and z'_{ijk} are the measured coordinates of the distorted image.

The description of geometric distortion effected by magnetic field non-uniformity is mathematically expressed as follows:

$$\vec{B} = \vec{B}_0 + \vec{B}'$$

Where $\vec{B}$ is unvarying and $\vec{B}'$ is a function of coordinates. MR imaging is usually performed in a homogeneous magnetic field such we can assume $\left|\vec{B}'\right| \ll \left|\vec{B}'_0\right|$, and the components of $\vec{B}'$ which are perpendicular to can be neglected for the reason of causing just a small disturbance of Larmor frequencies of the spins.

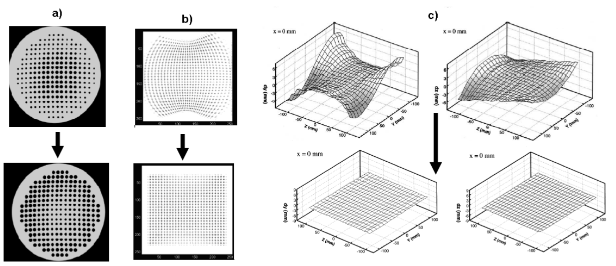

Figure 3.1: Geometric distortion before and after correction[Breeuwer et al.; Wang et al., 2004a]

3.2 Sources of geometric distortion

An image artifact is actually an undesired signal contribution or a visible structure which is added to the image, which does not exist in the real object or patient. Because of the pixels could be very noticeable or may be just few pixels out of balance which could confuse the pathology that may be mis-diagnosed at the end. In the last decades the frequency of occurrence and degree of severity of artifacts in MR images has been reduced significantly due to technical improvements in MR hardware and software. During the generation of MR images, artifacts could appear during one or more steps of the image generation process. This could be partly due to patient motion in the scanner, generation of RF pulses, and the involved processing steps like spatial encoding signal recording and image processing. Heterogeneity of the main magnetic field, eddy currents, nonlinearity of imaging gradients and other variety of reasons, both scanner and patient-related artifacts can degrade the quality of MR images [MR-tip, 2010.01.26].

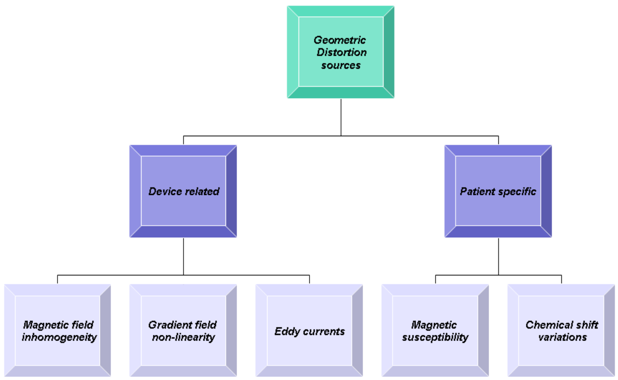

Figure 3.2: Sources of geometric distortion

Magnetic fields in MR scanners are often not homogeneous. This results in a subset of the dataspace that becomes more or less deformed. Especially when fast scan protocols are used, that is to prevent uncomfortable situations with respect the patient or when fast scanning is necessary to get valuable information. This kind of distortion source and four more main sources of geometrical distortion in MR systems, will be decribed in detail during this section.

3.2.1 Magnetic field inhomogeneity

All MRI imaging systems are supposed to have a homogeneous static magnetic field. An inhomogeneous static field leads to deformed images. This deformation can be either spatial, intensity, or both. The source behind intensity distortions is due to different field homogeneity around the imaged object and within it. Because the $T2^*$ in this area is different, and therefore the signal will be likely different. This means, if the homogeneity is less, the $T2^*$ will be less significant and the signal will be less. Geometric distortion results from long-range field gradients in B_o which is constant in time. The spins start to resonate at Larmor frequencies other than that set by an imaging sequence. The static field inhomogeneity is usually measured by the maximum deviation from considered field strength B_0 within a defined volume of interest, states:

$$\frac{|max(B_z(x,y,z))| - B_0}{B_0}$$

3.2.2 Gradient field non-linearity

Gradient coils in magnetic resonance imaging play an important role as other imaging parameters in requiring faster and stronger gradients. According to MR imaging principles, a spatially uniform static magnetic field and accurate magnetic gradient fields are required. In medical MRI systems equipped with superconducting magnets, geometric distortion due to gradient field non-linearity is usually much larger than that arising from the static field inhomogeneity, and is very small near to the magnet centre, but it increases when going off-centre. The strongest distortions appear near the device specific (FOV) boundary. It can be as large as 10 mm, so the correction of geometric distortion here is necessary. Using gradient coils with much better linearity and slower slew rate reduce the geometric distortion to about 4 mm. To meet this demand, shorter gradient coil structures with compromise in gradient field linearity is important issue to consider. The spatial characteristics of the gradient fields generated by a MR gradient sub-system can be described by the so called gradient coil tensor and defined as:

$$\begin{bmatrix} G_x(\vec{r}) \\ G_y(\vec{r}) \\ G_z(\vec{r}) \end{bmatrix} = \begin{bmatrix} L_{xx}(\vec{r}) & L_{xy}(\vec{r}) & L_{xz}(\vec{r}) \\ L_{yx}(\vec{r}) & L_{yy}(\vec{r}) & L_{yz}(\vec{r}) \\ L_{zx}(\vec{r}) & L_{zy}(\vec{r}) & L_{zz}(\vec{r}) \end{bmatrix} \begin{bmatrix} G_x \\ G_y \\ G_z \end{bmatrix}$$

where $G_i(i = x, y, z)$ are the components of the actual gradient generated by the gradient coils $(X, Y,$ and $Z)$ and G_x,G_y and G_z are the nominal gradient strength. If these gradients are perfectly linear, the gradient coil tensor is reduced to the $3x3$ identity matrix I. So the gradient coil tensor $L(r)$ can be decomposed into a linear part and non-linear part which is denoted as $L(\widetilde{r})$.

$L(r) = I + L(\widetilde{r})$

where

$$\begin{bmatrix} 1 & 0 & 0 \\ 0 & 1 & 0 \\ 0 & 0 & 1 \end{bmatrix}$$

and

$$L(\widetilde{r}) = \begin{bmatrix} L_{xx}(\vec{r})^{-1} & L_{xy}(\vec{r}) & L_{xz}(\vec{r}) \\ L_{yx}(\vec{r}) & L_{yy}(\vec{r})^{-1} & L_{yz}(\vec{r}) \\ L_{zx}(\vec{r}) & L_{zy}(\vec{r}) & L_{zz}(\vec{r})^{-1} \end{bmatrix}$$

$L(\widetilde{r})$ provides a complete description of the gradient field non-linearity. This non-linear part can cause a range of unwished effects including geometric distortion in MR images.

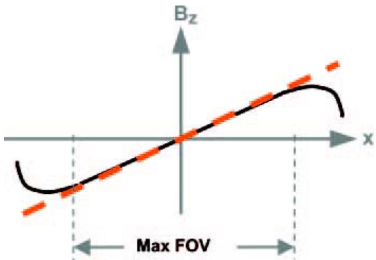

Figure 3.3: Schematic shows the geometric distortion of a typical gradient profile along the x-axis, with decreasing linearity (solid line) as the distance from the magnet isocenter increases. The red dotted line shows the desired linear gradient profile [Mahesh, 2004]

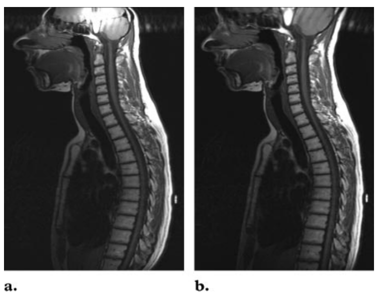

Figure 3.4: Gradient field non-linearity artifact. a)MR image obtained with SE sequence and large field of view, b) Image obtained with a vendor-supplied correction algorithm shows correction of the geometric distortion [Mahesh, 2004]

3.2.3 Eddy currents

Eddy currents are induced in conductive material within the scanner every time a gradient is changed in the course of the scanning process. As eddy currents cause dynamic magnetic fields, geometrical distortions arise. Errors due to eddy currents are obviously dependent on the actual imaging sequence and its parameterization. The fast acquisition strategies are very sensitive to eddy currents. Significant distortions in the phase-encoding direction can be caused by those eddy currents when the image bandwidth is quiet low. Methods for reducing this effect have been already addressed in previous work. Some of them simply involve the modifications of the gradient sequences. These approaches are not adequate to completely remove this artifact. Other approaches can be considered as registration methods which partly rely on MR physics and require additional experimental data. Others simply use a distortion geometric model inferred from the acquisition principle, which leads to estimate a few parameters using a standard similarity measure like cross-correlation.[Mangin et al., 2001]

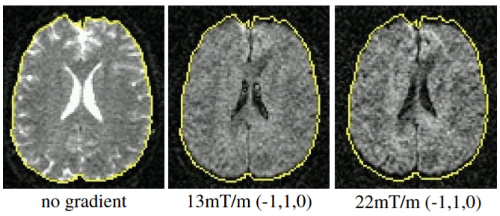

Figure 3.5: Eddy-current related distortions [Mangin et al., 2001]

3.2.4 Magnetic susceptibility

The degree of magnetization of a material due to the magnetic field is known as a magnetic susceptibility. Susceptibility artifact occurs if the static magnetic field is not perfectly uniform. This kind of non-uniformity may be a result of imperfections in the magnet itself, but it is more often due to the imaged object, i.e. at the boundaries between tissues with different magnetic susceptibilities like air/tissue. At this boundary the magnetic field is distorted because there are macroscopic field gradients. Stronger artifacts are seen around metallic and ferromagnetic objects within the body, which is because the susceptibility of metal is much higher than that of soft tissue. As outcome, the magnetic field lines bend into the object and this result in stronger and weaker fields at various locations around the object. Medical devices in or near the magnetic field or implants of the patient is a major reason for susceptibility artifacts. These materials distort the linear magnetic field gradients, which results in bright areas which are mis-registered signals and dark areas. To decrease the susceptibility artifact, spin echo should basically be used rather than gradient echo sequences. Reduction of echo time and increasing the readout bandwidth keeps the susceptibility artifact very small. Magnetic susceptibility effect has also been accounted one of the main reasons behind geometric distortion.

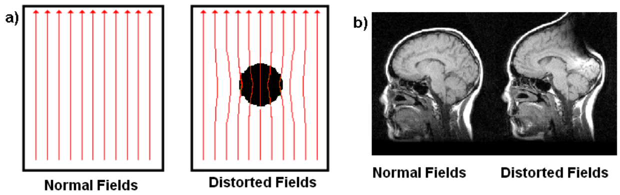

Figure 3.6: Normal and distorted magnetic field because of susceptibility phenomenon [Hornak]

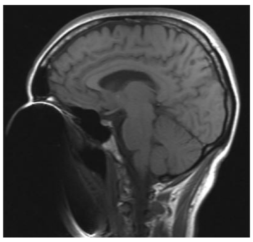

Figure 3.7: Sagittal MR image shows a magnetic susceptibility artifact that resulted from the presence of metallic dental fillings [Mahesh, 2004]

3.2.5 Chemical shift

Chemical shift is appearing because of different chemical environments of fat and water. Fat consists of hydrogen linked to carbon, whereas the hydrogen of water is linked to oxygen, and that results in different frequency precessions. Fat processes at a lower frequency than water. This artifact is recognized by dark edge at the interface between fat and water and occurs only at the frequency encoding axis. Chemical shift can be reduced by scanning at lower field strength and by keeping the FOV to a minimum. In case of using higher magnetic fields, manipulating the size of the bandwidth is one way of reducing chemical shift and keeping good SNR. [Westbrook et al., 2005; e-MR, 2010.01.26]

4 State of the art

Many authors reported in their publications that the main sources of spatial distortions are the inhomogeneity in the main magnetic field, nonlinearity of the gradient fields and the eddy currents due to the switching of the gradients. Field strength, materials and their distribution within the scanned object are among some factors which cause magnetic field inhomogeneity [Heiland, 2008; Hornak; Wang et al., 2004a].

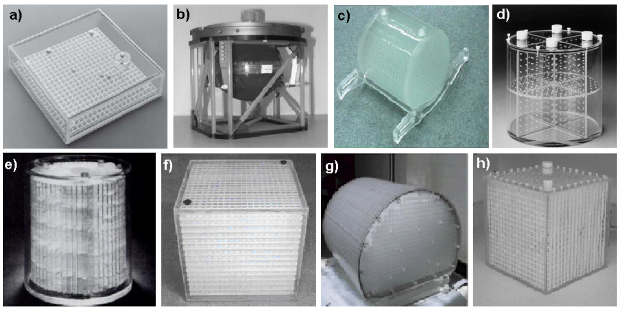

Figure 4.1: MR-compatible phantom designs: a.[supertech, 2010.03.22] b.[Orth et al., 1999] c.[Breeuwer et al., 2002] d.[Dataspectrumcorporation, 2010.01.26] e. [Gray und Felmlee, 1987] f. [Wang et al., 2004a] g.[Yan et al., 2006] h. [Sumanaweera et al., 1994b]

4.1 Correction methods and phantom designs

Geometric accuracy of MR images has long been an issue of concern, particulary for radiation therapy, MR neuro-imaging, target localization of lesions and for accurate planning of osteotomies and placement of implant components. That is due to a combination of some factors. Caramanos has reported some of them. First, the precision and accuracy can be affected by non-linear gradient distortions which are typical occuring with the newer scanner generation within gradient systems that are designed to have short bores, in order to save less space. Short gradient rise times in order to acquire faster images for functional MRI, diffusion tensor imaging, and MRI of the heart.[Wang et al., 2004a; Caramanos et al., 2009] Research studies have been done about the quantification and the correction of the geometric distortion in MR images.

Several authors have already proposed correction schemes. Two major design approaches have been employed; one approach uses square grids, and the other uses cylindrical rods or capillary tubes.[Price et al., 1990; Kawanaka und Takagi, 1986; Menuel et al., 2005; Breeuwer et al., 2002; Yan et al., 2006] Wang provided a comprehensive and accurate measurement of the geometric distortion in MRI by developing a 3D phantom. To study geometric distortion in MRI, Breeuwer et al. used spheres of a certain size arranged in three dimensions. Doran used a custom-built phantom with three orthogonal grids of fluid-filled rods for the gradient wrap correction purpose. Jovichich has quantitatively characterized and correct site-specific image distortions which caused by gradient non linearity by using a special cylindrical phantom. Michiels quantified the effects of the machine-dependent parameters by using especially designed phantom containing a rectangular grid of parallel water-filled rods; by comparison the measured positions of the rods in the image with their exact calibrated positions. Furthermore, Yu et al. present the results of a phantom study for examining the stereotactic accuracy of the Leksell system by using CT and 2 different MR systems. The phantom used in this study is for the purpose of assessing errors arising from field inhomogeneity and gradient field nonlinearity [Wang et al., 2004b; Doran et al., 2005; Jovicich et al., 2006; Michiels et al., 1994].

Table 4.1 illustrate a literature research of the phantom designs and related correction methods. The following table summerize some of the previous done work in the field of MR distortion correction. As seen, most of the phantom designs are either in cubical, cylindrical or spherical shape. That is because it has to fulfill the recommendation of AAPM according to spatial linearity and quality control phantoms. The ideas from the previous done phantom bodies are applicable on this case study. Furthermore, some limitatons according to the shape, size and motivation for this study have to be considered while designing a new calibration phantom. Among previous mentioned argumentations of phantom designs, a calibration body which are subjected for simultaneous scan with the patients knee was not found. In the coming chapter, several ideas for such calibration body design was proposed. It presents the optimal phantom design which allows calibration of object specific distortion.

The built-in distortion correction systems which exist today in MR scanners are able to correct the distortions due to gradients and magnetic fields. Furthermore, these systems are not able to correct specific distortions caused by either a patient or an object. To achieve specific estimation of the distortion's amount and later on correction of the deformations; a special designed tool with known dimensions has to be scanned with the patient-object, and this tool is considered as a reference body. The correction can be achieved according to the pre-known geometries of the reference body, which allows the individual correction of the geometrical distortions.

Paper	Year	Author	Motivation	Distortion source	Correction method	Results
Detection and correction of geometric distortion in 3D CT/MR images	1999	Marcel Breeuwer, Waldemar Zylka John Wadley Andreas Falk	For medical diagnosis and planning of medical treatment and during the actual treatment	In homogeneity of the static field and imperfectness and non-linearity of the gradients	3D phantom with regular spaced ball-shaped Perspex structures 	The average distortion remaining after image correction was in order of 0.2 mm reduced from 4.5 mm
Development of a unique phantom to assess the geometric accuracy of MRI for stereotactic localization	1999	Robert C., Sinha Praveen, Madsen Ernest, Frank Gary, Korosec Franc R, Mackie Rockwell, Mehta Minesh	For clinical application such as advanced image-guided neurosurgical procedures, radio-surgical procedures	Magnetic field distortions and susceptibility artefacts	Anthropomorphic head phantom consisting of 2D-lattice of acrylic spheres 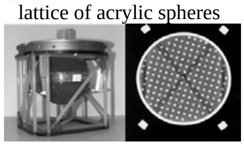	Average errors were less than 1 mm in all directions.
A phantom study of the geometric accuracy of CT and MRI stereotactic localization with the Leksell stereotactic system	2001	Cheng Yu, Michael Apuzzo, Chi-Shing Zee, Zbigniew Petrovich	For target localization of intracranial lesions in stereotactic radio-surgery	Magnetic field in homogeneity and gradient nonlinearities	3D phantom was constructed in the shape of a box, 164 mm in each dimension, with three perpendicular arrays of solid acrylic rod, 5 mm in diameter and spaced 30 mm apart within the phantom	Mean values of max errors were 0.9mm 0.2 mm and 1.9 mm in x, y & z-direction.
Assessment of geometrical accuracy of MRI images for radiation therapy of lung cancers	2003	N. Koch, H. H. Liu, L. E. Olsson,2 and E. F. Jackson2	For the purpose of radiation therapy treatment planning for lung cancer	Magnetic field in homogeneity and gradient field nonlinearities	Phantom with vials to approximate the geometry of the upper thorax 	fGRE sequence exhibited no errors .2.0 mm in the sagittal and coronal planes, whereas the FSE sequence produced images with errors between 2.0 and 4.0 mm
A novel phantom and method for comprehensive 3D measurement and correction of geometric distortion in magnetic resonance imaging	2004	Deming Wang David M. Doddrell Gary Cowin	For clinical and research settings, such as in MR neuro-imaging	magnetic field in homogeneity and gradient field non-linearity	3D phantom consists of a set of three orthogonal planes 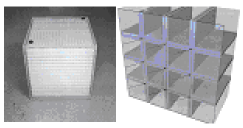	Mean errors were in order of 0.1 mm or less, which were less than 1/10:th of the voxels's dimensions of the phantom image, reduced from 10 mm
A proposed scheme for comprehensive characterization of the measured geometric distortion in MRI using a 3D phantom	2004	Deming Wang, David Doddrell	MRI quality assurance, Spatial localization and image based quantification	Magnetic field in homogeneity and gradient nonlinearities	3D phantom consists of a set of three orthogonal planes 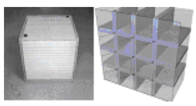	The proposed scheme provides a comprehensive assessment of the GD. The scheme can be potentially used as a standard procedure.

Characterization and correction of distortions in stereotactic MRI for bilateral sub-thalamic stimulation in Parkinson disease	2005	Carole Menuel, Line G. Eric Bardient, Fabrice Poupon, Daniel Phalippou, Didier Dormont	For targeting of the sub-thalamic nucleus for treating Parkinson disease	Magnetic field in homogeneity and gradient nonlinearities	3D phantom in cubical shape 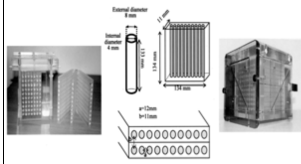	Average errors were < 1 mm in all directions, which represents 60.75 % 78.74% 61.18 % in x, y and z-directions.
Geometric distortion in structural MRI	2005	Deming Wang, David Doddrell	For stereotactic localization in radio-surgery and MR image guided biopsy	Gradient field nonlinearities, static field in homogeneity	3D phantom consists of a set of three orthogonal planes 	Errors were below 0.8mm and the average errors within a value of 0.5mm in all directions
A complete distortion correction for MR images: I Gradient warp correction	2005	Simon Doran, Liz Charles-Edwards, Stefan Reinsberg, Martin O Leach	Correcting extra-cranial images, with large distortions (> 25 mm) due to large FOV and for planning of radiotherapy treatments	Magnetic field in homogeneity induced by the imaged object and gradient nonlinearities	3D linearity test object 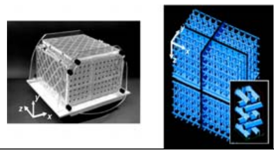	Mean error in x-coord. Over 365x230x340 mm cubic, is 0.6mm, equal to 1/3 of the voxel width in the original MRI-data set.
Investigation of MR image distortion for radiotherapy treatment planning of prostate cancer	2006	Z Chen, C-M Ma, K Paskalev, J Li, J Yang, T Richardson, L Palacio, X Xu, L Chen	Planning for Radiotherapy of prostate cancer	Magnetic field in homogeneity and gradient nonlinearities	Open MR unit with F18 phantom 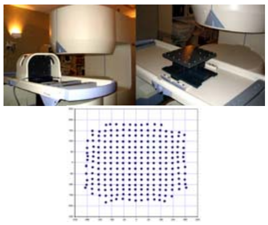	After using Gradient Distortion correction software built within the scanner, the residual distortions were <5 mm for a standard 48 cm FOV
Gradient distortion correction for low frequency current density imaging	2006	Charles X.B. Yan, Tim DeMonte, Michael L.G. Joy	For Current density imaging; technique that uses MRI to measure the distribution of externally applied electric current inside the tissues.	Distortion due to Gradient field nonlinearity	Cylindrical calibration phantom with 3D grid of acrylic spheres with 8 mm in diameter and regularly spaced 15 mm center-to-center 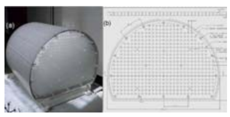	GDC method corrects the mis-registration and derivative distortion problems associated with distorted current density images.
Characterization, prediction and correction of geometric distortion in 3T MR images	2007	Lesley Baldwin, Keith Wachowicz, Steven Thomas,	For the purpose of image guidance in radiation treatment planning	Magnetic field in homogeneity and gradient nonlinearities	3D grid phantom with CT and MR image 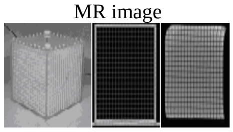	Mean distortions were reduced fr. 1.63-0.29 mm <1 pixel of residual distortion)

Table 4.1: summary of previous work on phantom designs and correction methods

5 Material and Method

5.1 Calibration phantom design

To solve the problem with MR spatial linearity, first we need a precise detection procedure which can be used to evaluate the geometrical distortion. To achieve that, a suitable phantom design with MRI-compatible materials is required for this procedure. Based on literature research it has been found out that, the most effective and common approach is the choice of a phantom which consists of a regular array of objects (3D-grid, spheres, rods or tubes) of known dimensions and spacing, moreover the phantom should be filled with a signal producing material. 3D Phantom shape varies, depending on work purpose, but the most common shapes are cubical, cylindrical and cuboid ones. There are numerous materials which have been used successfully as NMR contrast agents. They have primarily consisted of oils, gels and water solutions of various paramagnetic ions. The materials are discussed later in this section. Another issue is dealing with the phantom design. Most phantoms are made out of a combination of a single signal-producing material and a non-signal producing material. MR images of such a phantom shows changes in geometric accuracy, and these changes were visually confirmed on MR images of the phantom.

5.1.1 General phantom requirements

Spatial linearity is one of many issues which should be considered concerning the choice of phantom material and design. Spatial linearity is the degree of geometrical distortion presented in images, which refers to either displacement of phantom patterns (grid) within an image relative to their known location, or improper scaling of the distance between predefined image points. There are some requirements which are great of importance regarding the choice of the phantom material. For example, avoiding the use of colored plastics or other container materials, which possess significantly different magnetic susceptibility due to the filling materials. At each operating field intensity, it is recommended that the chosen NMR contrast materials exhibits the following characteristics, see table 5.1. Successfully NMR contrast agents can consist of gels, oils and water solutions of different paramagnetic ions. The phantom which is used to measure

100 ms < T_1 < 1200 ms	50 ms < T_2 < 400 ms	Proton density $\approx H_2O$

Table 5.1: Characteristics should be fulfilled by NMR material [Price et al., 1990]

Agent	Characteristic
Water	High proton density, Long T1 and T2
Water + paramagnetic agent (e.g. Ni, Cu, Gd)	Shorter T1 and T2
Gel (e.g. agarose) + paramagnetic agent	Independent adaptation of T1 and T2
Any of these above + NaCl	Adaption of electric conductivity
Oil	Fat simulation

Table 5.2: Phantom materials and their characteristics [Price et al., 1990]

spatial linearity should occupy at least 60 % percent of the largest field-of-view and consist of an NMR-compatible regular and rigid array of grid sheets, rods, tubes or spheres. These objects have known predefined dimensions and spacing, and the phantom should be filled with strong signal producing material (high contrast), which could be $CuSO_4$, $NiCl_2$, Propanediol, $MnCl_2$, deionized water, agar gel, polyvinyl alcohol gel, etc), see table 5.2. The plates of the phantom and the array should not emit NMR signal (solid support structures), it could be like acryl poly-methyl-methacrylate (PMMA), Perspex sheets or PVC Plexiglas. Scan conditions are another important issue to consider. While optimizing the phantom's design, considerations should be taken into account to determine the spatial linearity for a typical multi-slice acquisition with the largest available image matrix to maximize resolution. According to the volumetric imaging technique of NMR, the evaluation should be performed for each orthogonal plane to define the useful imaging volume. Spatial linearity is not expected to be depended significantly on image timing parameters such as TE, TR and the number of signal acquisitions, [Price et al., 1990]. For general phantom requirements see table 5.3.

Application-related	Protocol-related	Geometry-related	Material-related
Cover ROI (for example: anatomical knee compartments required for total knee arthoplasty)  	Phantom design should allow detection of grid or patterns on required slice orientation (coronal, sagittal, axial)	Phantom should fit into the knee coil (inner d = 17.5 cm, length = 23 cm)	Hard outer structure could be from Plexiglas, Perspex or PPMA
Find the optimal grid density which assures the compensation of the distortion with acceptable remaining error.	Slice thickness of the phantom should be at least twice the maximum slice thickness for single-slice measurements, plus the image volume length for multi-slice measurements (according to AAPM).	Phantom with cylindrical rods with same diameter and contrast agent. Rods e.g. (d = 5mm, length = 15 cm)	Acrylic cylindrical rods
Allow distortion measurement in (x,y,z) directions in case of 3D-data acquisition.	Specific knee protocols (those with fat suppression) should be considered while choosing phantom materials to avoid undesired effects.	Distance between two rods = 20 mm (according to AAPM) 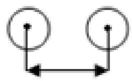 **20 mm** Should be adjusted for our design conditions.	Signal producing agent recipe according to AAPM: 1 litre Water 3.6 g NaCl 1.25 g $CuSO_4$ (1.96 g $CuSO_4$ x 5 H_2O) → T1 = T2 = 200 ms
Easy and simple set-up			
Rigid design			

Table 5.3: General phantom requirements

5.1.2 Specific phantom requirements

The specific requirements can be divided into four major categories; application related requirements, scan related requirements and geometry and material related requirements. The phantom shall cover the whole anatomical region of interest (ROI) where the distortion should be compensated and at the same time it shall fulfill the application-specific requirements (i.e. in case that the correction of MR-images of the knee joint is needed, the knee coil geometry should be considered for the phantom design since the phantom should fit inside the coil). Grid density of the phantom varies, depending on the volume of the imaged object and the requirements for the distortion quantification and correction. The effect of the grid density on the quantification and correction of the distortion could be investigated in computer simulation. Measuring errors in three directions is necessary for 3D data acquisition. The phantom should also be constructed of MR compatible materials, being as rigid as possible and at the same time easy to use. Phantom design should allow detection of grid or patterns on required slice orientation (coronal, sagittal, axial), and slice thickness of the phantom should be at least twice the maximum slice thickness for single-slice measurements, plus the image volume length for multi-slice measurements according to AAPM. AAPM stands for American Association of Physicists in Medicine; it is a standard for quality assurance methods and phantoms for MR imaging. Other standards exist like National Electrical Manufacturers Association (NEMA), European Economic Community (EEC) and American College of Radiology (ACR). According to AAPM, the standard distance between the rods is between one and two centimeters, that is for phantoms to be imaged inside the whole body magnet. Because this phantom will be much smaller, the distance between two rods is assumed, from centre to centre of the rods, would be about some millimeters. AAPM standard for this point should be adjusted for the specific phantom.

5.2 Experimental simulations with Matlab

As mentioned before, the short term goal and focus in this work is to quantify the amount of distortion and investigate the effectiveness for a non-rigid registration method based on the thin plate spline, to calculate the corrective transformation which aims to compensate the distortion. After the analysis of the general and specific requirements for the phantom design where chapter 5.2.3 discuss as well various design possibilities, it is suitable to use a cylinder-shaped construction with grid patterns distributed on its surface. The suggested phantom construction contains two grid of patterns. In this study the markers of the outer grid will be used for two purposes: 1) the quantification of the amount of distortion by comparing markers extracted from MRI to both CT-extracted markers and the reference phantom geometry and 2) for calculation of corrective non-rigid transformation. The markers of the inner grid where used for evaluation of the effectiveness of the proposed correction method. During this chapter some simulation experiments were performed in order to get a first impression about optimal grid density and the effectiveness of the used correction method. The subsequently following sub-chapter present the performed simulations step-by-step. Results of simulations on three different grid densities and the effectivity of the correction method have been computed.

5.2.1 Simulation steps

This chapter presents the performed simulation step-by-step; a) application of parabola-shaped distortion on an cuboid containing the two grid of the phantom, b) based on TPS the calculation of the corrective transformation using the markers of the outer grid, c) evaluation of the proposed correction method using both outer and inner grid, d) evaluation on the cuboid VOI inside the inner cylinder, e) evaluation on a model of the bone to get first impression how this looks like for surface correction. Step 1 in figure 5.1 illustrates the simulated MRI distortion which is applied on the phantom. The phantom is prepared to be distorted by using the green and red points, which represent reference and selected points, follow step 2 and 3 in figure 5.1. After application of the distortion on both cylinders, see figure 5.2, Thin Plate Spline correction method was applied on the outer and on the inner cylinder, see step 5 and 6 in figure 5.2. Furthermore, distortion application and correction was applied on a cuboid volume of interest, see figure 5.3. Later on, four evaluations were performed. First evaluation was applied on the inner cylinder, second evaluation on the outer cylinder, third evaluation was applied on a cuboid volume, and last evaluation was applied on a knee model, see the last steps in figure 5.4. For all four evaluations, minimum, maximum, mean, standard deviation and RMS were calculated both before and after correction on the Euclidian distances.

$$dr_{ijk} = \sqrt{(dx_{ijk})^2 + (dy_{ijk})^2 + (dz_{ijk})^2} \tag{5.1}$$

Where x_{ijk} , y_{ijk} and z_{ijk} are the predefined coordinates by control points of phantom geometry and x'_{ijk} , y'_{ijk} and z'_{ijk} are the measured coordinates of the distorted image.

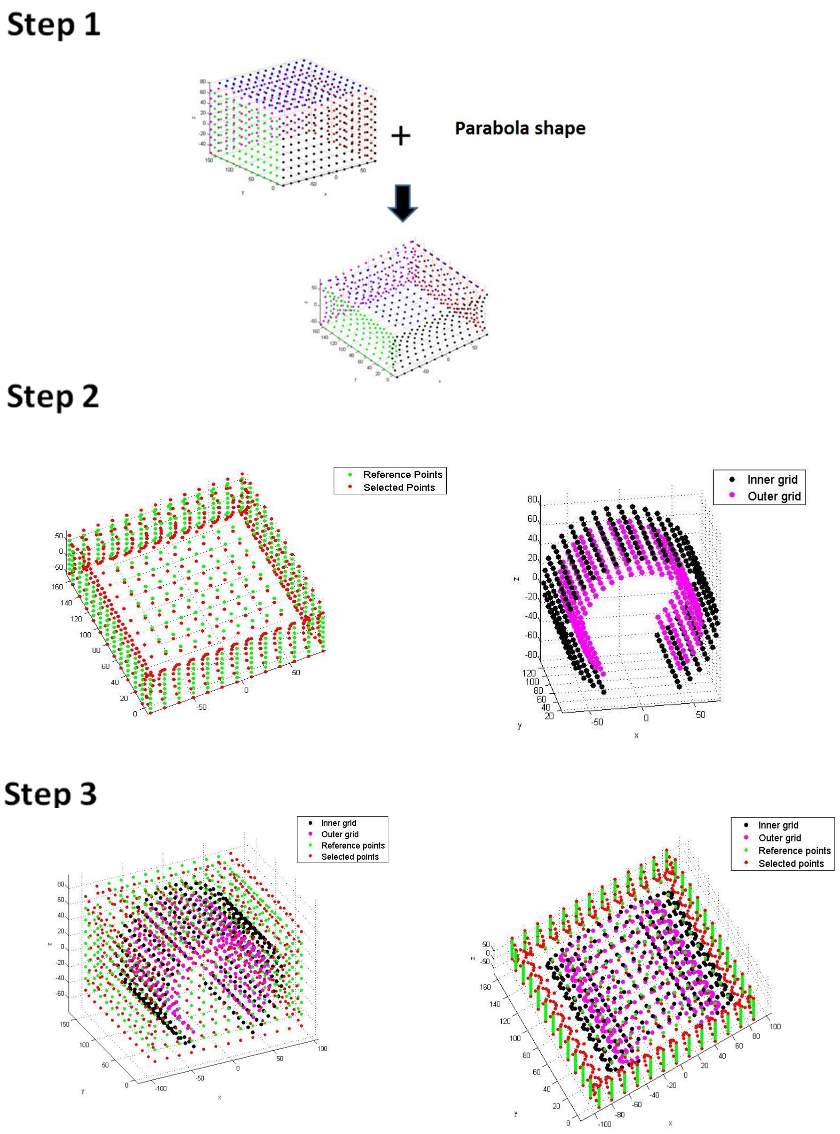

Figure 5.1: Experimental simulation; step.1 Simulation of geometric distortion. step.2 Reference and selected points are prepared for distortion and correction application. step.3 Inner and Outer coordinates of the phantom prepared to be distorted/corrected

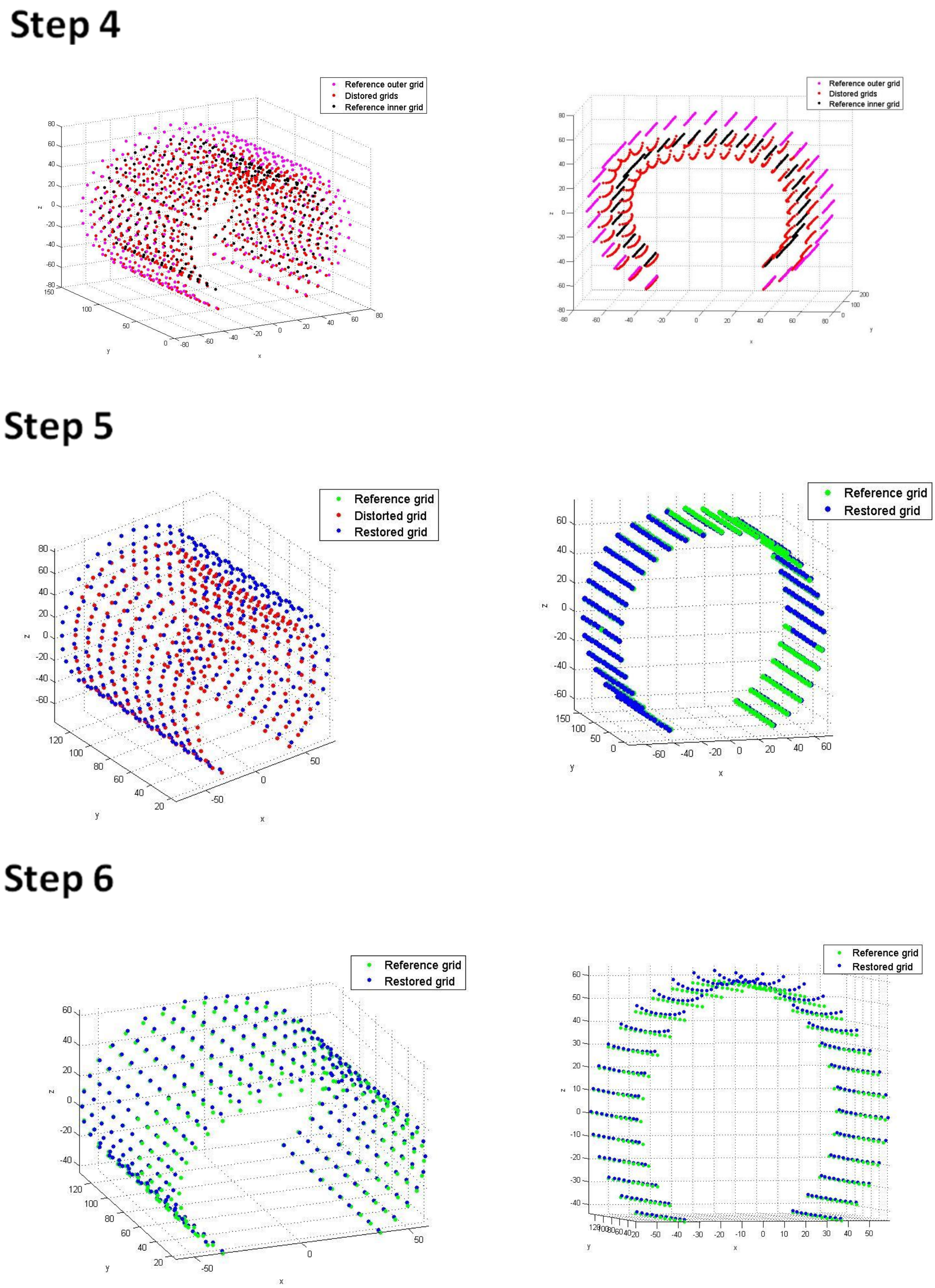

Figure 5.2: Distortion and correction steps; step.4 Distorted inner (left) and outer grid (right). step.5 Corrected outer grid. step.6 Corrected inner grid

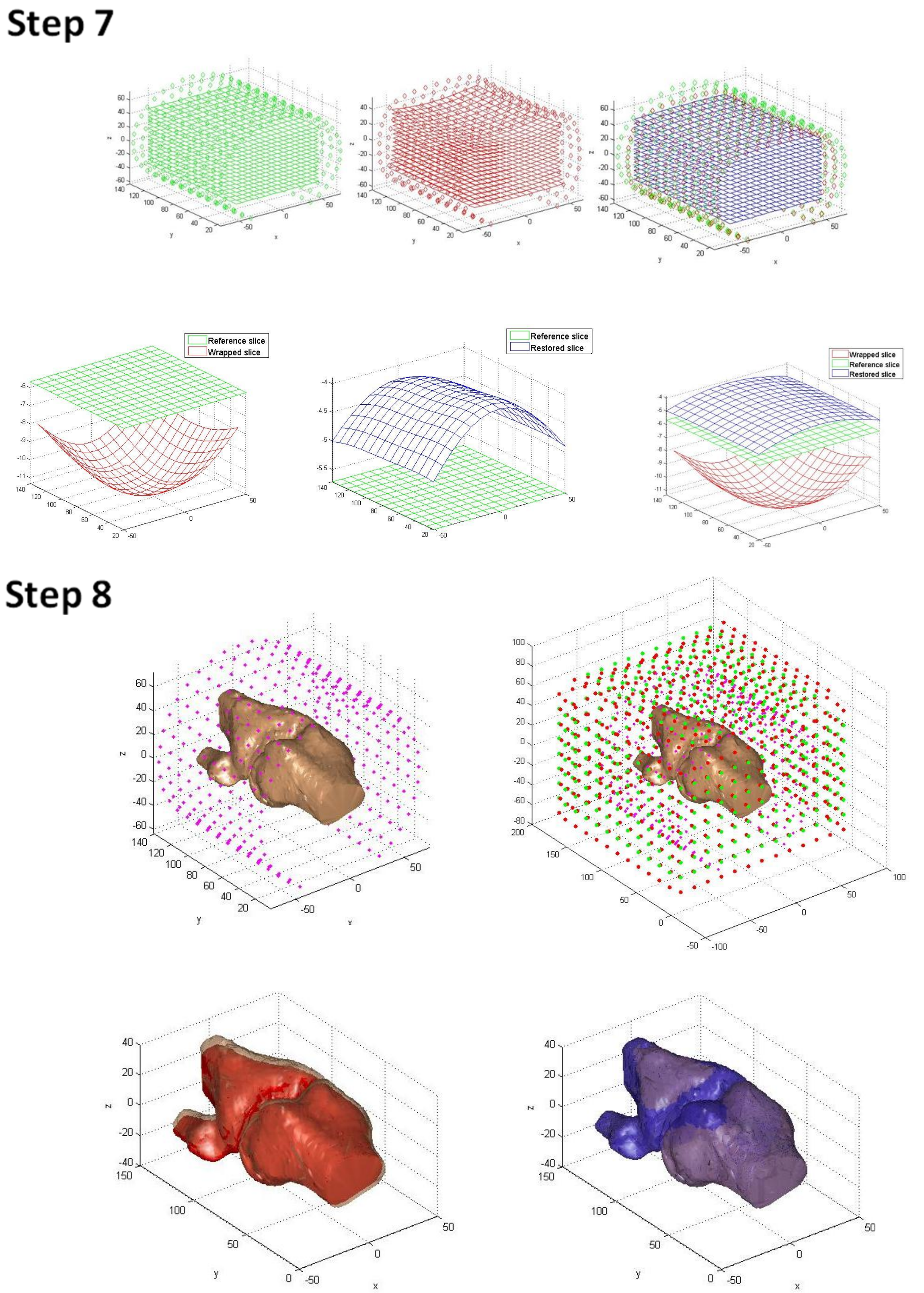

Figure 5.3: Simulation on a cuboid ROI inside the inner grid and on a knee model; step.7 Original, distorted and corrected cuboid VOI and result of distortion correction on a 2D slice (slice Nr.5) from the VOI. step.8 Simulation of distortion and correction on the surface of a knee model

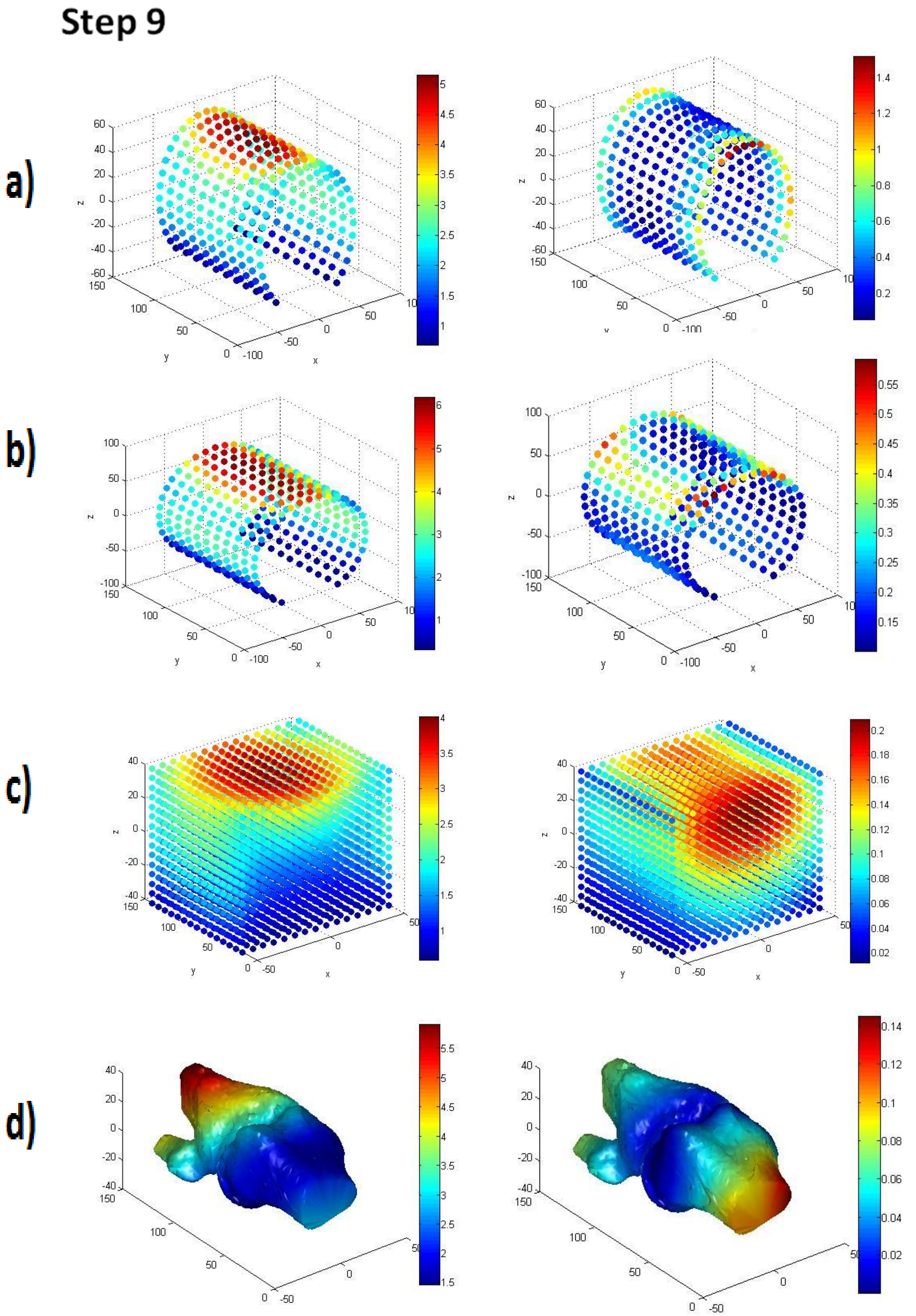

Figure 5.4: Visual evaluation of the proposed correction method;; step.9 a) Evaluation on the inner grid. b) Evaluation on the outer grid. c) Evaluation on the VOI. d) Evaluation on the knee model

5.2.2 Simulations on grid density

Three simulations were performed on the coordinates of the phantom for the purpose of finding optimal grid density. Same simulation procedure was applied on the inner grid, outer grid, on a cuboid volume and finally on a knee model. Results of the simulated coordinates are shown in table 5.4, 5.5, 5.6 and 5.7. Results of simulation on the inner and on the outer cylinders are illustrated in figure 5.5. Results of simulation on VOI and on knee model are illustrated in figure 5.6. Increasing or decreasing the number of control points gives no significant effect after correction. As seen in figure 5.5, the amount of distortion decreased from 5 mm to 1.4 mm for the inner grid. The error of the outer grid was decreased from 6 mm to 0.55 mm. For the VOI, the error decreased from 4 mm to 0.2 mm, and for the knee model decreased from 5.5 mm to 0.12 mm.

Summary of statistical data (μ, σ, Max, RMS) of the absolute errors in the simulated coordinates of the Inner grid compared between before and after correction				
Before correction	μ [mm]	σ [mm]	Max [mm]	RMS [mm]
First simulation: 26 x 24 x 8	2.5546	1.0858	5.1572	2.7747
Second simulation 31 x 29 x 11	2.5864	1.0874	5.1585	2.8050
Third simulation: 36 x 34 x 14	2.6058	1.0869	5.1736	2.8230
After correction	μ [mm]	σ [mm]	Max [mm]	RMS [mm]
First simulation: 26 x 24 x 8	0.4329	0.2789	1.4966	0.5146
Second simulation 31 x 29 x 11	0.4159	0.2622	1.5132	0.4915
Third simulation: 36 x 34 x 14	0.4070	0.2525	1.5283	0.4789

26 x 24 x 8
31 x 29 x 11
36 x 34 x 14

Outer grid points in xy-direction x
Inner grid points in xy-direction x
Nr. of points in z-direction

Table 5.4: Evaluation of the correction at the corrdinates of the inner grid for the three different grid densities

Summary of statistical data (μ, σ, Max, RMS) of the absolute errors in the simulated coordinates of the Outer grid compared between before and after correction				
Before correction	**μ [mm]**	**σ [mm]**	**Max [mm]**	**RMS [mm]**
First simulation: 26 x 24 x 8	**2.6722**	**1.5864**	**6.1968**	**3.1057**
Second simulation 31 x 29 x 11	**2.7032**	**1.5865**	**6.2038**	**3.1332**
Third simulation: 36 x 34 x 14	**2.7225**	**1.5854**	**6.2170**	**3.1497**
After correction	**μ [mm]**	**σ [mm]**	**Max [mm]**	**RMS [mm]**
First simulation: 26 x 24 x 8	**0.2342**	**0.1042**	**0.5933**	**0.2563**
Second simulation 31 x 29 x 11	**0.2335**	**0.1010**	**0.5933**	**0.2543**
Third simulation: 36 x 34 x 14	**0.2332**	**0.0993**	**0.5933**	**0.2534**

26 x 24 x 8
31 x 29 x 11
36 x 34 x 14

Outer grid points in xy-direction x
Inner grid points in xy-direction x
Nr. of points in z-direction

Table 5.5: evaluation of the correction at the corrdinates of the outer grid for the three different grid densities

Summary of statistical data (μ, σ, Max, RMS) of the absolute errors in the simulated coordinates of the cuboid VOI compared between before and after correction

Before correction	μ [mm]	σ [mm]	Max [mm]	RMS [mm]
First simulation: 26 x 24 x 8	1.8124	0.7107	4.0133	1.9467
Second simulation 31 x 29 x 11	1.8163	0.7123	4.0209	1.9509
Third simulation: 36 x 34 x 14	1.8182	0.7131	4.0250	1.9530

After correction	μ [mm]	σ [mm]	Max [mm]	RMS [mm]
First simulation: 26 x 24 x 8	0.1086	0.0454	0.2053	0.1177
Second simulation 31 x 29 x 11	0.1104	0.0460	0.2093	0.1196
Third simulation: 36 x 34 x 14	0.1114	0.0464	0.2116	0.1207

26 x 24 x 8 31 x 29 x 11 36 x 34 x 14	Outer grid points in xy-direction x Inner grid points in xy-direction x Nr. of points in z-direction

Table 5.6: evaluation of the correction at the corrdinates of the cuboid volume for the three different grid densities

Summary of statistical data (μ, σ, Max, RMS) of the absolute errors in the simulated coordinates of a knee model compared between before and after correction				
Before correction	μ [mm]	σ [mm]	Max [mm]	RMS [mm]
First simulation: 26 x 24 x 8	2.7896	0.9978	5.8968	2.9627
Second simulation 31 x 29 x 11	2.7895	1.0001	5.8988	2.9633
Third simulation: 36 x 34 x 14	2.7890	1.0011	5.8985	2.9632
After correction	μ [mm]	σ [mm]	Max [mm]	RMS [mm]
First simulation: 26 x 24 x 8	0.0439	0.0257	0.1357	0.0509
Second simulation 31 x 29 x 11	0.0456	0.0273	0.1444	0.0531
Third simulation: 36 x 34 x 14	0.0466	0.0281	0.1492	0.0544

26 x 24 x 08
31 x 29 x 11
36 x 34 x 14

Outer grid points in xy-direction x
Inner grid points in xy-direction x
Nr. of points in z-direction

Table 5.7: evaluation of the correction at the corrdinates of the MRI derived knee model for the three different grid densities

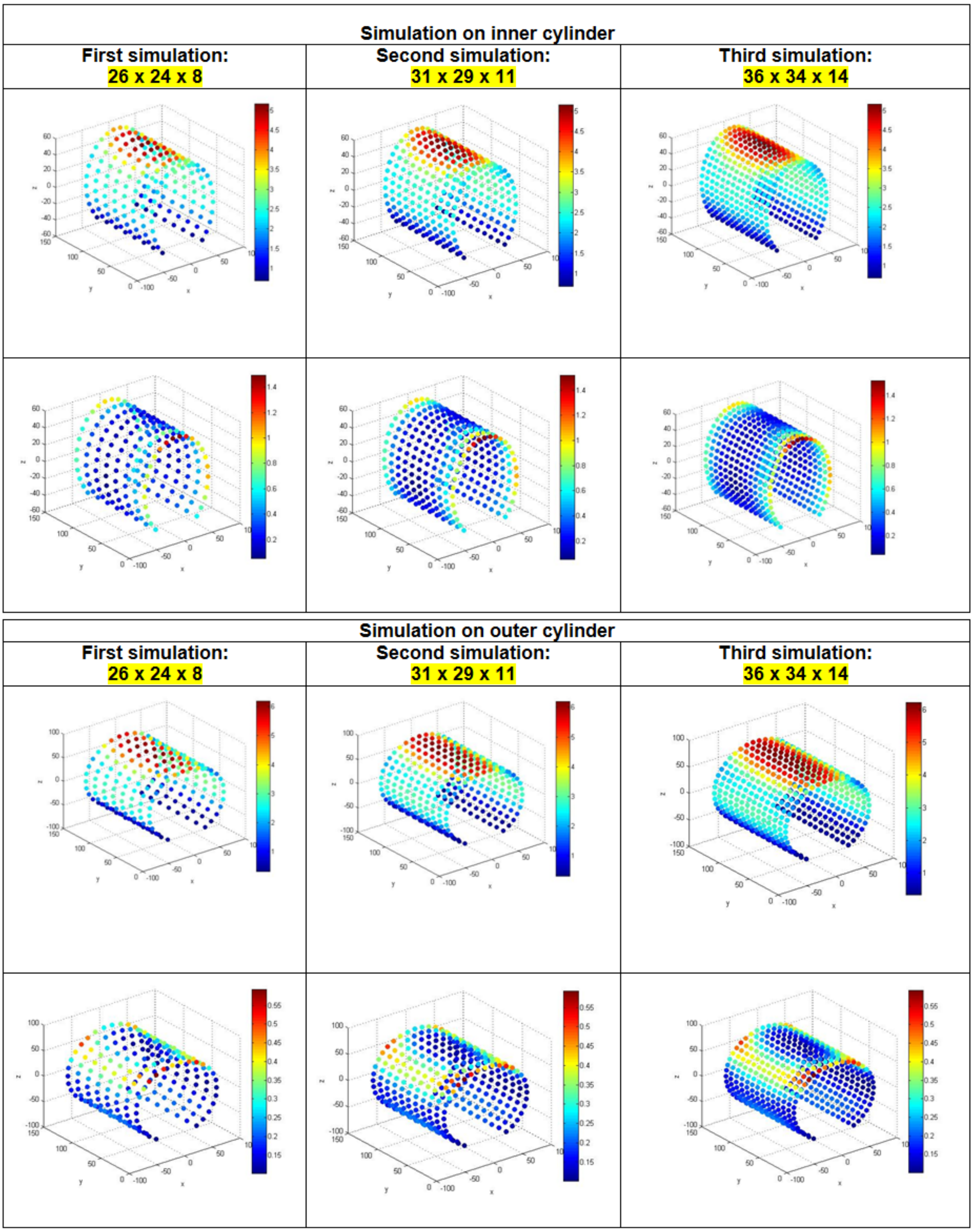

Figure 5.5: Simulation of the correction on the inner and outer grids for the three different grid densities

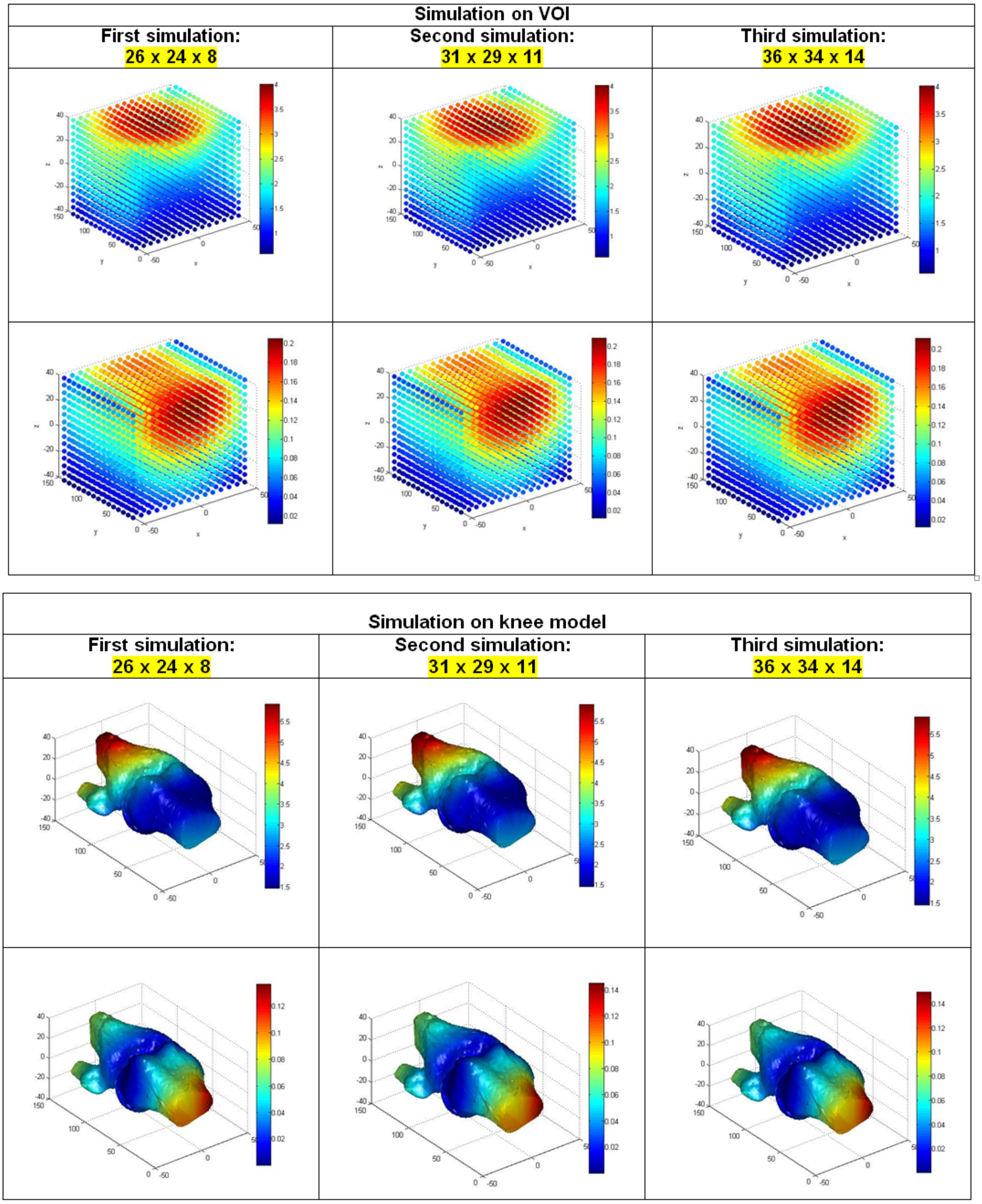

Figure 5.6: Simulation of the correction on the VOI and a virtual knee model for the three different grid densities

5.2.3 Phantom design ideas

During literature research on MR-related phantoms, many phantom designs have been developed for different quality control purposes. According to AAPM, material, accuracy issues, shape and grid features have to be fulfilled for the phantom design. Ideas from literature research, recommendations from AAPM and design restrictions which have to be considered while designing the phantom are essential factors for the final and optimal outcome. Several grid design ideas were proposed, see figure 5.7. Their advantages and disadvantages are listed in table 5.8 and 5.9. Image processing part has to be taken into account as a priority issue while thinking of a design of this phantom. Detection of the markers, especially for the center of the points depends on the shape of the markers. Some parameters were fixed, like marker shape and size, size of the phantom due to restriction of the space inside the knee coil and the size of the imaged object, which is in this case an artificial knee joint. The first idea shows cuboid-shaped phantom comprising two cuboid-shaped grids; the outer and the inner grid for calibration (correction) and evaluation respectively. The cuboid-shaped patterns grids allow more flexibility to integrate image information acquired from all standard orthogonal imaging planes: axial, coronal and sagittal. In addition, this would improve and simplify the definition of the grid patterns in further image processing works. Furthermore, the shape of the grids is easy to manufacture. Number of points that can be reached maximally within one grid is 280 control points. But on the other side, a cuboid-shaped grid around a rounded volume of interest doesn't reach the surface as good as a rounded shaped grid. The edges remain far away from the surface of the scanned object. Cuboid-shaped phantoms made out of different parts require careful and accurate fixation and assembly to ensure the total accuracy of the phantom. Because of those considerations, a rounded shape of a calibration phantom was the optimal solution for this case. The second version of the phantom design was a conic cylindrical phantom. It has the shape of cone in depth with small drillings along the entire depth of the phantom to simulate the effects of grids on MRI and CT images. The cylindrical shaped phantom offers an optimal coverage of VOI and excellent fitting inside the knee coil. This shape allows more rigidity and structural stability, where the bending effect is totally eliminated. Also, there is no need of fixation screws and pins. But there is no optimal solution because of the control points which lies on a curved grid, it is more complicated to detect and in this case only axial image slices can provide helpful information. Here, the conical shape provides a slope in z-direction; which could be used for the pattern detection and encoding along the z-direction.

Since there is not enough space inside the coil for making conical grid with higher slope, also risk of air accumulation or air bubbles inside the 150 mm long small cylinders, complication from manufacturing point of view and elimination of sagittal and coronal slices are the major disadvantages of this design. The third version solves those problems. It has also a cylindrical shaped grids; calibration and evaluation grids. They fit optimally inside the coil and cover the round-shaped VOI. The direction of the holes are similar to the first phantom design, it allows 253 control points for each grid. No risk for bending with the rounded shape and fixation screws and pins with the ground holding plate. However, the realization of this idea at our mechanical workshop has found out up to 2 mm error for in cylinder's diameter. That was due to the cutting of the grids. Therefore, a fourth version was delivered where cutting of the grids was carried off. The fourth version has the same criterions as the previous one. It does have fully cylindrical shape grids. This shape assures structural stability, rigidity, no need to fixate screws and since no many parts to assemble it is considered as an easy and simple design with 319 control points, i.e. maximum number of control points could be achieved. Risk of air bubbles accumulation, difficulties in manufacturing and the difficulty in image processing to integrate information from coronal and sagittal imaging directions remain limitations of the proposed design. The considered specific requirements, advantages and disadvantages for the phantom design are summarized in table 5.9.

Figure 5.7: Four different design ideas

Phantom design	Advantages	Disadvantages
Phantom with cuboid grids 	• Plate-grids have optimal shape for image processing • Cuboid girds are easier to manufacturer than cylindrical ones. • Grid allows many control points, total points = 280 • Phantom allows sagittal, coronal and axial slice selection	• The inner control points are not so close to the volume of interest! • Risk of bending while fixation of the grids • Risk of non-rigidity : many fixation screws and pins • Risk of air bubbles • Restricted thickness of the plates since geometry of the coil and the bone model
Conic shaped phantom with cylindrical drillings 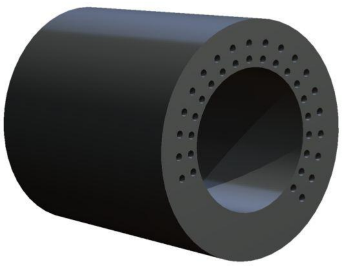	• Excellent fitting inside the knee coil • Optimally Coverage of volume of interest • Optimal for detection of axial slices • Conic shape of the outer cylinder allows the localization and encoding along the z-direction • Rigid body, structural stability and bending risk of the body is eliminated • No need for fixation screws and pins, since the grid consists of only one rigid part	• Control points which lies on a curved grid could be more complicated to detect than those who lies on plain grid • Not enough space inside the coil for making the conical/cylindrical grid with higher slope, which is needed as an essential information for detection in z-axis • Risk of air accumulation in the small long drillings • More complicated to manufacture • Suboptimal integration of information from coronal and sagittal imaging planes

Table 5.8: Advantages and disadvantages of cuboid and conic/cylindrical phantom designs

Half cylindrical calibration and evaluation grids 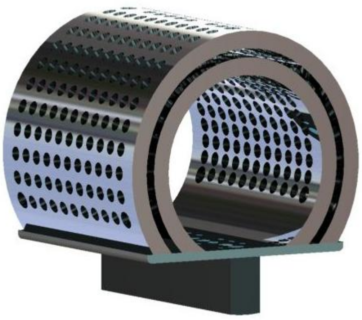	• Excellent fitting inside the knee coil • Optimally Coverage of volume of interest • Optimal for detection of axial slices • More secure and rigid fixation since not so many parts to assemble • Structural stability • No risk of grid bending • Simple design • Number of detection points on each grid: (23 x 11 = 253 pts)	• Control points which lies on a curved grid could be more complicated to detect than those who lies on a plane grid • More complicated to manufacture since holes lays on a curved body • Cutting of the grids results in up to 2 mm error for the cylinder's diameter • Possibility for air bubbles accumulation inside the holes • Suboptimal integration of information from coronal and sagittal imaging planes
Fully cylindrical calibration and evaluation grids 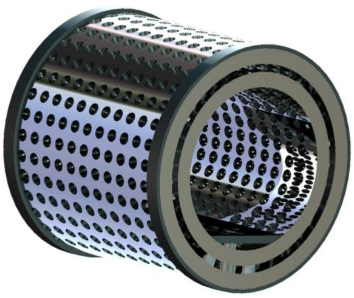	• Same criteria as for the last version of design • More secure and rigid fixation since not so many parts to assemble compare to the last version • Even more structural stability since no cutting of the grids • No risk of grid bending • More number of detection points for each grid: (29 x 11 = 319 pts)	• Control points which lies on a curved grid could be more complicated to detect than those who lies on a plain grid • More complicated to manufacture • Possibility for air bubbles accumulation inside the holes • Suboptimal integration of information from coronal and sagittal imaging planes

Table 5.9: Advantages and disadvantages of half and fully cylindrical phantom designs

5.3 Construction

The fourth phantom design version seen in figure 5.7, meets study's purposes, requirements and it was therefore chosen among the other ideas for the manufacturing., therefore it was chosen to be the manufactured one. See figure 5.8. The chosen material is Polyvinyl chloride plastic (PVC); is less expensive than plexiglas and allows good detection in both MRI and CT modalities.

The phantom has two fully cylindrical shaped grids; calibration and evaluation grids. This shape assures structural stability, rigidity, no need to fixate screws and since no many parts to assemble it is considered as an easy and simple design with many control points. Previous mentioned limitations of this design, are risk of air bubbles accumulation, complex of manufacturing and again elimination of coronal and sagittal slices. the required manufacturing accuracy from our mechanical workshop was 0.01 mm. CAD-drawings of phantom parts are listed in Appendix A.1, A.2, A.3, A.4, A.5, and A.6. During this section, a detailed explanation of each part's geometry and functionality will be demonstrated.

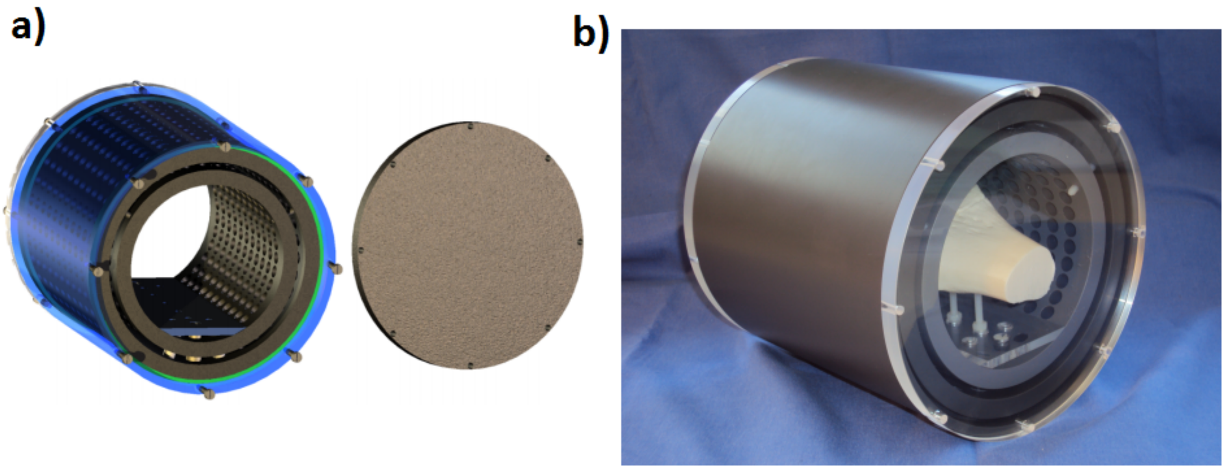

Figure 5.8: Phantom Setup: a) 3D-CAD drawing. b) Photograph of the manufactured phantom

5.3.1 Evaluation grid

The inner grid which surrounds and stands close to the artificial knee joint is the evaluation grid. It consists of 319 detection points in shape of holes. Each cylindrical hole is 8 mm in diameter and 10 mm in depth. The chosen material for this grid is PVC. Each row of the grid contains 29 points with distance between two holes in size of 12 mm, where each hole lies 10 degrees from the center of the grid. See figure 5.9.

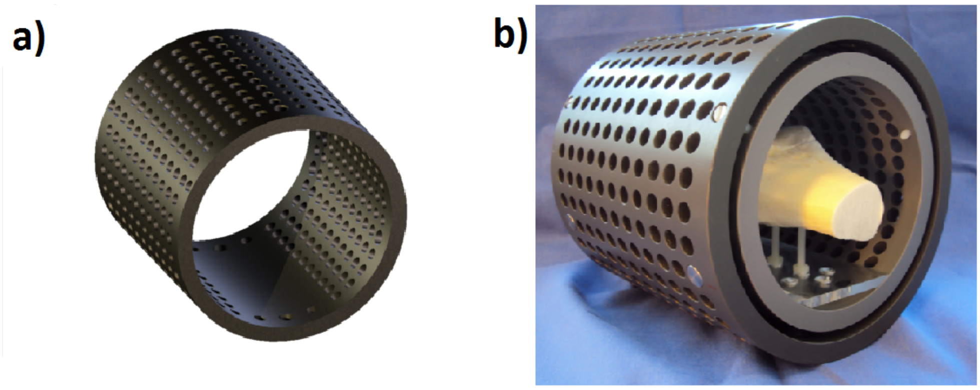

Figure 5.9: Calibration grid: a) 3D-CAD drawing. b) Photograph of manufactured calibration grid

5.3.2 Calibration grid

The outer grid which surrounds the evaluation grid and spaced 10 mm from it, is called calibration grid. It consists also of 319 detection points in shape of holes. Each cylindrical hole is 8 mm in diameter and 10 mm in depth. Six holes have 10 mm in diameter, and are spread around the edges of the grid. The functionality of these six bigger holes is to receive CT-markers used as a 3D rigid body for the various registration steps as CT-phantom, MRI-Phantom and CT-MRI. The holes on the outer grid are considered for the registration between CT-Phantom/ MRI-Phantom and CT-MRI which will explain later in evaluation concept. As mentioned before, CT-modality is considered as a ground truth, and is used here to compare MR-scans with the help of the registration markers. The chosen material for this grid was also PVC. Each row of the grid contains also 29 points with distance between two holes in the size of 12 mm, where each hole lies 10 degrees from the center of the grid. See figure 5.10.

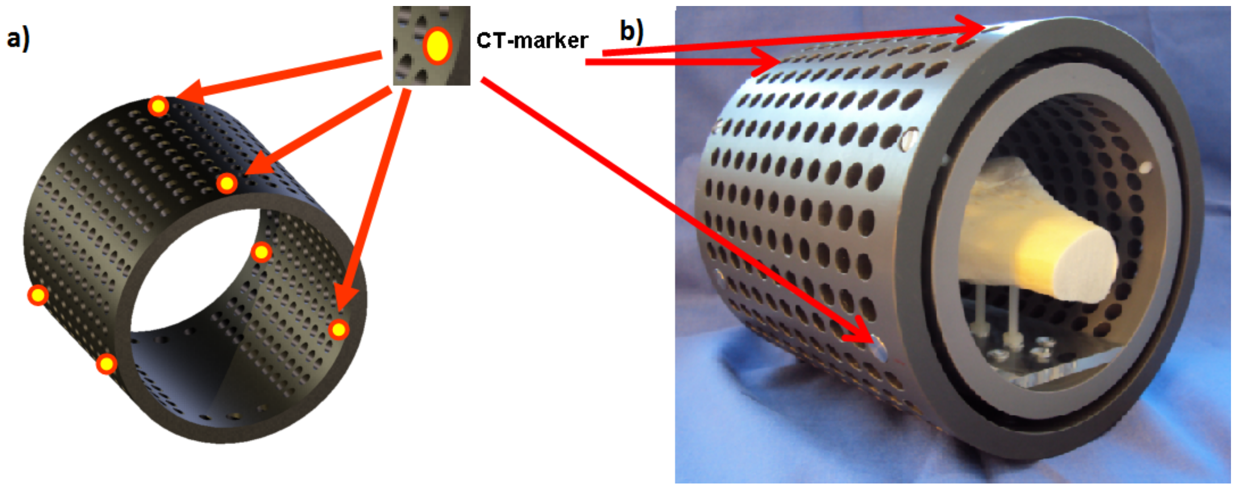

Figure 5.10: Evaluation grid: a) 3D-CAD drawing. b) Photograph of manufactured evaluation grid

5.3.3 Cylinder body

The grids are placed inside a bigger tube, which is called cylinder body. It is a simple cylinder which functions as a holder for the whole phantom construction, together with Copper Sulphate and Natrium Chloride solution as a contrast agent. It is rigid and sealed with two covers on the side, together with silicone to prevent solution leakage. The proposed dimension of the tube is considered to fit inside the geometry of the coil, which has 180 mm in diameter and 230 mm long. The signal active area of the coil lies in size of 160 mm. The chosen material for cylinder body is also PVC.

5.3.4 Fixation plate and knee model

Fixation plate is needed to settle the knee model with fixation pins and glue. Later on it will be fitted on the inner grid. See figure 5.11.

a) b)

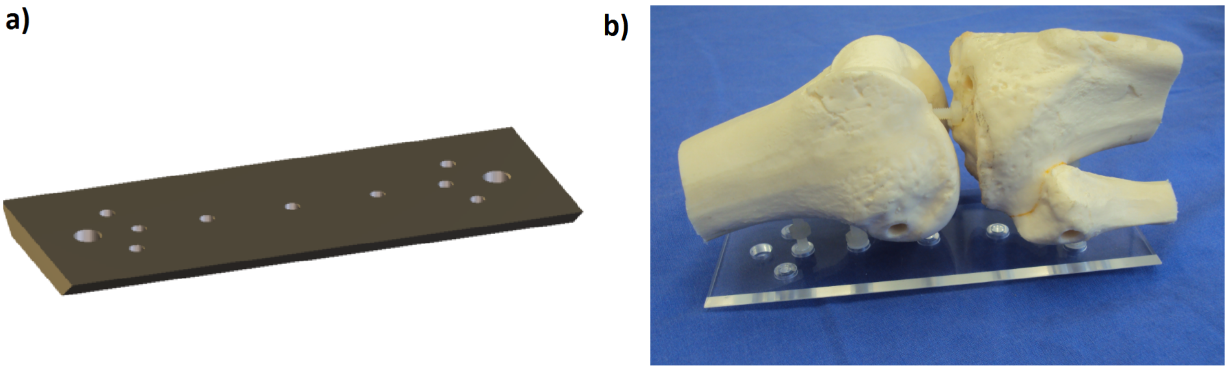

Figure 5.11: Fixation plate: a) CAD-drawing of fixation plate. b) Photograph of fixation plate with knee model

5.4 Experiment setup

The needed tools for this case study is a Philips Quadrature lower extremity coil, see photograph b) in figure 5.13, the new developed phantom prototype, see photograph a) in figure 5.13, an artificial knee joint, 0.7 g/l $CuSo_4$ and 2.68 g/l $NaCl$ solution. See experiment setup in figure 5.12. The newly developed phantom prototype was constructed and assembled, as shown in figure 5.13, photograph a). The phantom was filled very carefully with signal producing material $CuSo_4$ and $NaCl$ solution. To avoid air bubble accumulation inside the holes, the phantom was completely filled with the solution and resting over night before scanning. Later on, MR and CT-scans were taken with optimal scanning sequences.

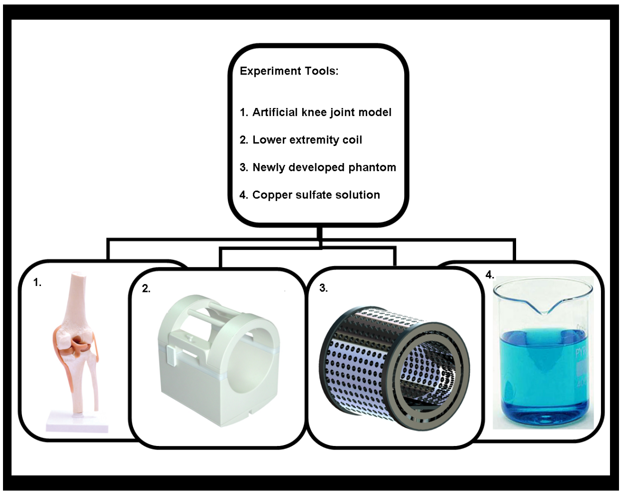

Figure 5.12: Experimental tools

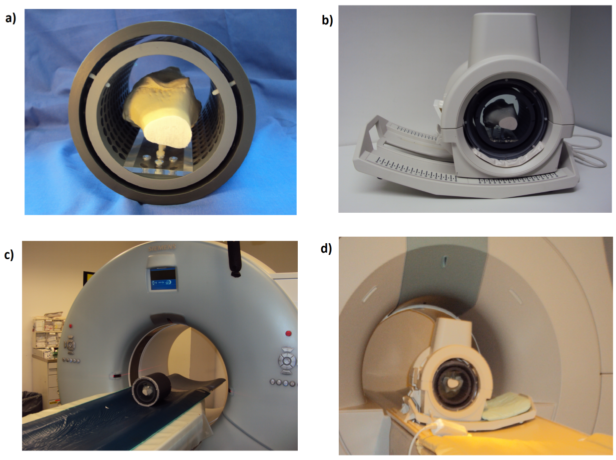

Figure 5.13: Phantom undergoing CT and MR scan: a) Phantom setup. b) Phantom within knee coil. c) CT scanning. d) MR scanning

5.4.1 Image acquisition

Image acquisition for both CT and MR modalities were achieved in the facilities of department of diagnostic and interventional radiology at the university hospital in Aachen (Universitätsklinikum-Aachen). The MR images were acquired with Philips Medical Systems, 1.5T MRI scanner. Positioning of the phantom was as near as possible to the magnet isocenter, and scanning was done with Philips knee coil. Imaging acquisition was performed according to the parameters listed in table 5.10 for MRI, and in table 5.11 for CT. T2 weighted Turbo Spin Echo (T2W TSE) imaging sequence was the optimal sequence for this case.

Parameter	Philips Medical Systems Intera 1.5T Settings
Image mode	Two – dimensional
Protocol name	T2W_TSE
Repetition time – TR	1000 ms
Echo time – TE	100 ms
Flip angle	90 degrees
Matrix size	192 x 192
No. of slices	192
Slice thickness	1 mm
Slice gap	1 mm
Receiving coil	Knee coil
Field of View	192 x192 mm^2

Table 5.10: Acquisition parameters for Magnetic Resonance Imaging

Parameter	Siemens Somatom Settings
Voltage	120 kV
Current	198 mA
Matrix size	512 x 512
No. of slices	185
Slice thickness	1 mm
Slice gap	1 mm
Field of View	187 x187 mm^2

Table 5.11: Acqusition parameters for Computed Tomographic Imaging

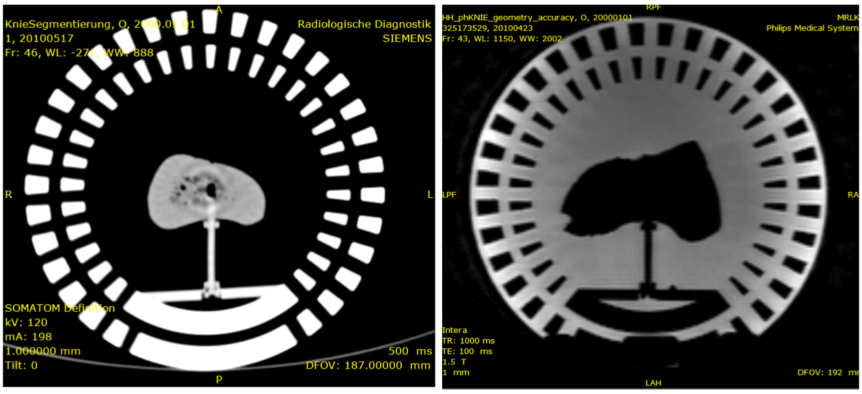

CT scan MR scan

Figure 5.14: Image acquisition; CT and MR scans of the phantom

5.5 Detection of registration markers

In this study, detection of 33 holes or markers on the surface of the outer grid on both CT and MRI was performed. The detected markers are well distributed around the knee model, and are used as registration markers. The detection of markers edges in both CT and MRI images was carried out by a dedicated image processing method and while the estimation of the marker center was performed by fitting a cylindrical surface to the detected edges points. For this purpose cylinder fitting concept, its evaluation and the related image processing steps for edge detection will be presented.

5.5.1 Cylinder fitting

In this method it is used Matlab-based Least Squares Geometric Elements package developed by the National Physical Laboratory (NPL) at the UK National Measurement Laboratory, [Smith, 2002]. It is a robust, well established algorithm which can be used in a segmentation strategy. The cylinder fitting procedure fits a cylinder surface to the extracted edges from each slice and approximates its center and radius. Figure 5.15 (a), (b) and (c), presents the simulation results of a fitted cylinder without noise.

5.5.2 Evaluation of the performance of cylinder fitting

To evaluate the performance and robustness of the LSGE two Matlab simulations were performed. In the first simulation the performance of the cylinder fitting method were tested for non-noisy simulated holes for seven different orientations ($0, 45, 135, 180, 225, 270$ and 315 degrees). Statistical evaluation for deviation between the estimated holes centers and the real centers (calculated using the regionprops Matlab-method on the central slice) were carried out.

The second simulation were performed on simulated noisy holes for different amounts of noise: 5, 10, 15 and 20 % of the hole diameter, see figure 5.16. The noise amount has been added 1000 times for each case and statistical evaluation were then performed. For the first statistical evaluation the root mean square deviation (RMS) was calculated while the mean, the standard deviation, the maximum and the root mean square deviation were all calculated. The results are represented in table 5.12 and table 5.13.

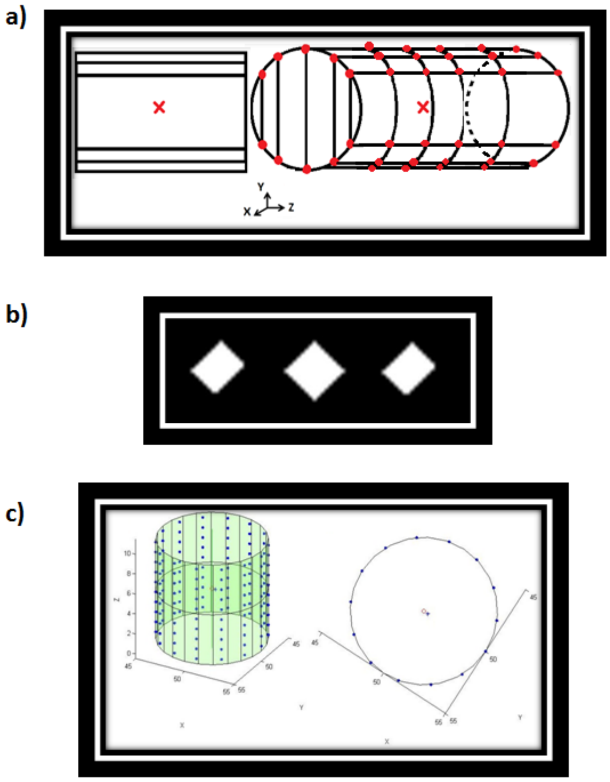

Figure 5.15: Concept of cylinder fitting: a) drawing of the concept; b) simulated slices; c) simulated fitted cylinder

Angle [°]	Difference (Euclidean distance) [mm]	RMS [mm]
0	0	0.025
45	0,035	
135	0	
180	0,035	
225	0	
270	0,035	
315	0	

Table 5.12: Evaluation of the performance of cylinder fitting without noise. Simulated hole: d=10, l=10 [mm]

Noise amplitude = % of simulated hole diameter [%]	RMS [mm]	μ [mm]	σ [mm]
5	0.335	0.334	0.025
10	0.342	0.339	0.047
15	0.354	0.346	0.074
20	0.374	0.363	0.093

Table 5.13: Evaluation of the performance of cylinder fitting with random noise

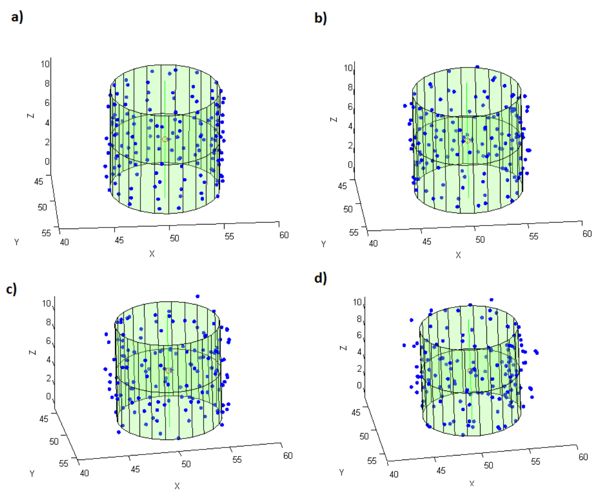

Figure 5.16: Evaluation of the cylinder fitting with random noise
Evaluation of the cylinder fitting with random noise: a) 5% noise. b) 10% noise. c)15% noise and d) 20% noise

5.5.3 Image processing

The flowchart in figure 5.17 shows the used concept for detection the holes centers from CT and MRI image data.

Based on the proir knowledge on the phantom geometry, a semi-automatic method has been developed for the definition of region of interests (ROIs) for all phantom markers. Figure 5.18 shows the defined ROIs around the registration markers for both CT and MRI data.

Based on image analysis inside these ROIs 3D-image segments including the markers were obtained semi-automatically by the definition of cylinders start-and end-slices. Figure 5.19 and 5.20 show the defined image segments for the first registration hole from both CT and MRI data. To obtain the region of the cylinder on each slice, application of a simple subtraction technique was performed. In this step the start-slice was considered as background and compared to all subsequent slices included in the image segment.

A thresholding technique based on extended maximum transformation was then applied to each individual slice to get binary images of the hole. The boundary of the hole was finally carried out by finding the edge map of the resulting binary image slices. Figure 5.21 and 5.22 show the result of the subtraction and thresholding techniques together with the final detected hole edges for CT and MRI data respectively.

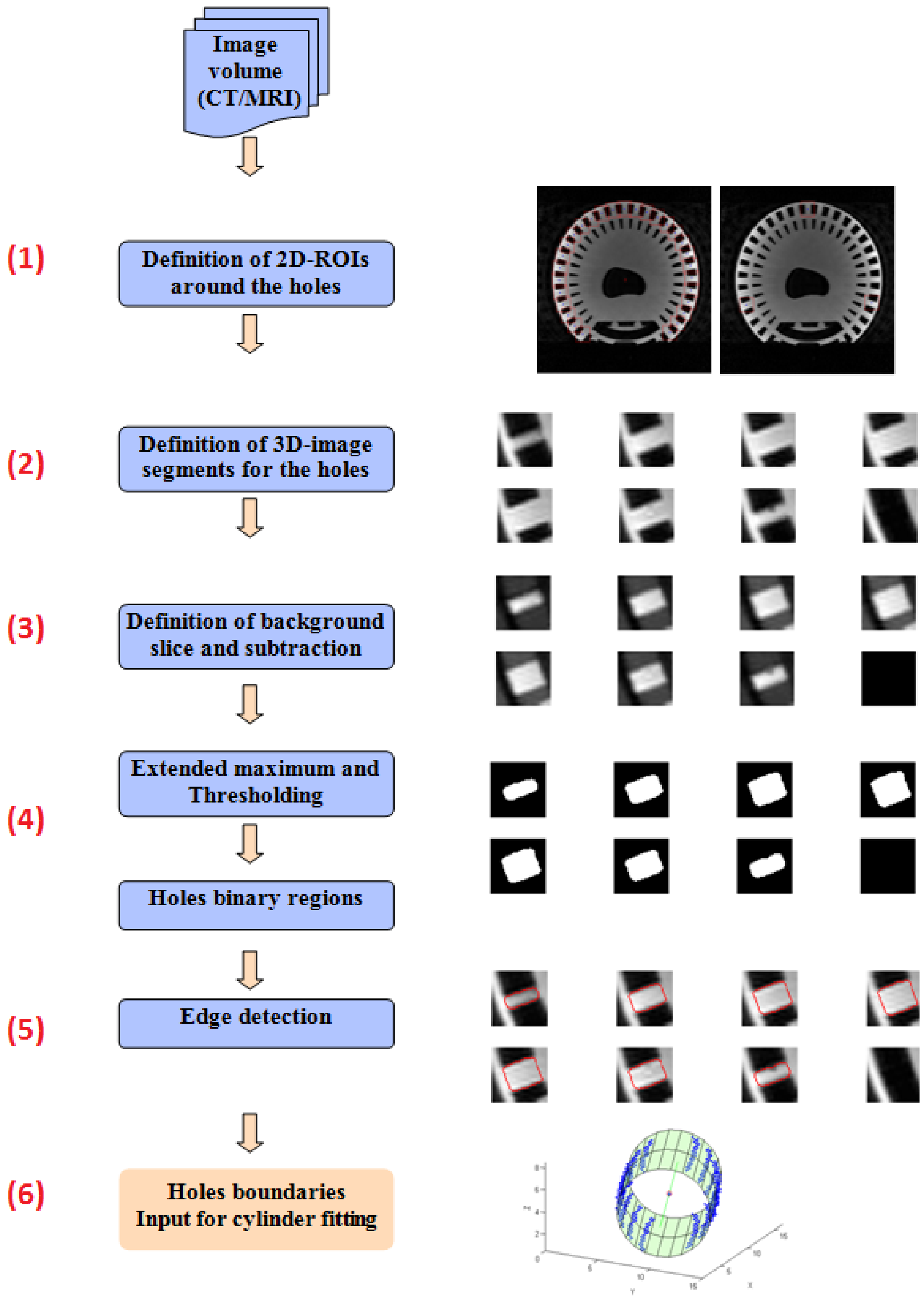

Figure 5.17: Concept of detection of hole centers

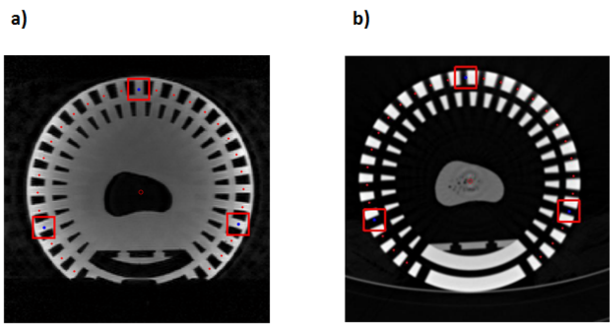

Figure 5.18: Definition of the ROIs around the markers used for the rigid registration between CT (b) and MRI (a)

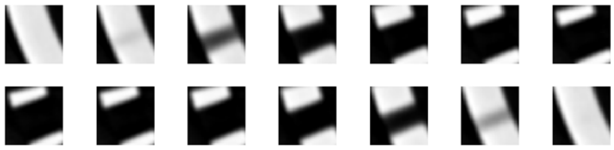

Figure 5.19: Obtained 3D image segment (CT); including the first registration hole from the CT data showing the start-slice (upper left) and end-slice (lower right)

Figure 5.20: Obtained 3D image segment (MRI); including the first registration hole from the MRI data showing the start-slice (upper left) and end-slice (lower right)

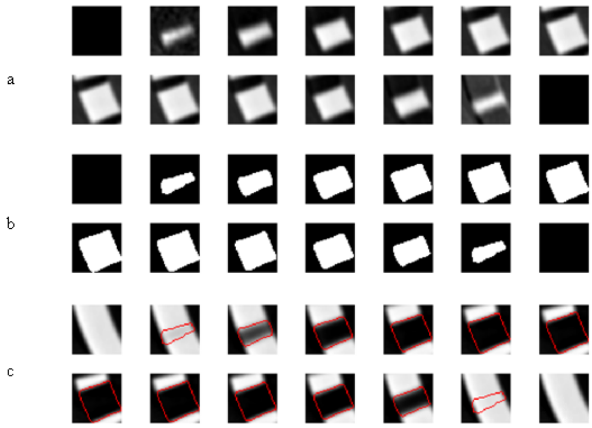

Figure 5.21: (a) Results of the subtraction (b) thresholding (c) techniques together with the final hole boundary superimposed on the original CT image

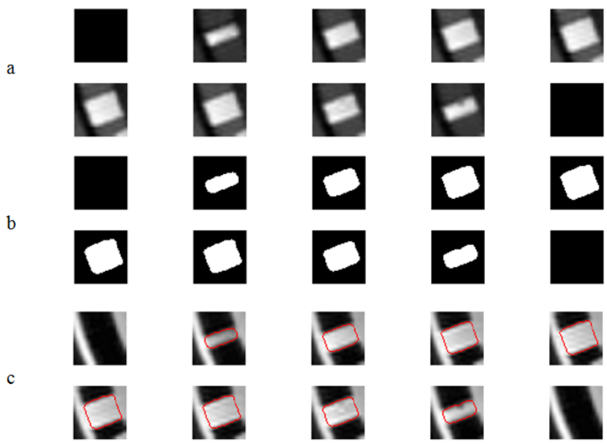

Figure 5.22: (a) Results of the subtraction (b) thresholding (c) techniques together with the final hole boundary superimposed on the original MRI image

5.6 Evaluation methods

To evaluate the amount of distortion associated with the MRI in this phantom study, the surface of the scanned bone model together with the locations of a set of phantom markers were extracted from the corresponding CT and MRI image data, figure 5.23. The marker set extracted from the outer grid (the calibration grid) were used as a reference body for comparison between the CT- and MRI-derived bone models. In the framework of this Master thesis two concepts for distortion evaluation were adopted. The first evaluation concept is illustrated in figure 5.24. The first part of this evaluation illustrates a comparison of the CT-extracted markers to their reference locations from the phantom geometry. The comparison was performed at the positions of 33 markers located on the outer grid. This evaluation would provide information about the accuracy of our marker detection method (Image Processing and cylinder fitting) since CT is recognized to be distortion-free imaging modality. The same evaluation was performed in the second part but using the MRI-extracted markers. For the two parts the comparisons were carried out by finding the optimal rigid registration between the extracted markers and their reference locations. Figure 5.25 illustrates the second evaluation concept, where in its first part the MR-extracted markers are compared to the CT-extracted markers considered as reference. The optimal rigid registration between the two marker sets were also calculated and for two different sizes of the markers set (6 and 33 markers), see figure 6.1. The purpose of this was to investigate the effect of the marker set's size on the registration outcomes. The second part of this evaluation involves a 3D surface comparison between the MRI- and the CT-derived models using the optimal rigid registration calculated in the first part.

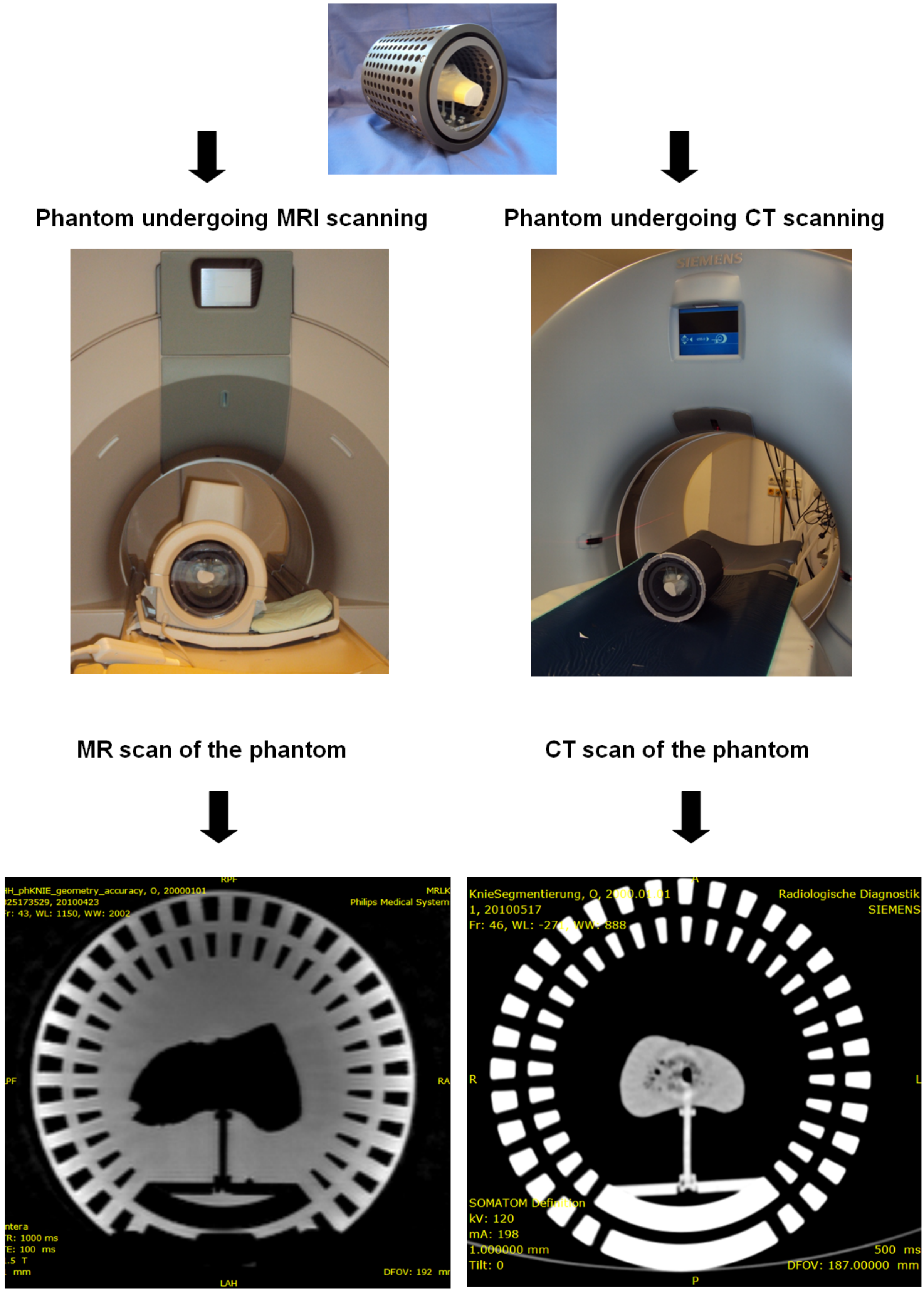

Figure 5.23: MRI-acquisition (left) and CT-acquisition of the constructed calibration phantom

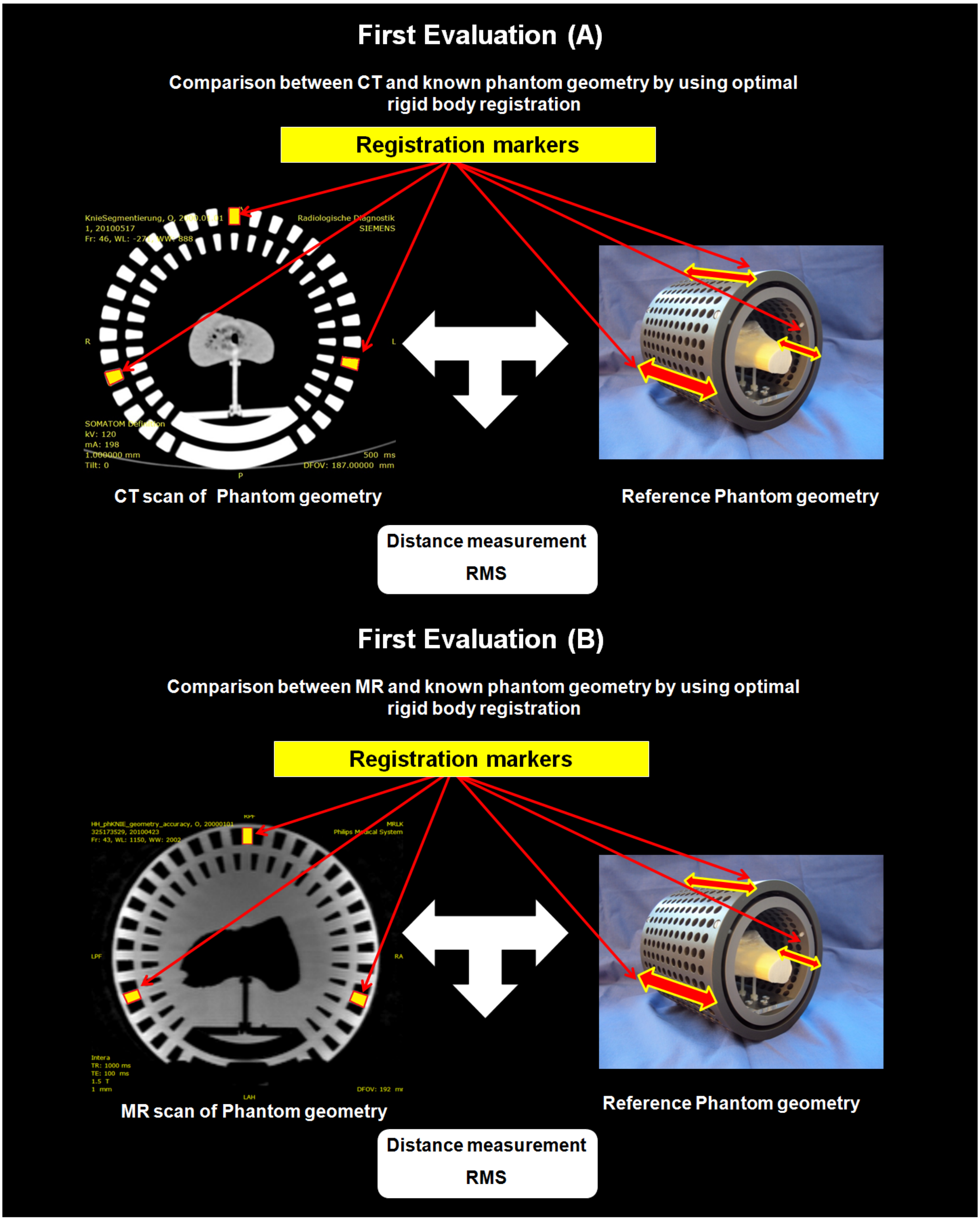

Figure 5.24: A) Comparison of CT with phantom geometry. B) Comparison of MRI with phantom geometry

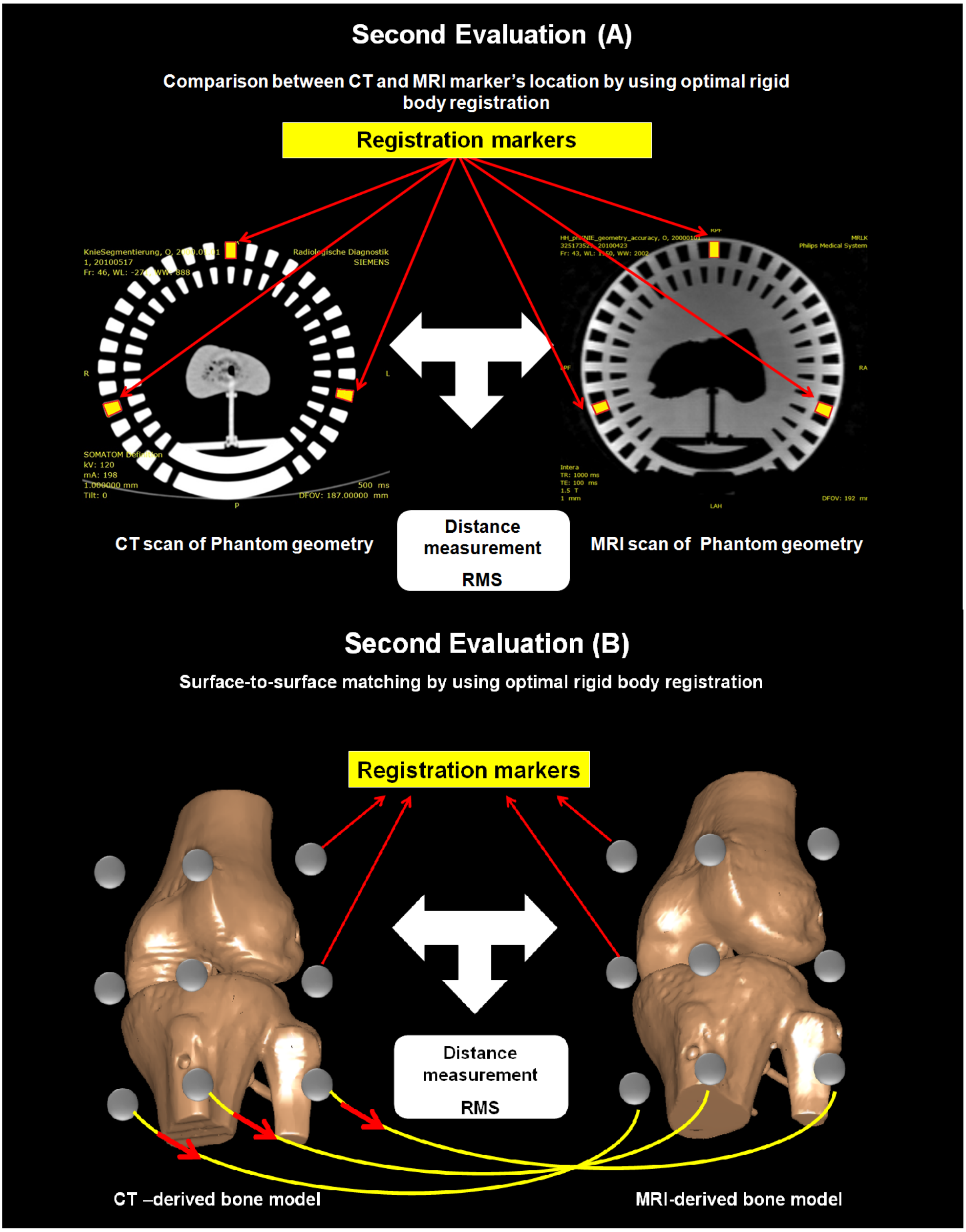

Figure 5.25: A) Comparison of CT with MRI. B) Comparison between CT and MRI bone surfaces

6 Results

In this chapter, results of previous mentioned evaluation concepts are presented. Results include; marker-based comparison between CT and MRI, comparison between CT and MRI at surface vertices, further comparison between CT and real phantom geometry and final comparison between MRI and real phantom geometry. Above mentioned comparisons were performed at defined marker positions by using an optimal rigid body registration method. Statistical results are presented in form of tables and figures.

6.1 Marker-based comparison between CT and MRI

As mentioned before, the comparison between CT and MRI images was performed at two different amount of registration markers; that is for the purpose of registration analysis. First registration between CT and MRI images included 6 markers and the second registration included 33 registration markers. In both cases, registration markers were distributed on the outer grid around the bone model. Table 6.1 represents a summary of statistical data (μ, σ, Max, RMS) of the absolute errors at the markers locations of above mentioned registration. The maximum distance error between CT and MRI by using 6 markers was 1.0252 mm, while for 33 markers was 0.96931 mm. Marker-based registration by using 33 registration markers showed less matching deviation than the registration with 6 markers. By increasing number of registration markers, the registration procedure became more accurate.

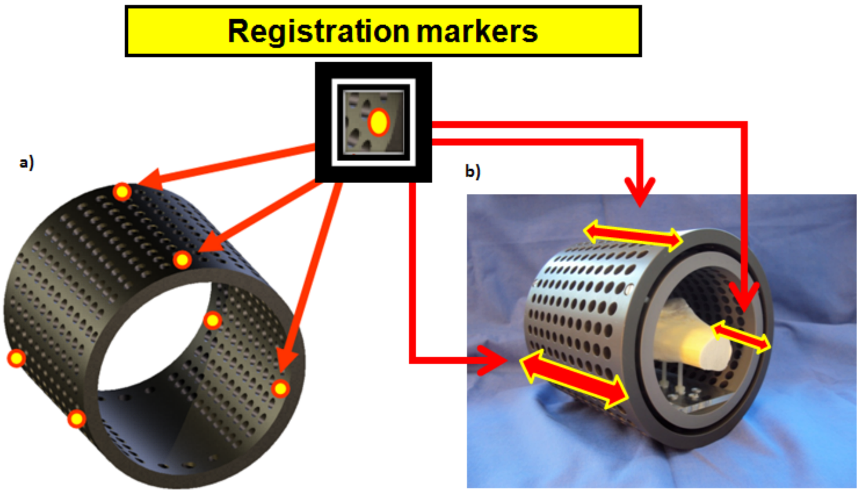

Figure 6.1: Marker-based registration at a) 6 markers; b) 33 markers

	μ [mm]	σ [mm]	Max [mm]	RMS [mm]
6 markers set	0.4656	0.3231	1.0252	0.5512
33 markers set	0.41605	0.18479	0.96931	0.4541

Table 6.1: Marker-based measurements of matching deviation between CT and MRI

6.2 Surface comparison between CT and MRI

Results from the evaluation at the surface vertices between CT and MRI models using 33 registration markers are summerized in table 6.2. After matching CT and MRI-derived models, as seen in figure 6.2 a), deviation errors at surface vertices were obtained by calculation of the distance between the two 3D models, see figure 6.2 b). The distribution of the deviation between the two models is shown on figure 6.3.

	μ [mm]	σ [mm]	Max [mm]	RMS [mm]
33 markers set	1.1262	0.5621	4.7115	1.2578

Table 6.2: Evaluation results of the deviation between the two models

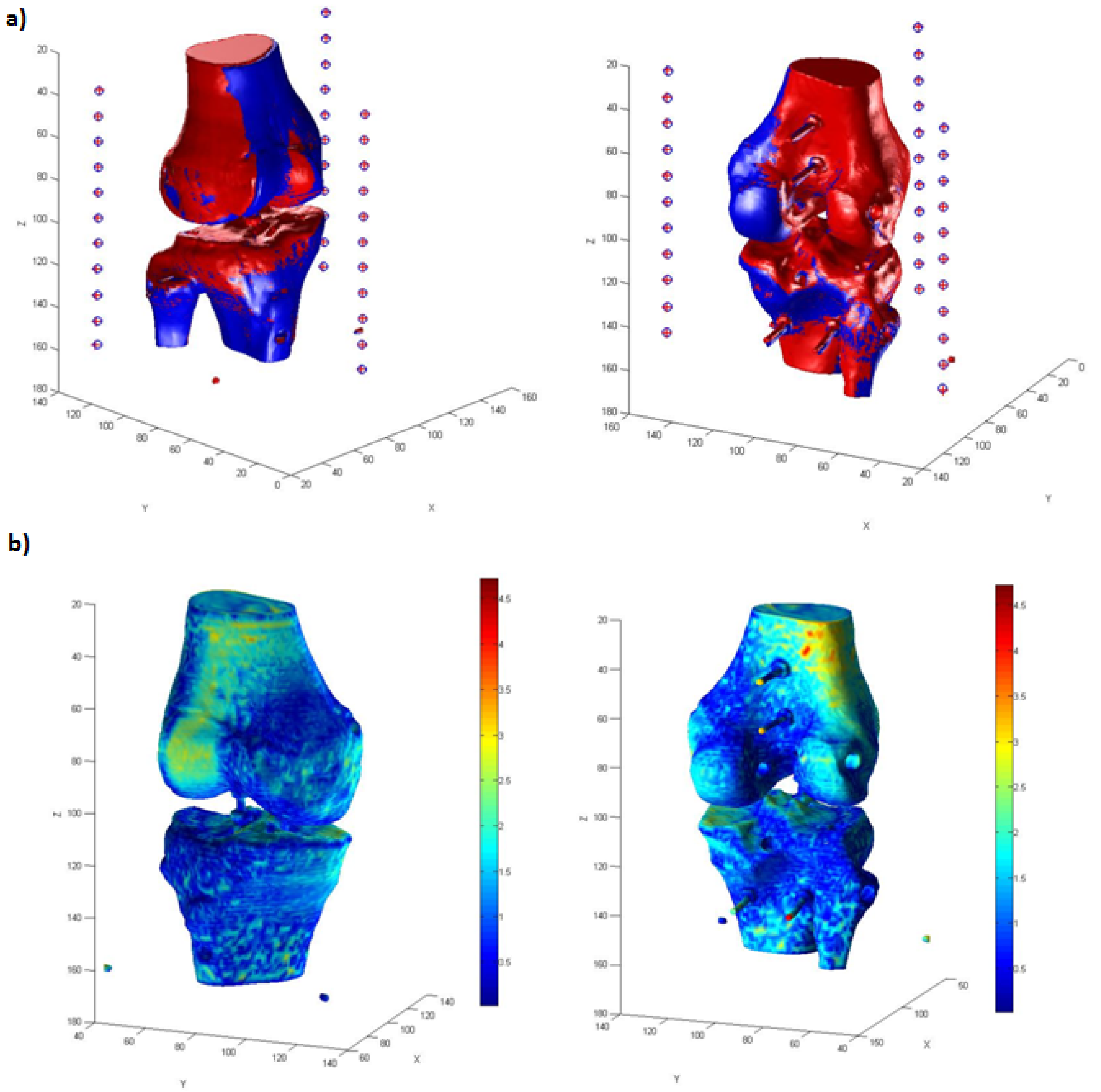

Figure 6.2: Measurement of geometrical difference between CT-derived and MRI derived model; a) Matching CT-derived (blue) with MRI-derived model (red) using 33 markers positions, b) Matching deviations at surface vertices

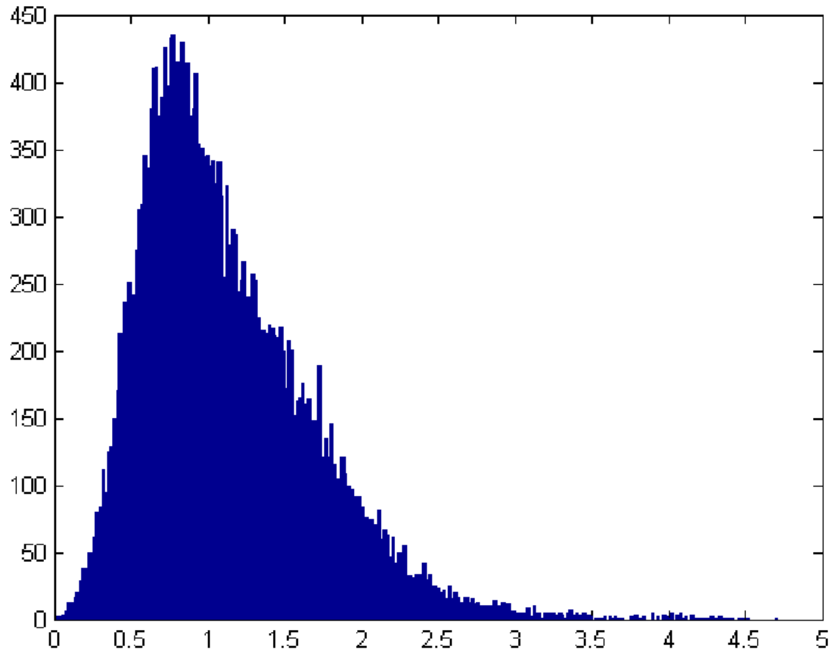

Figure 6.3: Distribution of the amount of deviatoin between the CT and MRI-derived model

6.3 Marker-based comparison between CT and phantom geometry

Another valuable evaluation was performed between CT phantom images and phantom real dimensions. Considering CT as a gold standard modality for the ability of providing precise geometric measurement, no deviation errors was expected between real phantom and measured phantom geometry. Table 6.3 presents the results from measurement of the geometrical differences between CT and real phantom geometry at 33 markers, by using rigid body registration. The measured deviations comprise manufacturing error, and the error of marker detection method (image processing and cylinder fitting).

	μ [mm]	σ [mm]	Max [mm]	RMS [mm]
33 markers set	0.26411	0.16477	0.6063	0.3099

Table 6.3: Marker-based measurements of matching deviation between CT and phantom geometry

6.4 Marker-based comparison between MRI and phantom geometry

Here, the differences in the coordinates at the locations of the 33 markers between those measured from the phantom images and that measured from the known dimensions of the phantom were examined after applying rigid body registration. The results for this comparison are summarized in table 6.4. Marker-based measurement between CT and phantom geometry showed less matching deviation than measurement between MRI and phantom geometry. These results were expected due MR-modality limitations.

	μ [mm]	σ [mm]	Max [mm]	RMS [mm]
33 markers set	0.3234	0.2012	0.9526	0.3793

Table 6.4: Marker-based measurements of matching deviation between MRI and phantom geometry

7 Discussion and Conclusion

7.1 Discussion and conclusion

The pre-operative planning of the total knee replacement (TKR) using the patient-specific templating (PST) technique has shown high potential in achieving precise bone resections and accurate alignment of the prosthesis components along with a reduced intervention time. Since the today's computer assisted planning and customization of individual templates uses CT-based 3D reconstructions of the bone structures and does not account for the volume of femoral and tibial cartilages. The intra-operative positioning of the planned templates requires, therefore, additional preparation work and operation time to remove the attached cartilages. The long term purpose is to use the MRI modality instead of the CT for the pre-operative planning since it provides excellent visualization of the knee cartilages and avoid the radiation risks of the the CT-imaging. However, as the quality of the planning is directly affected by the geometric accuracy of the 3D models it is mandatory as the first step to analyze and, if necessary, compensate the geometric distortions associated with MR images. In the framework of this thesis the work has focused on two main purposes; first the evaluation of the amount of distortion associated with the knee-MRI images; and second the primary investigations of the effectiveness of a proposed correction method for compensating of the distortion. The actual methods for the distortion evaluation and compensation are normally based on phantoms which scanned prior to the subject during the regular calibration procedures and combined with software-based built-in correction systems normally provided by the scanner's manufacturer. These methods accounts only for distortions due to gradients non-linearities and field inhomogeneities. Furthermore, these systems do not consider the object-specific distortions which vary according to the individual magnetic properties. For our first purpose we developed a dedicated calibration phantom which could be scanned together with the patient knee in the clinical scans and allows the quantification and correction of the overall amount of distortion as resultant of device-specific, scan-specific and object-specific distortions. In this study, different design ideas were proposed and analyzed regarding general and specific requirements. The considered criteria were functionality, MRI-compatibility, knee coil compatibility, manufacturing accuracy, material availability and costs, the image processing complexity involved with the detection of the phantom-specific markers. Based on the requirements analysis a dedicated phantom containing two cylindrical-shaped markers grids (319 markers in each grid) was the optimal design for our purposes and has been then realized. For the purpose of distortion evaluation the developed phantom was scanned in CT and MRI. We developed a method to extract the centers of a set of phantom markers from the corresponding CT and MRI images based on specific subtraction technique and cylinder fitting algorithm. The markers set extracted from the outer grid (the calibration grid) were used as a reference rigid body for comparison between the CT- and MRI-derived bone models. In the actual study only 33 markers were used in the reference rigid body. The comparison of the CT-extracted markers to their reference locations from the phantom geometry has shown a maximal deviation of 0.61 mm (mean: 0.26 mm, std: 0.16 mm, RMS: 0.31 mm), table 6.3. These results provide an evaluation of our markers detection method since CT is recognized to be distortion-free imaging modality. After manufacturing steps some markers could be visually identified as oval-shaped holes. This manufacturing inaccuracy may also have an effect on these results. The maximal deviation for the MRI-extracted markers compared to the reference geometry was, however, 0.95 mm (mean: 0.32 mm, std: 0.20 mm, RMS: 0.38 mm), table 6.4. These values were larger than those found for the CT-extracted markers. This could be due to an additional error arises by the geometric distortions. In the comparison between CT-extracted and MRI-extracted markers, where CT was considered as the ground truth, the maximal deviation found was 1.26 mm (mean: 0.47 mm, std: 0.32 mm, RMS: 0.55 mm) for a markers set consists of 6 markers and 0.97 mm (mean: 0.42 mm, std: 0.18 mm, RMS: 0.45 mm) for a markers set consists of 33 markers, tabel 6.1. The deviation was reduced using a larger number of registration markers. The 3D surface comparison between the MRI- and the CT-derived models using the larger markers set has shown at small regions a deviation up to 4.71 mm (mean: 1.13 mm, std: 0.56 mm, RMS: 1.26 mm), table 6.2 and figure 6.2. All evaluatiuons in this work were based on coordinate comparison after finding the optimal rigid registration for each evaluation. We have to keep in mind that several error sources may contribute to the final observed deviation (mean: 1.13 mm, std: 0.56 mm). Errors can arise from the markers detection methods, the 3D surfaces extraction and the rigid registration calculation.

Concerning the compensation of the distortion we preferred, due to time limitation, to constrains our efforts in the framework of this thesis on initial investigations concerning the effectiveness of a correction method based on thin-plate splines. These investigations were performed using computer simulation, were a knee bone model was distorted with a synthetic distortion (parabola-like shape) with maximal value of 6 mm and compensated with the proposed method. The proposed method was able to reduce the amount of distortion and keep the maximum deviation under 0.12 mm, table 5.7 and figure 5.6. This simulated served also to find the optimal number of grid patterns could be planned on the grids surface and used for distortion compensation.

7.2 Future work

The limitations of this work, an outlook on potential research and improvement areas for the future works are discussed. The final evaluation results in this study were carried out using markers set containing only 33 markers from the outer grid. It would be, however, interesting to perform the evaluation taking all markers from both outer and inner grids into consideration for future investigations. This would have two main benefits. First, the most reliable rigid registration could be achieved by using the maximal number of markers around the volume of interest. Second, the evaluation of the deviation at all possible markers locations will help to find whether the distortion particularly varies along a specific direction. The shape, size and distribution of the registration markers along with the accuracy of their detection in CT and MRI were important aspects while designing the calibration phantom. For the purpose of first investigation we simply used cylindrical holes filled with contrast material for MRI while this was not needed to achieve sufficient visualization and recognition in CT. During this phantom study, cylindrical markers were favored over spherical markers only due to their manufacturing simplicity. However, the major advantage of spherical markers is the simple and flexible detection on all imaging planes (axial, coronal and sagittal). In view of using cylindrical markers, we used image information from only axial slices in this study. The detection of the markers could be enhanced by using information from additional imaging planes. Further considerations concerning the markers shape and the overall experimental setup should be taken into consideration in case of future cadaver studies as the immersion in contrast medium may not be possible in this case. From another point of view, standard imaging protocols (CT, MRI) and a relative simple thresholding method were needed for segmenting the knee model's components in both modalities. This was due to the excellent contrast obtained between the model and the surrounding medium (contrast material for MRI and air for CT). For future cadaver studies the optimization of scanning protocols and development of a dedicated segmentation method for reliable 3D modeling of the related knee tissues will be, however, necessary. The proposed correction method in this study is based on the well established thin plate splines. First investigations were performed using computer simulation of the phantom geometry (calibration and evaluation grids) and synthetic distortions with a predefined shapes and amounts. In this step the test object was a virtual bone model of the knee and the correction of the applied distortions was promising. However, different shapes and amplitudes of distortion could be expected in real MRI scans. Future work will focus on the evaluation of the proposed method for compensating of geometric distortions associated in clinical MRI scan taken in cadaver studies.

Bibliography

[e-MR 2010.01.26] Experimental MR portal. (2010.01.26). – URL http://www.imaios.com/en/e-Courses/e-MRI/

[Dataspectrumcorporation 2010.01.26] Medical imaging phantom design. (2010.01.26). – URL http://www.spect.com

[MR-tip 2010.01.26] MR technology information portal. (2010.01.26). – URL www.mr-tip.com

[Wikipedia 2010.02.23] Wikipedia: The free encyclopedia. (2010.02.23). – URL http://en.wikipedia.org/wiki/Thin_plate_spline

[elonen 2010.02.25] elonen: Thin Plate Spline Demo. (2010.02.25). – URL http://elonen.iki.fi/code/tpsdemo/

[www.wmt.com 2010.03.15] Advanced knee systems: Total Knee Replacement. (2010.03.15). – URL http://www.wmt.com/TotalKnee/Patients/replacement$_$animation.asp

[www.orthoinfo.aaos.org 2010.03.15] American Academy of Orthopaedic Surgeons: Total Knee Replacement. (2010.03.15). – URL http://orthoinfo.aaos.org/topic.cfm?topic=A00389

[supertech 2010.03.22] MRI Quality Assurance Phantoms. (2010.03.22). – URL http://www.supertechx-ray.com/a2500-r.htm

[www.kneepaininfo.com 2010.03.29] Joint pain and injury information. (2010.03.29). – URL http://www.kneepaininfo.com/kneeanatomy.html

[Sportmedicine 2010.03.29] The Center for Orthopaedics and Sports Medicine. (2010.03.29). – URL http://www.arthroscopy.com/sp05001.htm

[www.imaios.com 2010.03.29] The knee MR-Interactive Atlas of Cross-Sectional Human Anatomy. (2010.03.29). – URL http://www.imaios.com/en/e-Anatomy/Limbs/Knee-MR

[Bookstein 1989] BOOKSTEIN, F.L.: Principal warps: Thin-plate splines and the decomposition of deformations. In: *IEEE Transactions on pattern analysis and machine intelligence* 11 (1989), Nr. 6, S. 567–585

[Breeuwer et al.] BREEUWER, M. ; ZYLKA, W. ; WADLEY, J. ; FALK, A.: Paper CARS 1999, June 23-26, 1999, Paris, France.

[Breeuwer et al. 2002] BREEUWER, Marcel ; ZYLKA, Waldemar ; WADLEY, John ; FALK, Andreas: Detection and correction of geometric distortion in 3D CT/MR images. (2002), S. 11–23

[Brown et al. 2003] BROWN, G.A. ; FIROOZBAKHSH, K. ; DECOSTER, T.A. ; REYNA JR, J.R. ; MONEIM, M.: Rapid prototyping: the future of trauma surgery? In: *The Journal of Bone and Joint Surgery* 85 (2003), Nr. Supplement 4, S. 49

[Caramanos et al. 2009] CARAMANOS, Z. ; FONOV, V.S. ; FRANCIS, S.J. ; NARAYANAN, S. ; PIKE, G.B. ; COLLINS, D.L. ; ARNOLD, D.L.: Gradient distortions in MRI: Characterizing and correcting for their effects on SIENA-generated measures of brain volume change. In: *NeuroImage* (2009)

[Cerney et al. 2003] CERNEY, M.M. ; ADAMS, D.C. ; VANCE, J.M.: Image Warping of Three-Dimensional Body Scan Data. In: *Image* 1 (2003), S. 2231

[Doran et al. 2005] DORAN, S.J. ; CHARLES-EDWARDS, L. ; REINSBERG, S.A. ; LEACH, M.O.: A complete distortion correction for MR images: I. Gradient warp correction. In: *Physics in Medicine and Biology* 50 (2005), Nr. 7, S. 1343–1361

[Glasbey und Mardia 1998] GLASBEY, C.A. ; MARDIA, K.V.: A review of image-warping methods. In: *Journal of Applied Statistics* 25 (1998), Nr. 2, S. 155–172

[Goble und Justin 2004] GOBLE, E.M. ; JUSTIN, D.F.: Minimally invasive total knee replacement: principles and technique. In: *Orthopedic Clinics of North America* 35 (2004), Nr. 2, S. 235–245

[Gray und Felmlee 1987] GRAY, JE ; FELMLEE, JP: Section thickness and contiguity phantom for MR imaging. In: *Radiology* 164 (1987), Nr. 1, S. 193

[Haaker et al. 2005] HAAKER, R.G. ; STOCKHEIM, M. ; KAMP, M. ; PROFF, G. ; BREITENFELDER, J. ; OTTERSBACH, A.: Computer-assisted navigation increases precision of component placement in total knee arthroplasty. In: *Clinical orthopaedics and related research* 433 (2005), S. 152

[Hafez et al. 2006] HAFEZ, MA ; CHELULE, KL ; SEEDHOM, BB ; SHERMAN, KP: Computer-assisted total knee arthroplasty using patient-specific templating. In: *Clinical orthopaedics and related research* 444 (2006), S. 184

[Heiland 2008] HEILAND, S.: From A as in Aliasing to Z as in Zipper: Artifacts in MRI. In: *Clinical Neuroradiology* 18 (2008), Nr. 1, S. 25–36

[Hinterwimmer et al. 2008] HINTERWIMMER, S. ; GRAICHEN, H. ; VOGL, T.J. ; ABOLMAALI, N.: An MRI-based technique for assessment of lower extremity deformitiesreproducibility, accuracy, and clinical application. In: *European Radiology* 18 (2008), Nr. 7, S. 1497–1505

[Hornak] HORNAK, J.P.: The basics of MRI. In: *Disponvel em< http://www. cis. rit. edu/htbooks/mri>. Acesso em* 8

[Jovicich et al. 2006] JOVICICH, J. ; CZANNER, S. ; GREVE, D. ; HALEY, E. ; KOUWE, A. van der ; GOLLUB, R. ; KENNEDY, D. ; SCHMITT, F. ; BROWN, G. ; MACFALL, J. et al.: Reliability in multi-site structural MRI studies: effects of gradient non-linearity correction on phantom and human data. In: *Neuroimage* 30 (2006), Nr. 2, S. 436–443

[Kawanaka und Takagi 1986] KAWANAKA, A. ; TAKAGI, M.: Estimation of static magnetic field and gradient fields from NMR image. In: *J. Phys. E* 19 (1986), S. 871–875

[Lee et al. 2008] LEE, Y.S. ; SEON, J.K. ; SHIN, V.I. ; KIM, G.H. ; JEON, M.: Anatomical evaluation of CT-MRI combined femoral model. In: *BioMedical Engineering OnLine* 7 (2008), Nr. 1, S. 6

[Ludeke et al. 1985] LUDEKE, KM ; RÖSCHMANN, P. ; TISCHLER, R.: Susceptibility artefacts in NMR imaging. In: *Magnetic resonance imaging* 3 (1985), Nr. 4, S. 329

[Mahesh 2004] MAHESH, M.: AAPM/RSNA physics tutorial for residents. In: *Radiographics* 24 (2004), Nr. 6, S. 1747

[Maintz und Viergever 1998] MAINTZ, J.B.A. ; VIERGEVER, M.A.: A survey of medical image registration. In: *Medical image analysis* 2 (1998), Nr. 1, S. 1–36

[Mangin et al. 2001] MANGIN, J.F. ; POUPON, C. ; CLARK, C. ; LE BIHAN, D. ; BLOCH, I.: Eddy-Current Distorsion Correction and Robust Tensor Estimation for MR Diffusion Imaging. In: *Lecture Notes in Computer Science* (2001), S. 186–194

[Menuel et al. 2005] MENUEL, C. ; GARNERO, L. ; BARDINET, E. ; POUPON, F. ; PHALIPPOU, D. ; DORMONT, D.: Characterization and correction of distortions in stereotactic magnetic resonance imaging for bilateral subthalamic stimulation in Parkinson disease. In: *Journal of neurosurgery* 103 (2005), Nr. 2, S. 256–266

[Michiels et al. 1994] MICHIELS, J. ; BOSMANS, H. ; PELGRIMS, P. ; VANDERMEULEN, D. ; GYBELS, J. ; MARCHAL, G. ; SUETENS, P.: On the problem of geometric distortion in magnetic resonance images for stereotactic neurosurgery. In: *Magnetic resonance imaging* 12 (1994), Nr. 5, S. 749

[Moro-oka et al. 2007] MORO-OKA, T. ; HAMAI, S. ; MIURA, H. ; SHIMOTO, T. ; HIGAKI, H. ; FREGLY, B.J. ; IWAMOTO, Y. ; BANKS, S.A.: Can magnetic resonance imaging-derived bone models be used for accurate motion measurement with single-plane three-dimensional shape registration? In: *Journal of orthopaedic research* 25 (2007), Nr. 7, S. 867–872

[Orth et al. 1999] ORTH, R.C. et al.: Development of a unique phantom to assess the geometric accuracy of magnetic resonance imaging for stereotactic localization. In: *Neurosurgery* 45 (1999), Nr. 6, S. 1423

[Portheine et al. 2004] PORTHEINE, F. ; OHNSORGE, JAK ; SCHKOMMODAU, E. ; RADERMACHER, K.: CT-based planning and individual template navigation in TKA. In: *Navigation, Robotics in Total Joint, Spine, Surgery. Berlin, Germany: Springer* (2004), S. 336–342

[Price et al. 1990] PRICE, RR ; AXEL, L. ; MORGAN, T. ; NEWMAN, R. ; PERMAN, W. ; SCHNEIDERS, N. ; SELIKSON, M. ; WOOD, M. ; THOMAS, SR: Quality assurance methods and phantoms for magnetic resonance imaging: Report of AAPM nuclear magnetic resonance Task Group No. 1. In: *Medical physics* 17 (1990), Nr. 2, S. 287–295

[Radermacher et al. 1998] RADERMACHER, K. ; PORTHEINE, F. ; ANTON, M. ; ZIMOLONG, A. ; KASPERS, G. ; RAU, G. ; STAUDTE, H.W.: Computer assisted orthopaedic surgery with image based individual templates. In: *Clinical orthopaedics and related research* 354 (1998), S. 28

[Smith 2002] SMITH, I.: Matlab least squares geometric element software. In: *Centre for Mathematics and Scientific Computing, National Physical Laboratory. url: http://www. npl. co. uk* (2002)

[Sumanaweera et al. 1994a] SUMANAWEERA, T. ; GLOVER, G. ; SONG, S. ; ADLER, J. ; NAPEL, S.: Quantifying MRI geometric distortion in tissue. In: *Magnetic Resonance in Medicine* 31 (1994), S. 40–40

[Sumanaweera et al. 1994b] SUMANAWEERA, T.S. ; ADLER JR, J.R. ; NAPEL, S. ; GLOVER, G.H.: Characterization of spatial distortion in magnetic resonance imaging and its implications for stereotactic surgery. In: *Neurosurgery* 35 (1994), Nr. 4, S. 696

[Tomczak et al. 1997] TOMCZAK, RJ ; GUENTHER, KP ; RIEBER, A. ; MERGO, P. ; ROS, PR ; BRAMBS, HJ: MR imaging measurement of the femoral antetorsional angle as a new technique: comparison with CT in children and adults. In: *American Journal of Roentgenology* 168 (1997), Nr. 3, S. 791

[Vadim 2000] VADIM, Kuperman: *Magnetic resonance imaging: physical principles and applications*. Academic Pr, 2000

[Wang et al. 2004a] WANG, D. ; DODDRELL, D.M. ; COWIN, G.: A novel phantom and method for comprehensive 3-dimensional measurement and correction of geometric distortion in magnetic resonance imaging. In: *Magnetic resonance imaging* 22 (2004), Nr. 4, S. 529–542

[Wang et al. 2004b] WANG, D. ; STRUGNELL, W. ; COWIN, G. ; DODDRELL, D.M. ; SLAUGHTER, R.: Geometric distortion in clinical MRI systems Part I: evaluation using a 3D phantom. In: *Magnetic resonance imaging* 22 (2004), Nr. 9, S. 1211–1221

[Wang et al. 2000] WANG, H. ; ZHENG, B. ; GOOD, W. ; ZHUANG, T.G.: Thin-plate spline based automatic alignment of dynamic MR breastimages. In: *Engineering in Medicine and Biology Society, 2000. Proceedings of the 22nd Annual International Conference of the IEEE* Bd. 4, 2000

[Westbrook et al. 2005] WESTBROOK, C. ; KAUT-ROTH, C. ; TALBOT, J.: *MRI in Practice*. Wiley-Blackwell, 2005

[Whitbeck und Guo 2006] WHITBECK, M. ; GUO, H.: *Multiple landmark warping using thin-plate splines*. 2006

[White et al. 2008] WHITE, D. ; CHELULE, KL ; SEEDHOM, BB: Accuracy of MRI vs CT imaging with particular reference to patient specific templates for total knee replacement surgery. In: *The International Journal of Medical Robotics and Computer Assisted Surgery* 4 (2008), Nr. 3, S. 224–231

[Yan et al. 2006] YAN, C.X.B. ; DEMONTE, T.P. ; JOY, M.L.G.: Gradient Distortion Correction for Low Frequency Current Density Imaging. (2006), S. 260–263

[Young et al. 1987] YOUNG, IR ; KHENIA, S. ; THOMAS, DGT ; DAVIS, CH ; GADIAN, DG ; COX, IJ ; ROSS, BD ; BYDDER, GM: Clinical magnetic susceptibility mapping of the brain. In: *Journal of computer assisted tomography* 11 (1987), Nr. 1, S. 2

A Appendix

A.1 CAD-drawings

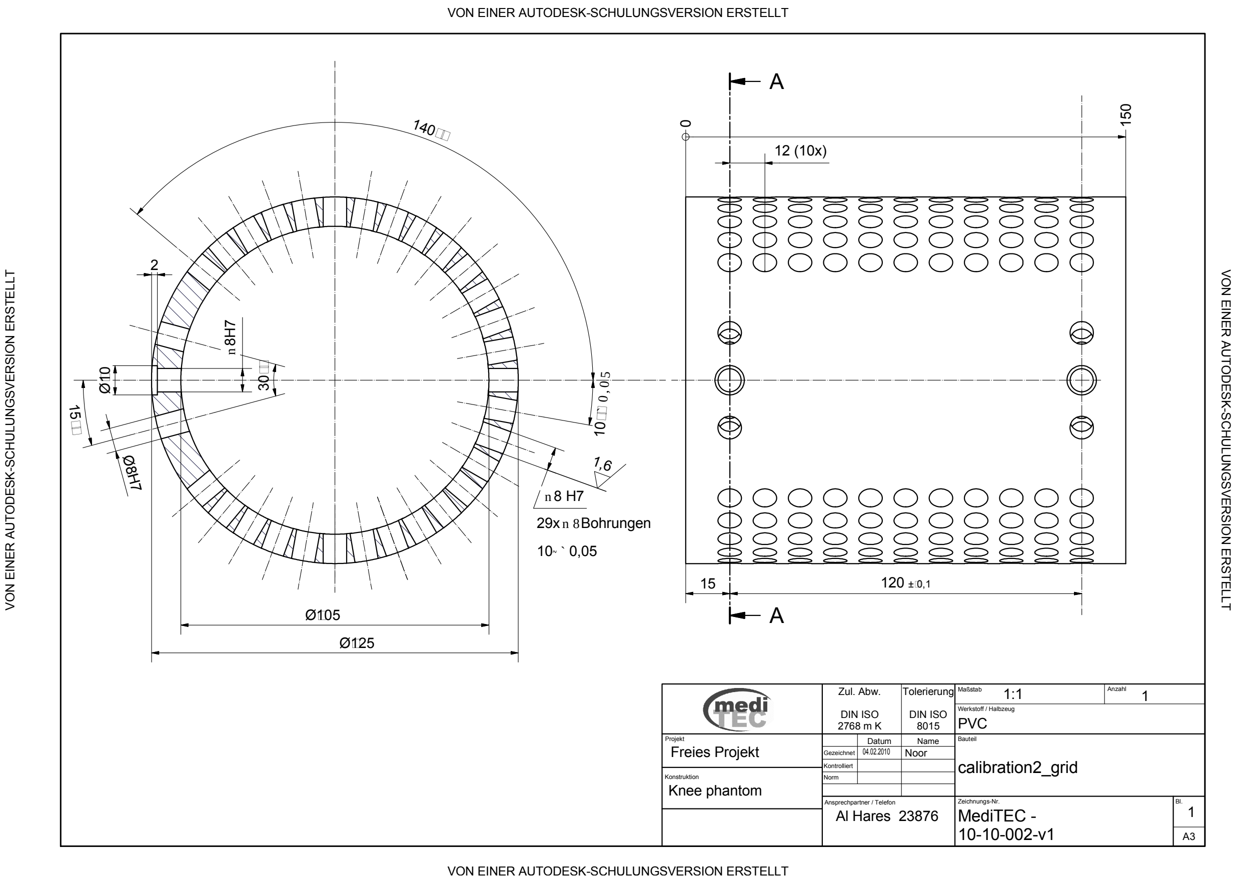

Figure A.1: CAD-drawing of calibration grid

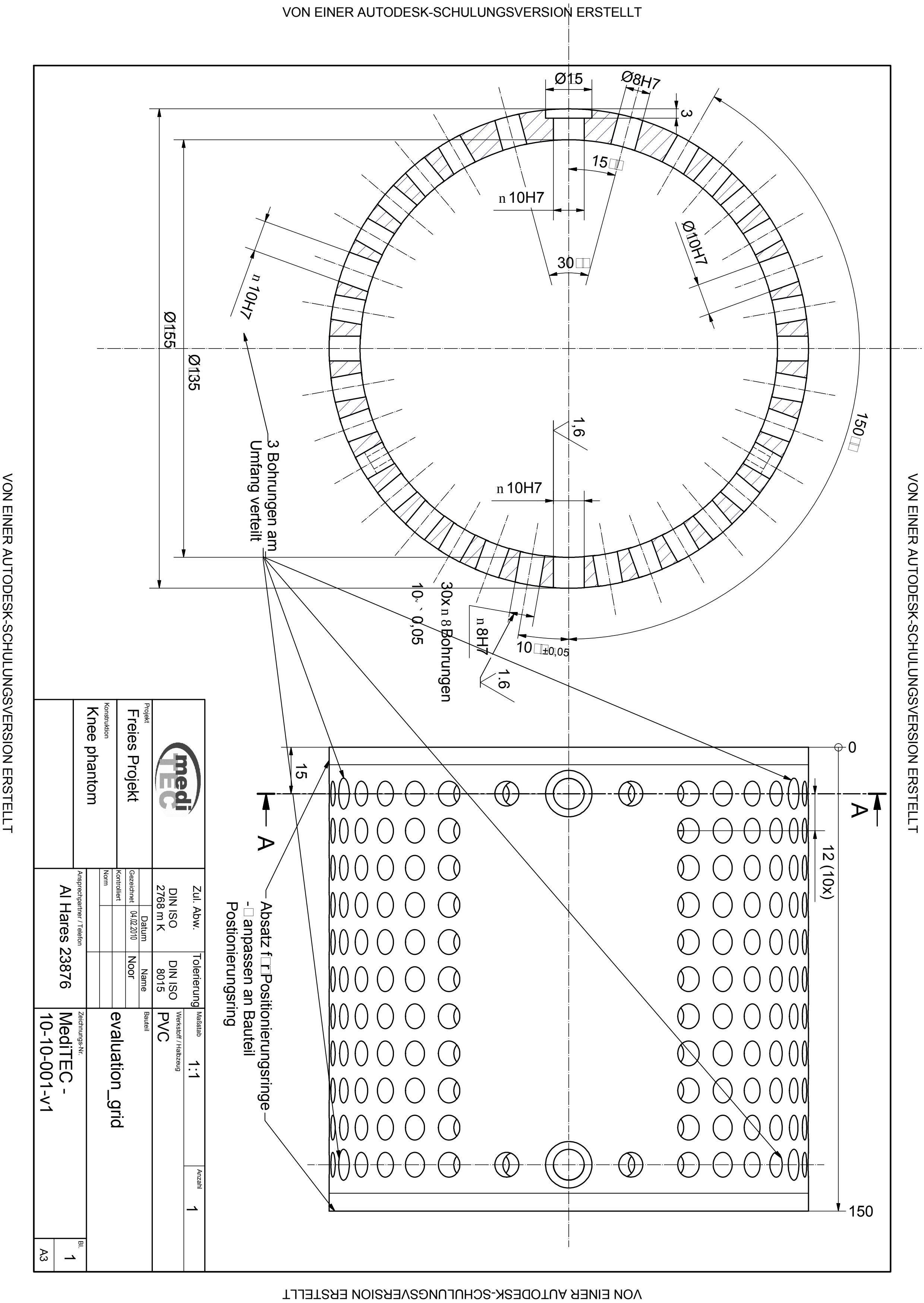

Figure A.2: CAD-drawing of evaluation grid

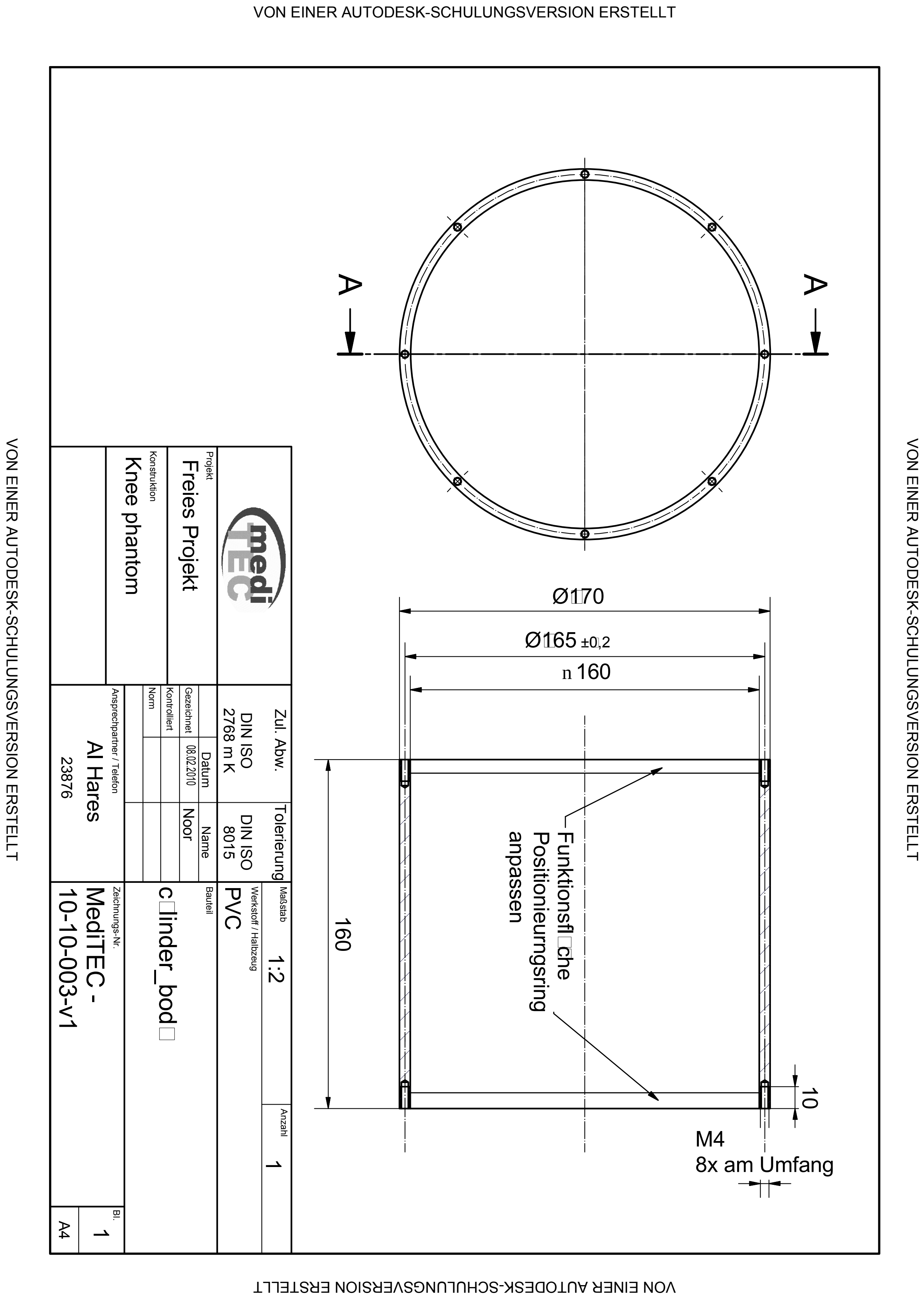

Figure A.3: CAD-drawing of cylinder body

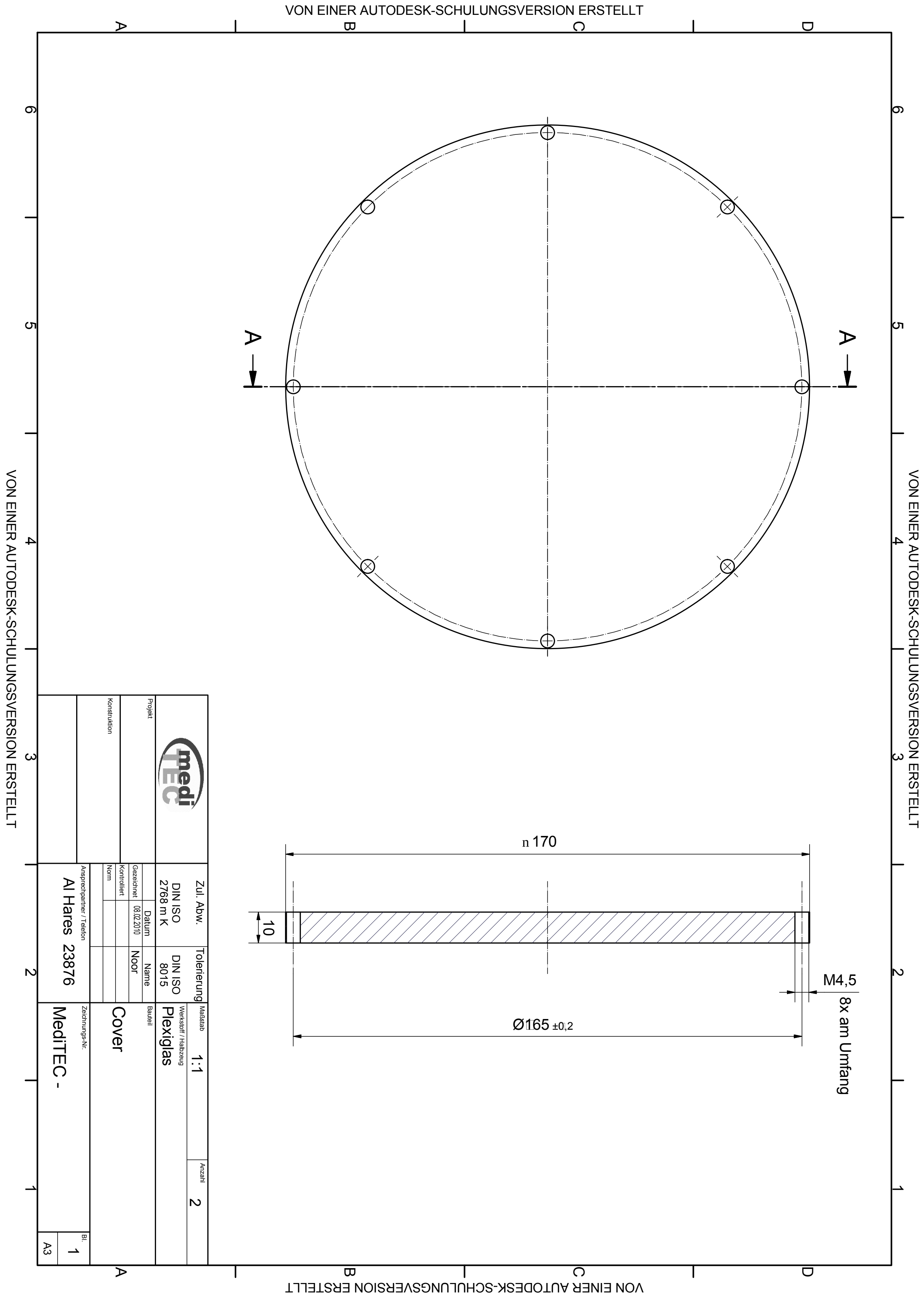

Figure A.4: CAD-drawing of the lid

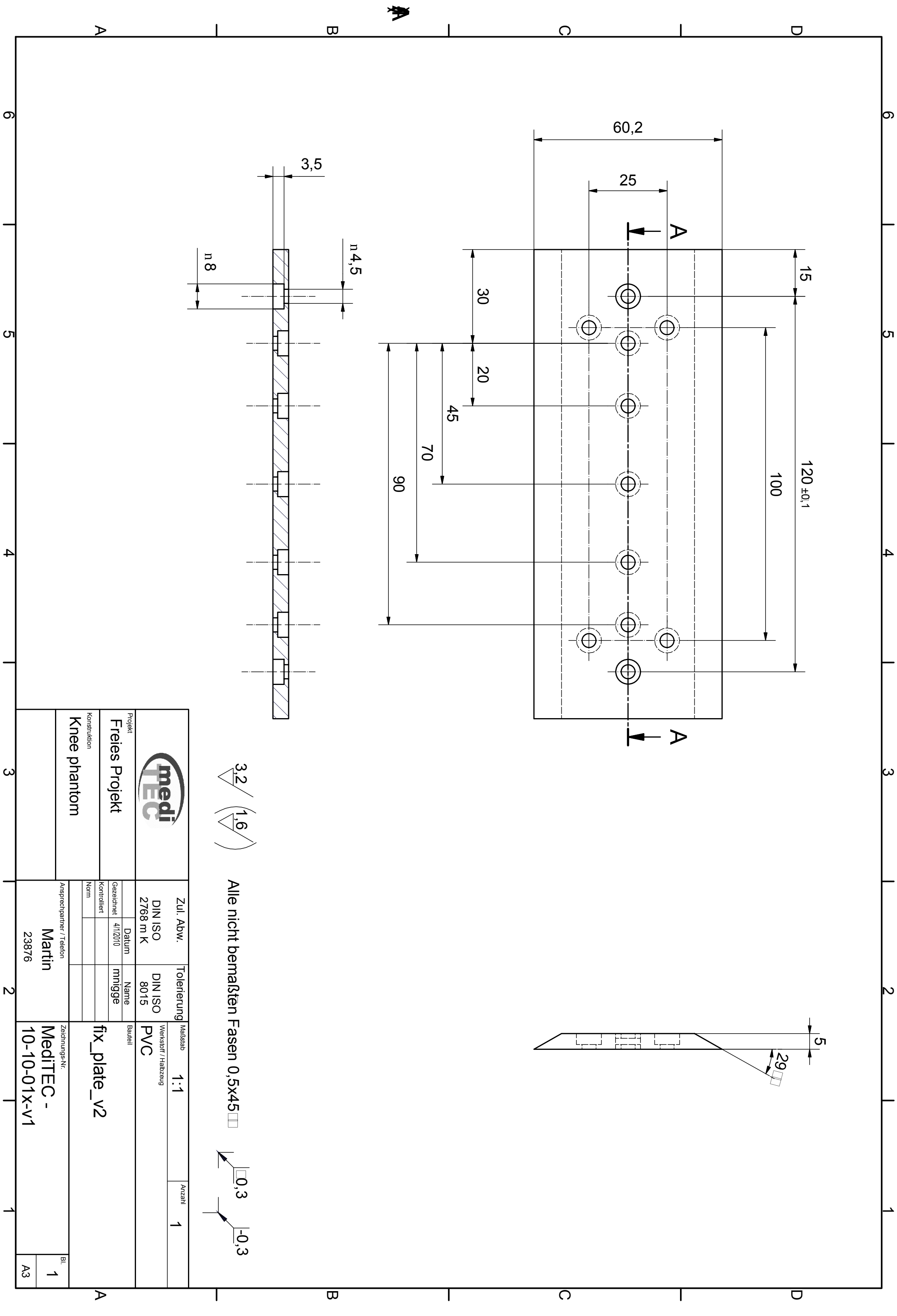

Figure A.5: CAD-drawing of the fixation plate

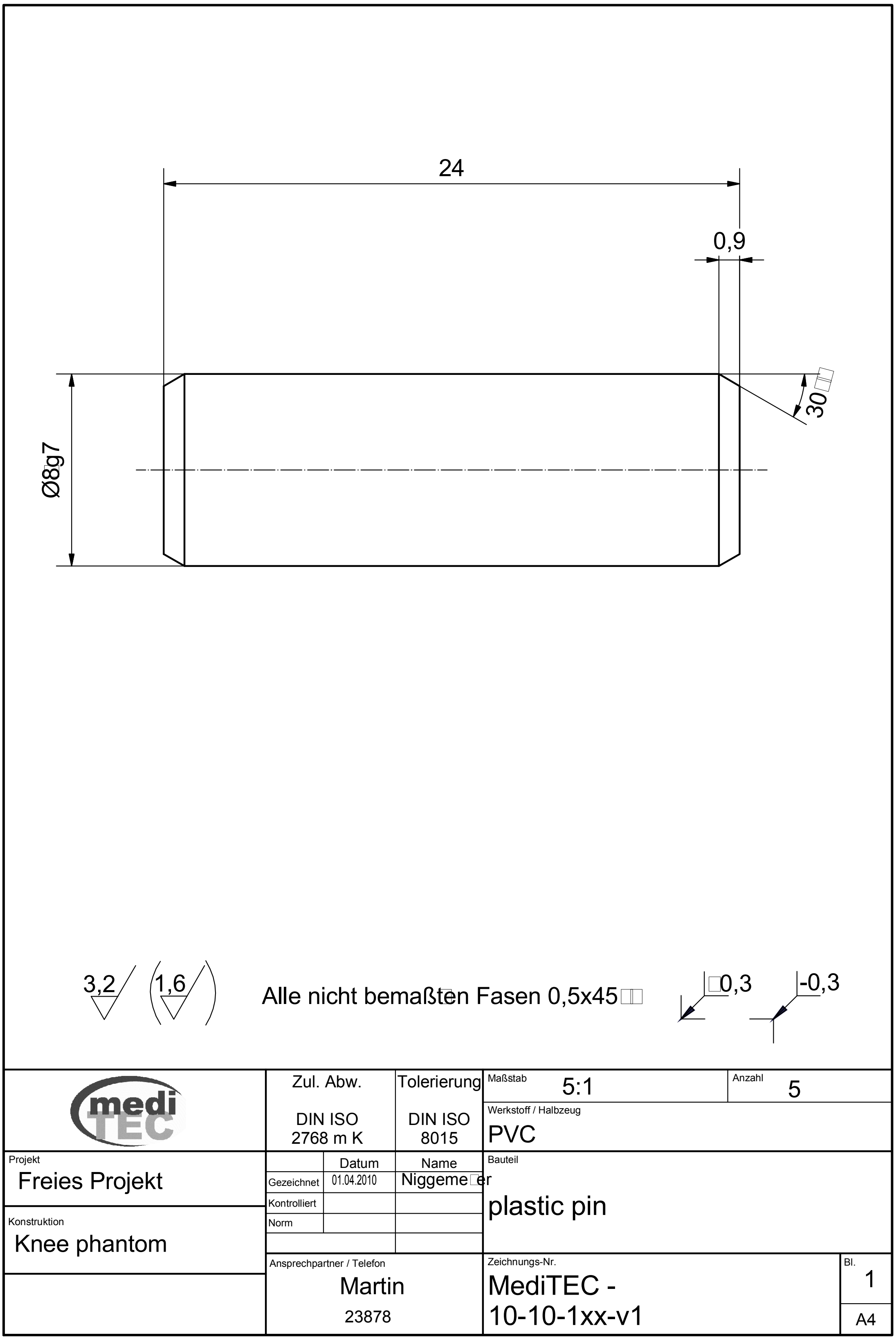

Figure A.6: CAD-drawing of fixation pins

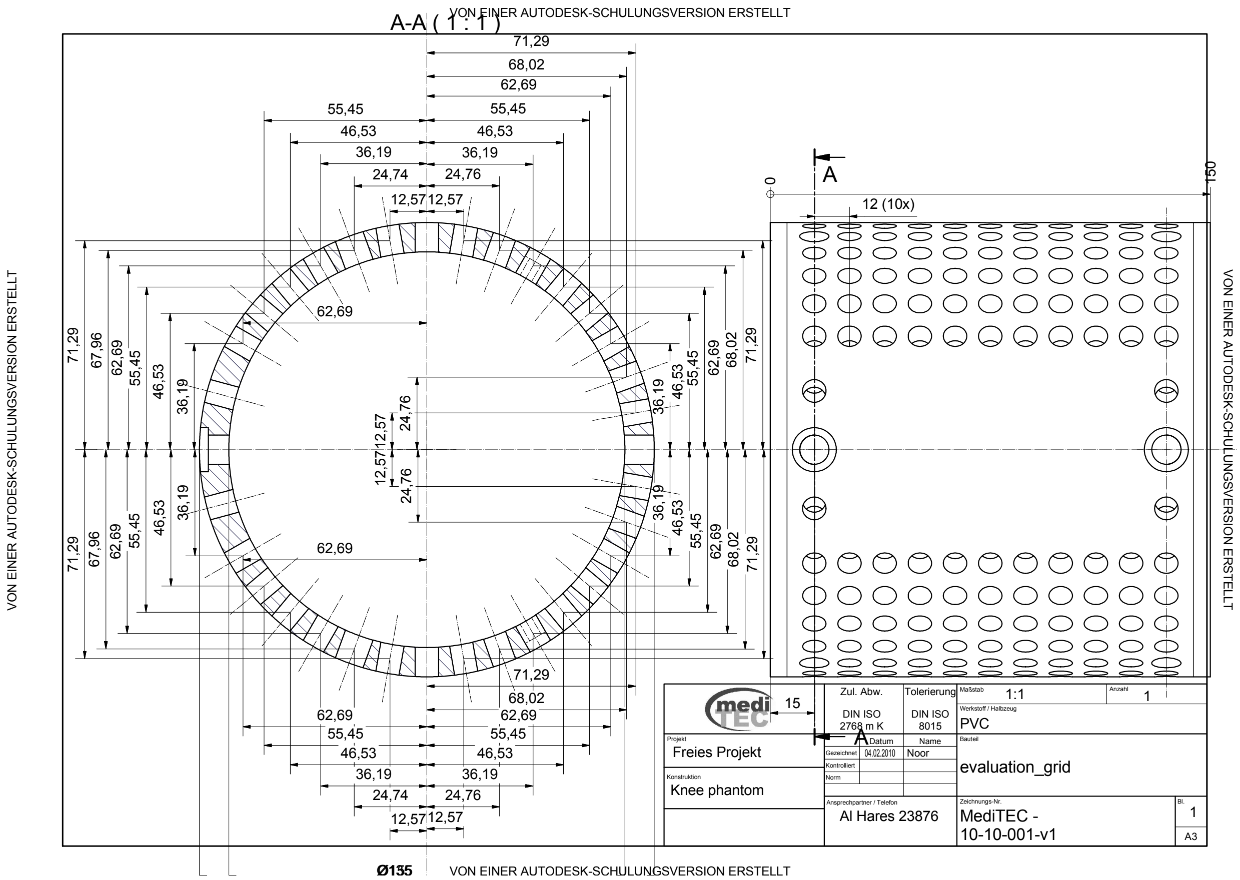

Figure A.7: CAD-drawing with outer cylinder coordinates

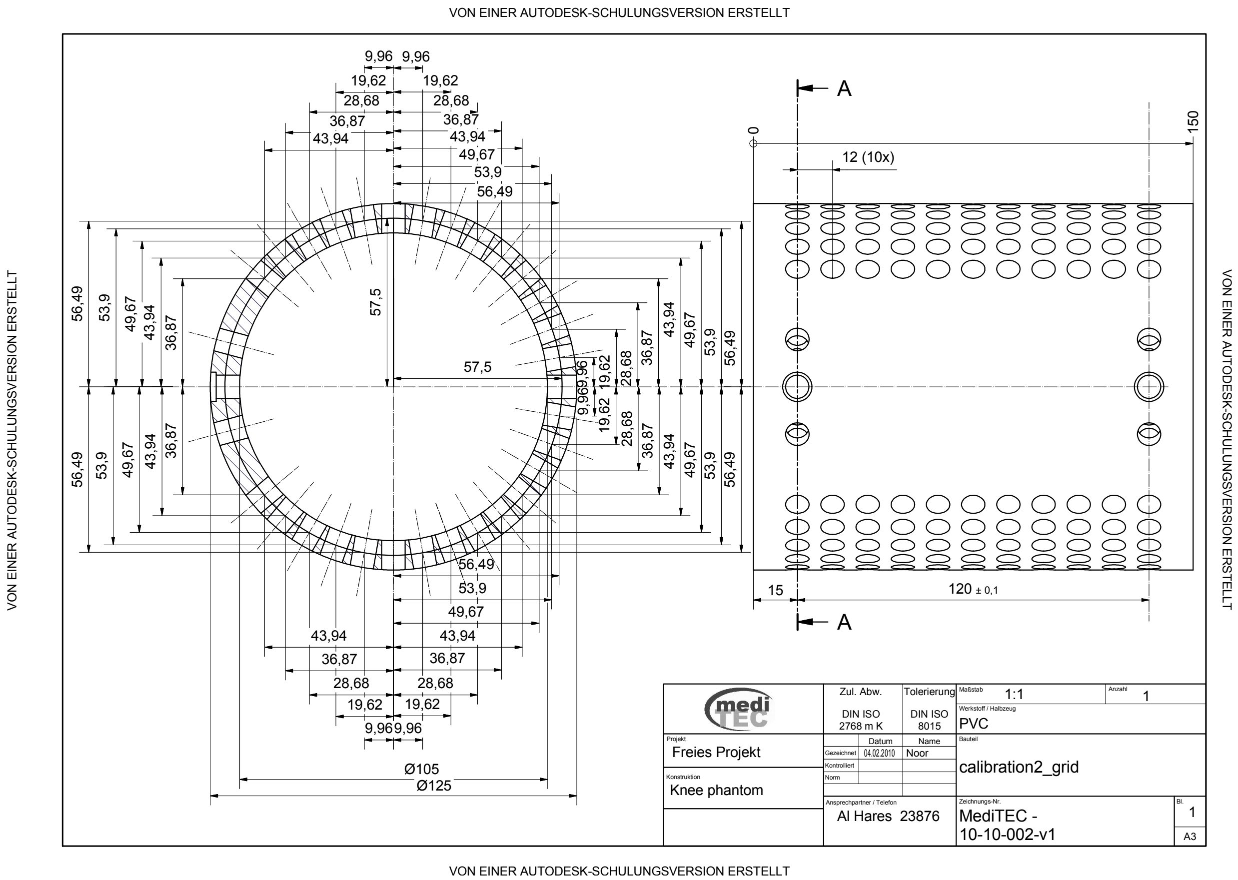

Figure A.8: CAD-drawing with inner cylinder coordinates

A.2 The thin plate spline for non-rigid image wraping

Image warping is a part of image processing that deals with geometric transformation techniques. It can be defined as the manipulation process of a significantly distorted image and is considered as an important stage in many applications of image analysis. Warping may also be used for the purpose of distortion correction. It involves transformation which maps all positions in one image plane to positions in a second plane. A pair of two-dimensional functions, $u(x, y)$ and $v(x, y)$, maps a position (x, y) in one image, where x denotes column number and y denotes row number, for the purpose of positioning (u, v) in another image [Glasbey und Mardia, 1998].

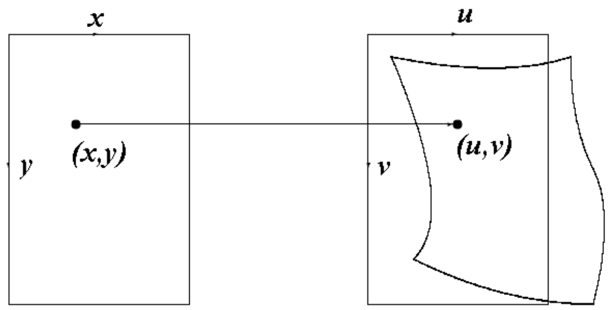

Figure A.9: Image warping [Glasbey und Mardia, 1998]

It arises in many image analysis problems, whether in order to register and image with a map of template, or to align two or more images. Some overviews of geometric transformations were given by Wolberg (1988), Bookstein (1991), Brown (1992) and Tang and Suen (1993). Matching process might be specified by some predefined points which must be brought into alignment, by local measures of correlation between images, or by the coincidence of edges.

Medical imaging plays an important role in a large number of clinical applications. It is used in medical diagnostics and at the areas of planning, carrying out and evaluating surgical procedures where high accuracy is required. [Glasbey und Mardia, 1998; Maintz und Viergever, 1998]

There are several registration methods and warping algorithms which have been developed. MR imaging modality, which involves non-rigid geometric distortion as well as nonuniform contrast enhancement, the surface interpolation method Thin-Plate Spline (TPS) has been shown to have a high potential for the unwarping of image sequences. It's elegant algebra expresses the dependence of the physical bending energy of a thin metal plate on point constraints. [Bookstein, 1989; Wang et al., 2000] During the upcoming subsection, Bookstein's bending energy equation and the thin plate spline algorithm will be explained in detail.

A.2.1 Thin Plate Spline

TPS for short is an interpolation method that finds a 'minimally bended' smooth surface that passes through all given points in the case of three dimensions. The term Thin plate splines comes from the fact that it more or less simulates how a thin metal sheet or plate would behave if it was forced through the same control points. It was pioneered to geometric design by Duchon, in year 1976, and formalized by Meinguet. Later on the mathematical approach for the two dimensional interpolation was adapted by Bookstein. [Bookstein, 1989; Cerney et al., 2003; Wang et al., 2000; Wikipedia, 2010.02.23]

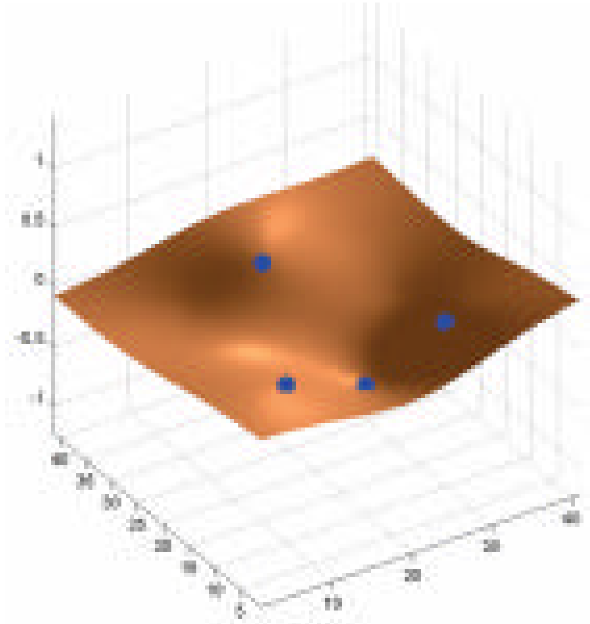

Figure A.10: Bending of a thin metal sheet[Whitbeck und Guo, 2006]

This interpolatin approach expresses the dependence of the physical bending energy on the point constraints of a thin metal plate. It's popular in representing shape transformations, for example, image morphing or shape detection/matching. In geometric morphometrics field, it has been used to graphically display warping required to interpolate between landmark configurations representing significant feature points. [Cerney et al., 2003]

A.2.1.1 Calculation of TPS

The mathematical methods that follow were adapted by Fred Bookstein, [Bookstein, 1989] which briefly during this section will be described. As mentioned before, this algorithm calculates the

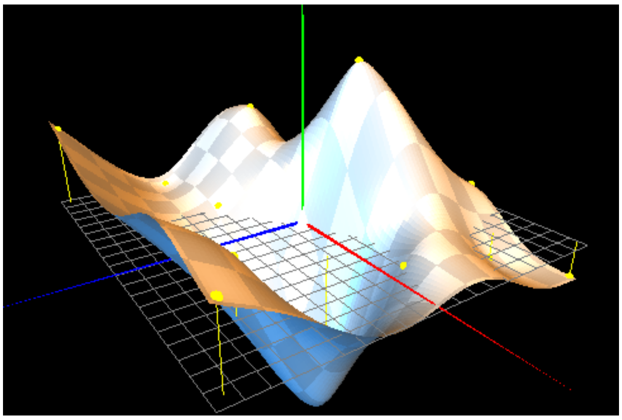

Figure A.11: Screenshot from the TPS demo [elonen, 2010.02.25]

mapping of the reference points to corresponding points on a target image. In two dimensions interpolation, these data can either lay over or below a plane of a thin metal plate. The displacement from the plate occurs orthogonally. If the plate is defined in the x, y plane, then these displacements, $z(x, y)$ describes the following surface

$$z(x, y) = -U(r) = -r^2 log r^2$$

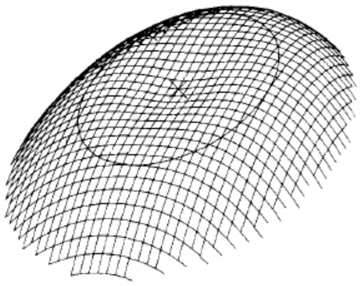

Figure A.12: A circular fragment of the surface z(x,y) viewed from above

where r represents the distance, i.e. $\sqrt{x^2 + y^2}$ from the cartesian origin for the two dimensional solution. When this model is applied to an image or scan warping, then the deformation of the plate in the z direction is interpreted as the displacement of the x or y coordinates. Thus, for two-dimensional interpolations, TPS calculations define a map $R^2 \rightarrow R^2$ with the following function

$$f(x, y) \rightarrow f(x', y') = (x, y + z(x, y))$$

where $z(x, y)$ is the displacement at the vertical direction of the metal plate. Defining a set of data points, a weighted combination of thin plate splines centered about each data point gives the interpolation function that passes through the points exactly while minimizing the so-called 'bending energy'. Bending energy is defined here as the integral over R^2 of the squares of the second derivatives:

$$\int\int_{R^2} \left(\frac{\partial z}{\partial x}\right)^2 + 2\left(\frac{\partial z}{\partial x \partial y}\right)^2 + \left(\frac{\partial z}{\partial y}\right)^2 dxdy$$

The $f(x, y)$ function maps exactly all land mark points from reference to corresponding points in the target. In matrix form, (x, y) is mapped to (x', y') as

$$\begin{bmatrix} x' \\ y' \end{bmatrix} = A \begin{bmatrix} 1 & x & y \end{bmatrix} + \sum_{i=1}^{n} w_i U(r),$$

Here n denotes the number of common landmark points for the interpolation between the target and reference examples. $U(r)$ is defined as the distance between landmark i and the current (x, y) point in the reference image. The matrix A contains parameters for the affine or linear transformation of the landmarks including translation, rotation, scale and shear, and multiplied by a matrix containing the full set of image data points for the reference example increased with a column of 1s. The matrix w includes parameters for the non-affine deformation. A and w are based upon the relationships between the reference and target landmark points and are determined in the following way:

Define P as an $nx(p + 1)$ matrix of reference landmark points preceded by a column of $1s$ in which n is the number of p-dimensional points.

$$P = \begin{bmatrix} 1 & x_1 & y_1 \\ 1 & x_2 & y_2 \\ 1 & ... & ... \\ 1 & x_n & y_n \end{bmatrix}$$

K is defined as an nxn matrix of the $U(r)$ functions of the distances between landmarks in the reference

$$K = \begin{bmatrix} 0 & U(r_{12}) & ... & U(r_{1n}) \\ U(r_{21}) & 0 & ... & U(r_{2n}) \\ ... & ... & ... & ... \\ U(r_{n1}) & U(r_{n2}) & ... & 0 \end{bmatrix}$$

and

$$L = \left[\begin{array}{c|c} K & P \\ \hline P^T & O \end{array} \right]$$

where O is a pxp matrix of zeros. A and w are found from the inverse of L by the equation

$$L^{-1}Y = \begin{pmatrix} W \mid a_1 & a_x & a_y \end{pmatrix}^T$$

in which

$$Y = \begin{pmatrix} V \mid 0 & 0 & 0 \end{pmatrix}^T$$

such that Y is an $(n+p+1)xp$ matrix of the landmarks of the target example V, increased by $p+1$ rows of p zero s.

Modifications to the thin plate spline algorithm in order to change from a two-dimensional to a three-dimensional analysis ($p = 3$) are minimal, and include solving $U(r) = |r|$ rather than $U(r) = r^2 log r^2$. The thin plate spline mapping function becomes

$$\begin{bmatrix} x' \\ y' \\ z' \end{bmatrix} = A \begin{bmatrix} 1 & x & y & z \end{bmatrix} + \sum_{i=1}^{n} w_i U(r),$$

in which the input (x, y, z) are the set of points for the full reference image or three-dimensional scan.[Cerney et al., 2003]